

Development and Modeling of Flowtube Apparatus for Conducting Corrosion  
Experiments

A thesis presented to  
the faculty of  
the Russ College of Engineering and Technology of Ohio University

In partial fulfillment  
of the requirements for the degree  
Master of Science

Lukas G. Johansson

December 2024

© 2024 Lukas G. Johansson. All Rights Reserved.

This thesis titled  
Development and Modeling of Flowtube Apparatus for Conducting Corrosion  
Experiments

by

LUKAS G. JOHANSSON

has been approved for  
the Department of Chemical and Biomolecular Engineering  
and the Russ College of Engineering and Technology by

Srdjan Nesic

Professor of Department of Chemical and Biomolecular Engineering

Patrick Fox

Dean, Russ College of Engineering and Technology

## Abstract

JOHANSSON, LUKAS G., M.S., December 2024, Chemical Engineering

Development and Modeling of Flowtube Apparatus for Conducting Corrosion

Experiments

Director of Thesis: Srdjan Nestic

The objective of this research is to continue development of the flowtube, a new type of test equipment developed at the ICMT. Baseline testing is commonly used to validate models and ensure understanding of the electrochemical system. Baseline mass transfer experiments were performed using a rotating cylinder electrode (RCE). Baseline corrosion experiments were completed using an RCE as well as a rotating disk electrode (RDE). Mass transfer within the RDE system was also successfully modeled using computational fluid dynamics (CFD) software Ansys Fluent. Experimental and simulated results were validated using well known and accepted correlations. Validation of the CFD simulations is vital because no physical prototype for the flowtube currently exists to compare with the CFD results. The RDE simulations will serve as a baseline to prove that Fluent is capable of performing accurate mass transfer calculations and potentially future corrosion simulations. Current testing apparatuses for flowing environments tend to be large and/or difficult to use in a small-scale lab. To combat this, the flowtube cell can create a controlled single phase flow regime in a glass cell or autoclave and can test 3 samples at one time in its most recent revision. A new revision is currently being created, so the flowtube was modeled using CFD in order to determine how design alterations will affect the flowing environment within the glass cell. The flowtube hydrodynamics have

been successfully modeled using Ansys Fluent. This model can illustrate fluid flow in the glass cell around the flowtube apparatus in both steady state and transient conditions.

This model will continue to be expanded upon in the future to reflect the design considerations for the next prototype version. Design considerations and their impact on the hydrodynamics of the flowtube system were analyzed through this research.

### **Acknowledgments**

I would like to thank my advisor, Dr. Nestic, my thesis committee, the Institute for Corrosion and Multiphase Technology, and the corporate sponsors of the ICMT for the opportunity to perform this research.

## Table of Contents

	Page
Abstract.....	3
Acknowledgments.....	5
List of Tables .....	9
List of Figures .....	11
Chapter 1: Introduction and Literature Review .....	16
1.1 Background on Corrosion.....	16
1.2 Cost of Corrosion.....	18
1.3 Laboratory Experimentation Techniques.....	21
Chapter 2: Objectives and Research Questions .....	31
Chapter 3: Safety .....	32
Chapter 4: Corrosion and Mass Transfer Results .....	34
4.1 Preliminary RCE Experiments.....	34
4.1.1 Equipment.....	34
4.1.2 Experimental Apparatus.....	34
4.1.3 Materials Tested.....	35
4.1.4 Test Matrices.....	36
4.1.5 Procedure .....	38
4.2 Preliminary RDE Experiments .....	48
4.2.1 Equipment.....	48
4.2.2 Experimental Apparatus.....	48
4.2.3 Materials Tested.....	49
4.2.4 Test Matrix.....	50
4.2.5 Procedure .....	51
Chapter 5: Preliminary Mass Transfer and Corrosion Results and Discussion.....	56
5.1 Preliminary RCE Experiments.....	56
5.1.1 Mass Transfer Experiments .....	56
5.1.2 Corrosion Experiments .....	59
5.2 Preliminary RDE Experiments .....	72
5.3 Experimental Summary .....	75
Chapter 6: Methodology for Modeling Flowtube Using CFD .....	77

6.1	Simplified Preliminary Model and Introduction to CFD Modeling .....	77
6.1.1	Rationale for CFD Modeling .....	77
6.1.2	Translation to SpaceClaim .....	78
6.1.3	Meshing .....	82
6.1.4	Ansys Fluent CFD Modelling .....	85
6.2	Replication of Physical Prototype Model .....	87
6.3	Removal of Internal Flow Straightener .....	91
6.4	Reduced Counter Electrode Diameter .....	97
Chapter 7:	Methodology for Modeling RDE Simulations Using CFD .....	100
7.1	Mass Transfer CFD Model for RDE Simulation .....	100
Chapter 8:	Results and Discussion for CFD Model of Flowtube .....	105
8.1	Simplified Preliminary Model .....	105
8.1.1	Transient Simulation Results .....	105
8.1.2	Steady State Simulation Results .....	109
8.2	Replication of Physical Prototype Model .....	123
8.2.1	1000 RPM .....	124
8.2.2	2000 RPM .....	127
8.2.3	5000 RPM .....	130
8.3	Removal of Internal Flow Straightener .....	135
8.3.1	1000 RPM .....	135
8.3.2	2000 RPM .....	138
8.3.3	5000 RPM .....	141
8.4	Reduced Counter Electrode Diameter .....	145
8.4.1	1000 RPM .....	146
8.4.2	2000 RPM .....	149
8.4.3	5000 RPM .....	152
Chapter 9:	Results and Discussion for CFD Model of RDE .....	158
9.1	Mass Transfer CFD Model for RDE Simulation .....	158
Chapter 10:	Conclusions and Future Work .....	162
Chapter 11:	References .....	165
Appendix A:	Additional Experimental Methodology .....	169
	Flowmeter Calibration .....	169
	Equipment .....	169

Experimental Apparatus.....	169
Procedure .....	169
Results.....	171
Flowtube Flow Rate Calibration.....	173
Equipment.....	173
Experimental Apparatus.....	173
Procedure .....	174
Results.....	177
Reference Electrode OCP Calibration .....	180
Equipment.....	180
Experimental Apparatus.....	180
Procedure .....	181
Results.....	183
Proposed Flowtube Baseline Corrosion experimentation.....	185
Equipment.....	185
Experimental Apparatus.....	185
Materials Tested.....	185
Test Matrix.....	186
Polishing RDE Specimen.....	188
Equipment.....	188
Experimental Apparatus.....	188
Procedure .....	188
Appendix B: Equations.....	190
Mass Transfer Experimentation and RCE Equations .....	190
RDE Equations.....	192
Corrosion Rate Calculations .....	195
Ansys Fluent Background.....	196
Appendix C: Material Composition Data .....	200
1018 Mild Steel #5.....	200
X65 Mild Steel #49.....	202

## List of Tables

	Page
Table 1. Global Cost of Corrosion (CoC) by Geographic Region by Sector (US\$ billions, 2013) <sup>6</sup> .....	19
Table 2. Test Matrix for RCE Mass Transfer Experimentation.....	36
Table 3. Test Matrix for RCE Corrosion Experimentation.....	37
Table 4. Test Matrix for RDE Corrosion Experimentation .....	50
Table 5. Superficial Velocity, Limiting Current, and Mass Transfer Coefficient for Each Rotational Speed Examined in Mass Transfer Experimentation .....	58
Table 6. Tabulated Nondimensional Numbers for Mass Transfer Experiments .....	58
Table 7. Linear Polarization Resistance Data for RCE corrosion experiments in CO <sub>2</sub> sparged environment at pH 4.0±0.1 .....	62
Table 8. Comparison of LPR corrosion rate to FREECORP™ in CO <sub>2</sub> sparged environment at pH 4.0±0.1 through 10.1 cm diameter pipe .....	62
Table 9. Linear Polarization Resistance Data for RCE corrosion experiments in CO <sub>2</sub> sparged environment at pH 5.0±0.1 .....	64
Table 10. Comparison of LPR corrosion rate to FREECORP™ in CO <sub>2</sub> sparged environment at pH 5.0±0.1 through 10.1 cm diameter pipe .....	64
Table 11. Linear Polarization Resistance Data for RCE corrosion experiments in CO <sub>2</sub> sparged environment at pH 6.0±0.1 .....	66
Table 12. Comparison of LPR corrosion rate to FREECORP™ in CO <sub>2</sub> sparged environment at pH 6.0±0.1 through 10.1 cm diameter pipe .....	66
Table 13. Linear Polarization Resistance Data for RCE corrosion experiments in N <sub>2</sub> sparged environment at pH 5.0±0.1 .....	70
Table 14. Comparison of LPR corrosion rate to FREECORP™ in N <sub>2</sub> sparged environment at pH 5.0±0.1 through 10.1 cm diameter pipe .....	70
Table 15. Linear Polarization Resistance Data for RDE corrosion experiments in CO <sub>2</sub> sparged environment at pH 4.0±0.1 .....	74
Table 16. Comparison of LPR corrosion rate to FREECORP™ in CO <sub>2</sub> sparged environment at pH 4.0±0.1 through 10.1 cm diameter pipe .....	75
Table 17. Comparison of superficial velocity between various flowtube design considerations .....	157
Table 18. Test Matrix for Flowtube Mass Transfer Experimentation .....	186
Table 19. Test Matrix for Flowtube Corrosion Experimentation .....	187
Table 20. Material Analysis for 1018 Mild Steel #5 .....	201

Table 21. Material Analysis for X65 Mild Steel #49..... 203

## List of Figures

	Page
Figure 1. Causes of significant incidents in onshore and offshore pipelines (reproduced “fair use” from Federal government publication) <sup>8</sup> .....	21
Figure 2. Schematic representation of flowtube apparatus in a 2-liter glass cell (Albert Schubert).....	23
Figure 3. Schematic representation of flowtube internal components (Albert Schubert). 25	
Figure 4. Flowtube specimen holder separation from upper housing.....	28
Figure 5. 2 L glass cell set up for RCE experimentation (Cody Shafer) .....	35
Figure 6. 1 L glass cell set up for RDE experimentation (Cody Shafer).....	49
Figure 7. Potentiodynamic sweep data showing the effect of rotational rate on nickel RCE mass transfer in N <sub>2</sub> sparged, 0.01 M ferri-/ferro- cyanide, and 0.5 M NaOH solution at 30°C for 500 RPM, 1000 RPM, 1500 RPM, 2000 RPM, and 6000 RPM rotational rates. ....	57
Figure 8. Sherwood Correlation Resulting from Mass Transfer Experiments Compared to Correlation from the Eisenberg Paper <sup>19</sup> .....	59
Figure 9. Potentiodynamic sweep data showing the effect of rotational rate on 1018 mild steel RCE corrosion in CO <sub>2</sub> sparged, pH 4.0±0.1, and 1 wt% NaCl electrolyte solution at 35°C in for 500 RPM, 1000 RPM, 1500 RPM, and 2000 RPM RCE rotational rates. ....	61
Figure 10. Potentiodynamic sweep data showing the effect of rotational rate on 1018 mild steel RCE corrosion in CO <sub>2</sub> sparged, pH 5.0±0.1, and 1 wt% NaCl electrolyte solution at 35°C in for 500 RPM, 1000 RPM, 1500 RPM, and 2000 RPM RCE rotational rates. ....	63
Figure 11. Potentiodynamic sweep data showing the effect of rotational rate on 1018 mild steel RCE corrosion in CO <sub>2</sub> sparged, pH 6.0±0.1, and 1 wt% NaCl electrolyte solution at 35°C in for 500 RPM, 1000 RPM, 1500 RPM, and 2000 RPM RCE rotational rates. ....	65
Figure 12. Potentiodynamic sweep data showing the effect of pH on 1018 mild steel RCE corrosion in CO <sub>2</sub> sparged and 1 wt% NaCl electrolyte solution at 35°C for pH 4.0±0.1, 5.0±0.1, and 6.0±0.1 at 500 RPM rotational rate.....	67
Figure 13. Potentiodynamic sweep data showing the effect of rotational rate on 1018 mild steel RCE corrosion in N <sub>2</sub> sparged, pH 5.0±0.1, and 1 wt% NaCl electrolyte solution at 35°C in for 500 RPM, 1000 RPM, 1500 RPM, and 2000 RPM RCE rotational rates. ....	69
Figure 14. Potentiodynamic sweep data showing the effect of N <sub>2</sub> or CO <sub>2</sub> sparge gas on 1018 mild steel RCE corrosion in pH 5.0±0.1 and 1 wt% NaCl electrolyte solution at 35°C at 500 RPM rotational rate.....	71
Figure 15. Potentiodynamic sweep data showing the effect of rotational rate on X65 mild steel RDE corrosion in CO <sub>2</sub> sparged, pH 4.0±0.1, and 1 wt% NaCl electrolyte solution at	

30°C in for 250 RPM, 500 RPM, 1000 RPM, 2000 RPM, 4000 RPM, and 8000 RPM RDE rotational rates.....	73
Figure 16. CAD drawing of simplified flowtube in a glass cell .....	79
Figure 17. Cross-section view of CAD drawing of simplified flowtube in a glass cell ...	80
Figure 18. External view of volume enclosed by glass cell.....	81
Figure 19. Enclosure volume surrounding impeller .....	82
Figure 20. External view of mesh on volume enclosed by the glass cell .....	84
Figure 21. Cross-section view of mesh on volume enclosed by the glass cell .....	85
Figure 22. External view of flowtube geometry with external baffles .....	88
Figure 23. Cross-section view of flowtube with internal flow straightener and external baffles in the 4 L glass cell .....	90
Figure 24. Internal flow straightener geometry used in CFD simulations.....	90
Figure 25. Cross-section of refined mesh used for CFD simulation in 4 L glass cell with baffles and internal flow straightener .....	91
Figure 26. Cross-section view of flowtube geometry with external baffles .....	93
Figure 27. Cross-section of mesh used for 1000 RPM and 2000 RPM simulations in 4 L glass cell with external baffles .....	95
Figure 28. Cross-section of refined mesh used for 5000 RPM simulation in 4 L glass cell with baffles.....	97
Figure 29. Bottom view of flowtube with 0.25-inch diameter counter electrode.....	99
Figure 30. SpaceClaim model of RDE in 1 L glass cell .....	102
Figure 31. Initial salt concentration on the base of the glass cell .....	106
Figure 32. Salt concentration at 20.8 seconds throughout the glass cell .....	106
Figure 33. Initial velocity pathlines in glass cell .....	107
Figure 34. Final velocity pathlines in glass cell.....	108
Figure 35. Velocity vectors in vertical cross section of preliminary model at 1000 RPM .....	111
Figure 36. Velocity vectors in horizontal cross section of preliminary model at 1000 RPM .....	111
Figure 37. Velocity vectors on exterior of preliminary model at 1000 RPM.....	112
Figure 38. Turbulent kinetic energy in vertical cross section of preliminary model at 1000 RPM .....	112
Figure 39. $y^+$ values in vertical cross section of preliminary model at 1000 RPM .....	113
Figure 40. Velocity vectors in vertical cross section of preliminary model at 2000 RPM .....	115

Figure 41. Velocity vectors in horizontal cross section of preliminary model at 2000 RPM .....	115
Figure 42. Velocity vectors on exterior of preliminary model at 2000 RPM .....	116
Figure 43. Turbulent kinetic energy in vertical cross section of preliminary model at 2000 RPM .....	116
Figure 44. $y^+$ values in vertical cross section of preliminary model at 2000 RPM .....	117
Figure 45. Velocity vectors in vertical cross section of preliminary model at 5000 RPM .....	118
Figure 46. Velocity vectors in horizontal cross section of preliminary model at 5000 RPM .....	119
Figure 47. Velocity vectors on exterior of preliminary model at 5000 RPM .....	119
Figure 48. Turbulent kinetic energy in vertical cross section of preliminary model at 5000 RPM .....	120
Figure 49. $y^+$ values in vertical cross section of preliminary model at 5000 RPM .....	120
Figure 50. Effect of impeller rotational speed in preliminary model on velocity observed in specimen holder .....	123
Figure 51. Velocity vectors in yz cross-section of physical prototype model at 1000 RPM impeller speed .....	125
Figure 52. Velocity pathlines in yz cross-section of physical prototype model at 1000 RPM impeller speed.....	125
Figure 53. Turbulent kinetic energy contour in yz cross-section of physical prototype model at 1000 RPM impeller speed.....	126
Figure 54. $y^+$ contour in yz cross-section of physical prototype model at 1000 RPM impeller speed .....	126
Figure 55. Velocity vectors in yz cross-section of physical prototype model at 2000 RPM impeller speed .....	128
Figure 56. Velocity pathlines in yz cross-section of physical prototype model at 2000 RPM impeller speed.....	128
Figure 57. Turbulent kinetic energy contour in yz cross-section of physical prototype model at 2000 RPM impeller speed.....	129
Figure 58. $y^+$ contour in yz cross-section of physical prototype model at 2000 RPM impeller speed .....	129
Figure 59. Velocity vectors in yz cross-section of physical prototype model at 5000 RPM impeller speed .....	131
Figure 60. Velocity pathlines in yz cross-section of physical prototype model at 5000 RPM impeller speed.....	131

Figure 61. Turbulent kinetic energy contour in yz cross-section of physical prototype model at 5000 RPM impeller speed.....	132
Figure 62. $y^+$ contour in yz cross-section of physical prototype model at 5000 RPM impeller speed .....	132
Figure 63. Velocity vectors in yz cross-section of model without internal flow straightener at 1000 RPM impeller speed.....	136
Figure 64. Velocity pathlines in yz cross-section of model without internal flow straightener at 1000 RPM impeller speed.....	136
Figure 65. Turbulent kinetic energy contour in yz cross-section of model without internal flow straightener at 1000 RPM impeller speed.....	137
Figure 66. $y^+$ contour in yz cross-section of model without internal flow straightener at 1000 RPM impeller speed.....	137
Figure 67. Velocity vectors in yz cross-section of model without internal flow straightener at 2000 RPM impeller speed.....	139
Figure 68. Velocity pathlines in yz cross-section of model without internal flow straightener at 2000 RPM impeller speed.....	139
Figure 69. Turbulent kinetic energy contour in yz cross-section of model without internal flow straightener at 2000 RPM impeller speed.....	140
Figure 70. $y^+$ contour in yz cross-section of model without internal flow straightener at 2000 RPM impeller speed.....	140
Figure 71. Velocity vectors in yz cross-section of model without internal flow straightener at 5000 RPM impeller speed.....	142
Figure 72. Velocity pathlines in yz cross-section of model without internal flow straightener at 5000 RPM impeller speed.....	142
Figure 73. Turbulent kinetic energy contour in yz cross-section of model without internal flow straightener at 5000 RPM impeller speed.....	143
Figure 74. $y^+$ contour in yz cross-section of model without internal flow straightener at 5000 RPM impeller speed.....	143
Figure 75. Velocity vectors in yz cross-section of smaller counter electrode model at 1000 RPM impeller speed.....	146
Figure 76. Velocity pathlines in yz cross-section of smaller counter electrode model at 1000 RPM impeller speed.....	147
Figure 77. Turbulent kinetic energy contour in yz cross-section of smaller counter electrode model at 1000 RPM impeller speed .....	147
Figure 78. $y^+$ contour in yz cross-section of smaller counter electrode model at 1000 RPM impeller speed.....	148
Figure 79. Velocity vectors in yz cross-section of smaller counter electrode model at 2000 RPM impeller speed.....	149

Figure 80. Velocity pathlines in yz cross-section of smaller counter electrode model at 2000 RPM impeller speed.....	150
Figure 81. Turbulent kinetic energy contour in yz cross-section of smaller counter electrode model at 2000 RPM impeller speed .....	150
Figure 82. $y^+$ contour in yz cross-section of smaller counter electrode model at 2000 RPM impeller speed.....	151
Figure 83. Velocity vectors in yz cross-section of smaller counter electrode model at 5000 RPM impeller speed.....	152
Figure 84. Velocity pathlines in yz cross-section of smaller counter electrode model at 5000 RPM impeller speed.....	153
Figure 85. Turbulent kinetic energy contour in yz cross-section of smaller counter electrode model at 5000 RPM impeller speed .....	153
Figure 86. $y^+$ contour in yz cross-section of smaller counter electrode model at 5000 RPM impeller speed.....	154
Figure 87. Velocity Vectors in RDE Simulation at 1000 RPM.....	158
Figure 88. $H^+$ Concentration profile 1 mm above centerline starting at RDE surface for 1000 RPM trial.....	159
Figure 89. Comparison of simulated mass transfer boundary layer thickness to theoretical correlation .....	161
Figure 90. Flowmeter Calibration Curve .....	172
Figure 91. Flowtube calibration rig used in voltage response calibration (Albert Schubert) .....	173
Figure 92. Flowmeter Voltage Output as a Function of Controller Voltage Input.....	178
Figure 93. Superficial Velocity as a Function of Voltage Input to Flowtube Controller	179
Figure 94. PVC Experimental Apparatus for Use in OCP Calibration.....	181
Figure 95. Open Circuit Potential Using Brass Ring on Flowtube Reference Electrode	184

## Chapter 1: Introduction and Literature Review

### 1.1 Background on Corrosion

Corrosion is an electrochemical process that affects nearly every metal surface, especially those in contact with aqueous environments. Corrosion involves a series of two coupled electrochemical half reactions: the cathodic half reaction and the anodic half reaction. The cathodic half reaction is a reduction reaction whereas the anodic half reaction is an oxidation reaction. For the case of steel within an acidic solution, the anodic half reaction is reflected in Reaction (1) below, which shows the oxidative dissolution of iron.



Within the acidic solution, the cathodic half reaction is reflected in Reaction (2) below, which shows the reduction of hydrogen within the electrolyte solution.



The complete redox reaction for iron in acidic solution is determined by combining the two half reactions and is shown in Reaction (3) below.



The corrosion of steel involves the electrochemical reactions described above. As with other processes, the rate at which corrosion occurs is limited by the slowest step within the process. Without the addition of other aqueous species or reactions, the

corrosion rate can be limited by the rate at which  $H^+$  ions are brought to the metal surface, otherwise known as mass transfer limited, or by the rate at which the electrochemical reaction occurs, otherwise known as charge transfer limited.<sup>1</sup>

Within many environments that experience corrosion, such as oil pipelines, gaseous carbon dioxide is present and can dissolve into the electrolyte solution as shown in Reaction (4) below.



After the dissolution of  $CO_2$ , the aqueous  $CO_2$  goes through a hydration reaction with the water present in order to form carbonic acid, as shown in Reaction (5) below.



The carbonic acid, being a diprotic acid, is then able to dissociate in two distinct steps as shown in Reactions (6) and (7) below



Due to the addition of the carbonic species within solution, corrosion within a  $CO_2$  environment can now be limited by the chemical reaction rates of the reactions listed above. In the case of corrosion of steel in an acidic environment containing  $CO_2$ , these chemical reactions significantly alter the rate of the electrochemical processes at the

metal surface.<sup>2,3</sup> The dissociation of carbonic acid introduces a source of  $H^+$  ions to the electrolyte solution, which then replace the  $H^+$  ions consumed during the cathodic half reaction described in Reaction (2). Because the hydrogen ions consumed through Reaction (2) are replaced through Reactions (6) and (7), this causes an effect known as buffering. Buffering allows the concentration of hydrogen ions to resist change and thereby remain consistent within solution, which then promotes an increase in the corrosion rate.<sup>4,5</sup>

## **1.2 Cost of Corrosion**

In 2016, the National Association of Corrosion Engineers (NACE) published a study examining the economic impact of corrosion throughout the world.<sup>6</sup> This study analyzed the cost of corrosion in various countries and within different industries in 2013. The results are tabulated below in Table 1.

Table 1. Global Cost of Corrosion (CoC) by Geographic Region by Sector (US\$ billions, 2013)<sup>6</sup>

<b>Economic Regions</b>	<b>Agriculture CoC US\$ billion</b>	<b>Industry CoC US\$ billion</b>	<b>Services CoC US\$ billion</b>	<b>Total CoC US\$ billion</b>	<b>Total GDP US\$ billion</b>	<b>CoC % GDP</b>
United States	2.0	303.2	146.0	451.3	16,720	2.7%
India	17.7	20.3	32.3	70.3	1,670	4.2%
European Region	3.5	401	297	701.5	18,331	3.8%
Arab World	13.3	34.2	92.6	140.1	2,789	5.0%
China	56.2	192.5	146.2	394.9	9,330	4.2%
Russia	5.4	37.2	41.9	84.5	2,113	4.0%
Japan	0.6	45.9	5.1	51.6	5,002	1.0%
Four Asian Tigers + Macau	1.5	29.9	27.3	58.6	2,302	2.5%
Rest of the World	52.4	382.5	117.6	552.5	16,057	3.4%
<b>Global</b>	<b>152.7</b>	<b>1446.7</b>	<b>906.0</b>	<b>2505.4</b>	<b>74,314</b>	<b>3.4%</b>

As shown in Table 1, the global cost of corrosion in 2013 was in excess of \$2.5 trillion. In the United States, the cost of corrosion was over \$450 billion, equivalent to

2.7% of the Gross Domestic Product (GDP). A subsequent study indicated the cost of corrosion within the US rose to \$1.1 trillion in 2016.<sup>7</sup> The cost of corrosion can be broken down into two distinct categories: direct costs and indirect costs. Direct costs are defined as the money spent directly on replacing or maintaining equipment exposed to corrosive environments. Indirect costs are defined as all the costs that result from corrosion, oftentimes due to failure of equipment. Examples of indirect costs of corrosion include, but are not limited to, plant down time, loss of product, loss of efficiency, environmental contamination, losses to other industries, and overdesign. The NACE study attempted to average the cost of corrosion from various previous studies, not all of which reported the indirect cost of corrosion. As a result, it is likely that the reported values are an underrepresentation of the true cost of corrosion.

Many industries have an interest in understanding and mitigating corrosion; for the purposes of this research, influences on the oil and gas industry have been examined. Pipe flow environments commonly experience the effects of corrosion. “Corrosion is one of the leading causes of failures in onshore transmission pipelines (both gas and hazardous liquids) in the United States.”<sup>8</sup> In 2008, the U.S. Department of Transportation’s Pipeline and Hazardous Materials Safety Administration (PHMSA) requested a study intended to provide a common understanding of issues related to pipeline corrosion. To better understand the potential dangers of corrosion, Figure 1 below shows a breakdown of the causes for all significant pipeline incidents. Note that corrosion was the cause of 18% of all incidents between 1988 and 2008. The study goes on to further show that corrosion is the leading cause of all incidents involving hazardous

liquid or gas transmission within that time period.<sup>8</sup> These incidents can be especially dangerous as corrosion-related pipeline failures can lead to serious injury or death.

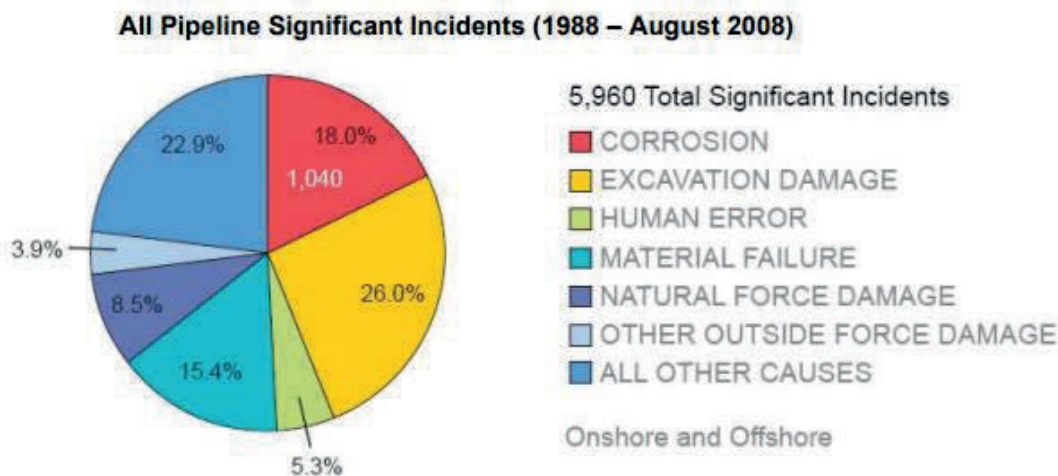


Figure 1. Causes of significant incidents in onshore and offshore pipelines (reproduced “fair use” from Federal government publication)<sup>8</sup>

### 1.3 Laboratory Experimentation Techniques

The majority of corrosion analysis techniques used in laboratories typically rely on small scale experiments using rotating specimens or, more atypically, larger equipment intended to model the pipeline environment more accurately. The conceived flowtube apparatus that is the subject of this thesis represents an improvement on existing techniques to better represent flowing environments for electrochemical testing using a small-scale tabletop design. Currently, laboratory corrosion experiments are frequently performed using either a rotating cylinder electrode (RCE)<sup>10, 11</sup> or a rotating disk electrode (RDE).<sup>11</sup> One of the primary characteristics with these approaches is the

spinning nature of the setup. The fact that a rotating shaft is necessary for the RCE and RDE setups means that there is a sliding contact within the system. This sliding contact can be prone to failure or can potentially cause errors in data collection by introducing electrical noise. Additionally, the centrifugal forces on a rotating specimen may influence the formation of a protective film or may prevent adherence of corrosion products and scales thereon, different than in a pipe flow environment;<sup>12</sup> unwanted vibration can be also postulated to occur that adversely impacts conducted experiments. The flowtube apparatus solves these issues by eliminating the rotating shaft and specimen.

The flowtube apparatus is also comparable to the Thin Channel Flow Cell (TCFC) developed previously by the ICMT. The flowtube is, however, of smaller scale and simpler design. Both sets of experimental equipment are used to develop specific characteristics of a flowing environment similar to that experienced in the field; the TCFC is designed to take wall shear stress into account.<sup>13,14</sup> The main benefit to the flowtube apparatus is its size, since the TCFC is a larger piece of equipment compared to the portable tabletop design of the flowtube. This smaller size combined with design features means fewer reagents are employed, less waste is generated, and cleaning is more straightforward, minimizing costs as well as decreasing downtime between experiments. Cleaning is a critical step when corrosion inhibition experiments are conducted in flow systems and can be especially challenging. Additionally, a flowtube style apparatus can readily fit into an autoclave for testing in high temperature/pressure environments. A schematic representation of the flowtube is shown in Figure 2 below.

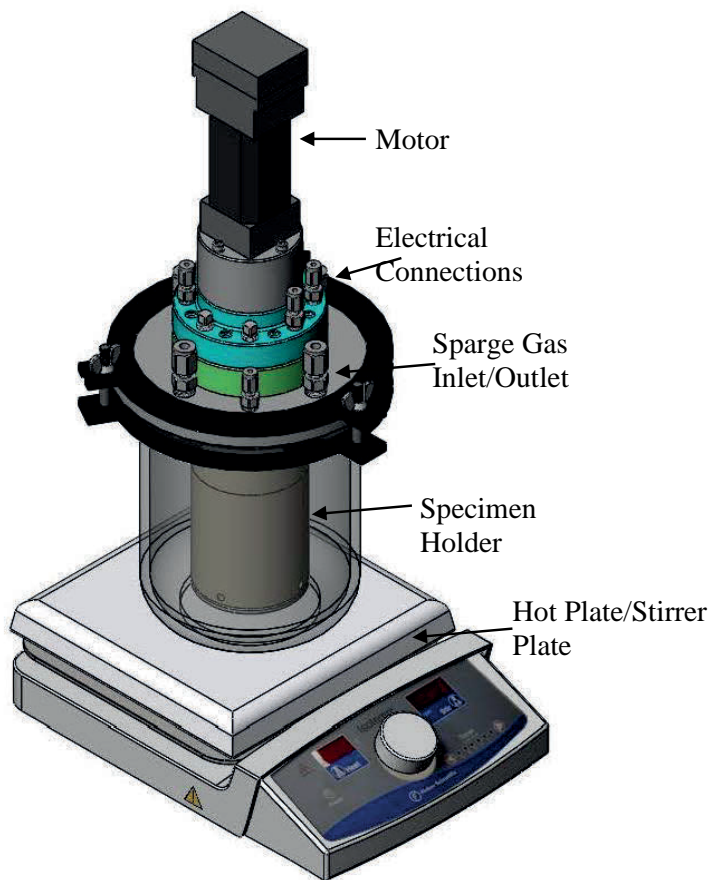


Figure 2. Schematic representation of flowtube apparatus in a 2-liter glass cell (Albert Schubert)

The flowtube uses an impeller located above the specimen holder to draw the aqueous electrolyte up through the flowtube and past the specimens. The hollow cylindrical specimens are stationary, and the aqueous phase contacts their inner surface. This mimics single phase pipe flow that steel, or other metals, may experience in a pipeline. A counter electrode is placed in the center of the specimen holder and extends past all internal specimens. This creates flow through an annulus, which has similar characteristics to full pipe flow, although flow through an annulus exhibits the transition

from laminar flow to turbulent flow at a lower volumetric flow rate. This is validated because the Reynolds number indicates a transition between laminar and turbulent flow at the same flow velocity.<sup>15</sup> Furthermore, the Navier-Stokes equations can be applied to this system to determine the anticipated shear stress profile. Based on these comparisons, it can be shown that a cylindrical pipeline with the same diameter as the annulus will experience very similar wall shear stress near the wall at low pressure drop environments, such as those within the flowtube. It is believed that this flow geometry is sufficient in simulating an adequate estimate of pipeline flow. The design may also be changed as the apparatus is further developed, so it remains a possibility that the flow geometry will be slightly altered. A schematic of the internal components of the original flowtube that was foundational to the research described herein is shown in Figure 3 below.

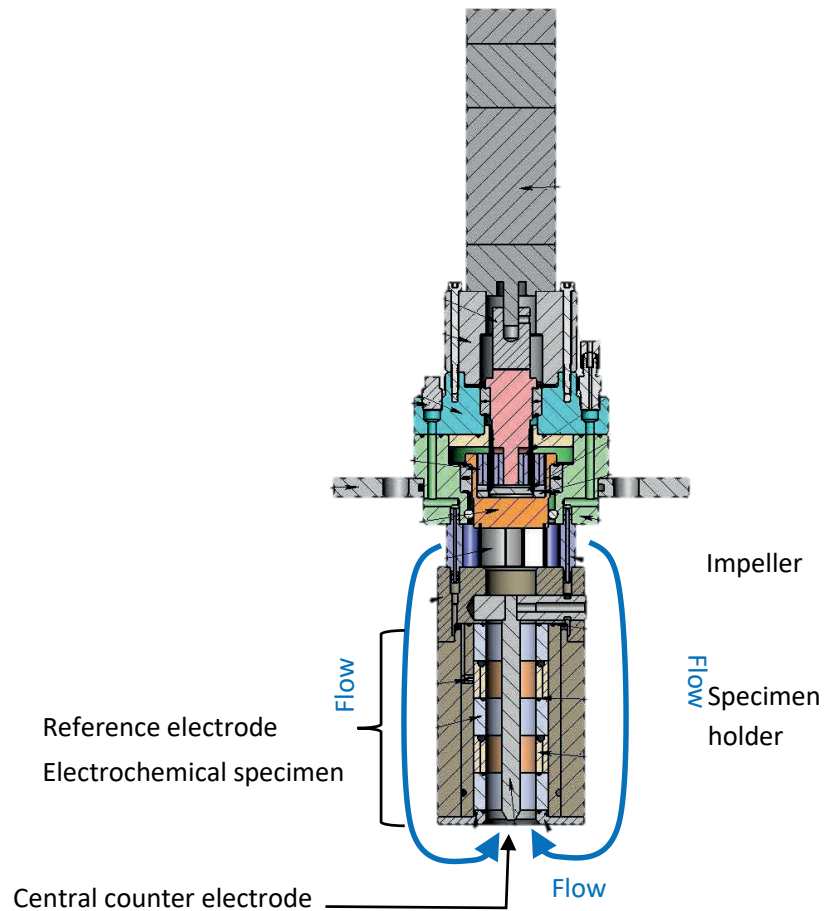


Figure 3. Schematic representation of flowtube internal components (Albert Schubert)

As reported in this thesis, this representation of the internal structure of the flowtube has been utilized in modeling the flowtube using computational fluid dynamics (CFD) in order to analyze the flow patterns surrounding the flowtube apparatus in a glass cell environment. These simulations will aid in the future design of a new working flowtube. These CFD simulations also allow for mass transfer and corrosion to be modeled, which are especially useful for the intended application of the flowtube apparatus.

The flowtube apparatus, which is the focus of the research, has a history of sporadic development and testing up until this point. It was originally conceived by Prof. Srdjan Nestic and initially designed by ICMT Research Engineer Albert Schubert in early 2013. The first prototype was not built or tested until the middle of 2015. Between late 2015 and the middle of 2016, electrochemical tests were performed roughly once per month using the flowtube cell. However, by June 2016 data collection became unreliable due to persistent issues with the reference electrode. At this point, ICMT alumnus Dr. Marijan Babic began to work with the apparatus prior to his graduation from Ohio University. Dr. Babic began working with a revised version of the reference electrode and performed similar tests to those performed in this thesis research. Dr. Babic ran experiments using an RCE and then repeated the tests using the flowtube in order to verify results for design validation. These tests were run until March 2017 when the recurring problems with the reference electrode impeded future progress. Work with the flowtube was then later picked up by Dr. Oladeji Ige, who worked with the apparatus during the Spring and Summer of 2019 as a visiting scholar at the ICMT. Dr. Ige performed several corrosion tests in CO<sub>2</sub> and N<sub>2</sub> environments. Dr. Ige noted at the end of the experiments that further work needs to be done in order to properly model corrosion phenomena in the flowtube; output from existing models deviated from the reported results from Dr. Ige's experiments. Dr. Ige created an internal presentation detailing his findings, however, there is no published work due to the lack of substantial advancement on the flowtube project at the time.

It should be noted that the prototype version of the flowtube referenced above is no longer in working order. In September 2021, the casing around the specimen holder partially detached from the upper housing of the flowtube, as shown in Figure 4 below. This exposed the internal electrical components of the flowtube to the electrolyte solution. A reaction occurred between the internal components of the flowtube and the electrolyte solution which turned the solution a blue color, potentially a copper species, and rendered the flowtube inoperable. The flowtube was then disassembled in order to salvage components that could be used in the next prototype version, as well as better understand the inner workings of the device. Designs for a new version are in development, but no physical prototype has been developed at the time of writing this thesis.

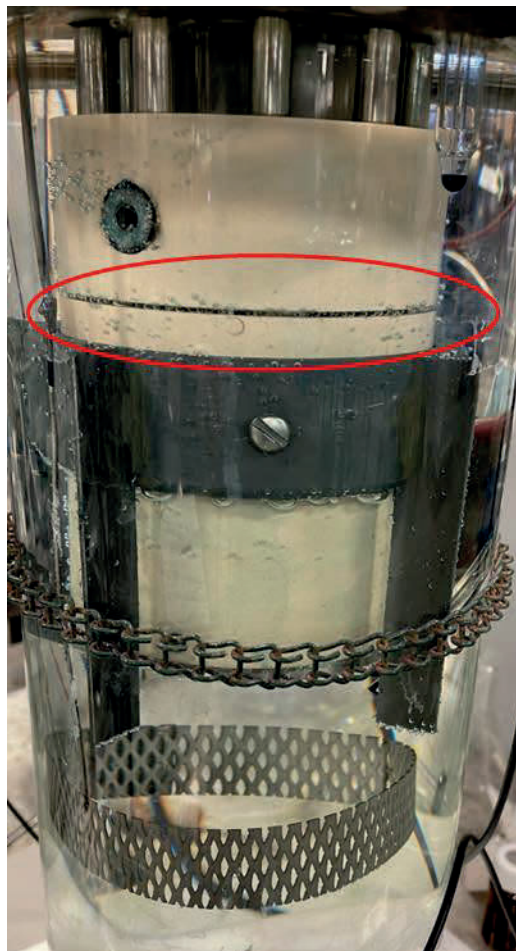


Figure 4. Flowtube specimen holder separation from upper housing

Moving forward, the intention is to advance the flowtube apparatus towards a reliable, well characterized working order for electrochemical testing. To begin, mass transfer testing has been performed using an RCE. These tests are already well defined, which allows for verification of electrochemical testing techniques and a vital learning experience so as to understand what the expected results may look like when using the flowtube. Specifically for the mass transfer tests, Eisenberg has developed an accepted Sherwood correlation to model the mass transfer characteristics of a ferricyanide-

ferrocyanide solution with a nickel electrode in a hydrodynamically smooth cylinder.<sup>19</sup> After validating these results using a RCE, the flowtube apparatus is then used to verify that it can produce expected results for mass transfer coefficients. This verifies that the flowtube apparatus is functional for future electrochemical experiments. Once the mass transfer correlation is verified, corrosion testing is to begin in N<sub>2</sub> and CO<sub>2</sub> environments.

There is potential concern regarding electrolyte characteristics and specimen surface areas within the flowtube apparatus. Concern regarding electrolyte characteristics is due to potential changes in water chemistry deriving from evolution of particular corrosion-related species during experiments, such as elevated levels of ferrous ions and/or deviations in pH; this is a concern within the flowtube in the same way that it would be a concern in any other experimental apparatus while testing many corroding specimens simultaneously. Concern regarding specimen surface area stems from the fact that each specimen is designed to have a surface area of 15.2 cm<sup>2</sup> contacting the aqueous electrolyte. The current design of the flowtube allows for its use in a 4-liter glass cell; only about three liters of water are able to be added due to its displacement due to insertion of the flowtube apparatus therein. Based on this design, the solution volume to specimen surface area ratio is expected to be >60 mL/cm<sup>2</sup>, which exceeds the minimum ratio of 40 mL/cm<sup>2</sup> noted in ASTM Standard G31 (Corrosion Testing) Section 8.9.2.<sup>20</sup> To remedy any possible incident under different design conditions, the size of specimens could be decreased to reduce the surface area contacting the water. Another possible solution could be to only test one specimen at a time rather than the three-specimen configuration currently being explored in the flowtube apparatus. However, an alternative

approach would be to use a double cell system. The second cell could potentially be used to adjust water chemistry, as necessary. This double cell system allows for the use of ion exchange resins to potentially be used to remove aqueous species related to corrosion from the electrolyte. There are a multitude of possible solutions that can be implemented using the flowtube apparatus since it generates pressure driven flow. While the double cell system was not an original thought, the ability to apply this idea highlights the versatility of the flowtube apparatus for corrosion investigations.

## **Chapter 2: Objectives and Research Questions**

The long-term objective, extending past this thesis, is continuous development of the flowtube apparatus and utilize it to perform corrosion tests. The flowtube apparatus is intended to provide a new method for a controlled single phase flow regime in a glass cell or autoclave. A primary research objective, and the main thrust of this thesis, is to model the flowtube using Computational Fluid Dynamics (CFD) software and aid in design of the next prototype version by modeling design considerations. These objectives will be achieved by addressing the following research questions:

- What design considerations would allow for the simplest version of the flowtube while retaining the desired functionality?
- What impeller rotational speeds are required to achieve the desired Reynolds number within the specimen holder?
- How do components such as external baffles and internal flow straightener impact the fluid flow around and within the flowtube?

### Chapter 3: Safety

Chemical hazards associated with this research include working with chemicals such as potassium ferricyanide, potassium ferrocyanide, hydrochloric acid, sodium hydroxide, isopropanol, and sodium chloride. As such, gloves must be worn at all times working with these chemicals. Eye protection must also be worn in the lab at all times. Chemicals used in the lab should not be inhaled; in addition to masks being worn for COVID-19 safety helping to aid in preventing inhalation of chemicals, all efforts should still be made to avoid potential inhalation. It should be noted that masks were no longer required as a COVID-19 safety precaution after all RCE testing was completed but before RDE testing was started. Before experiments are conducted or if contact with a chemical occurs, the safety data sheet (SDS) for that chemical should be referenced for specific instructions for handling and disposal; in all cases the affected area should be rinsed with water if it is external to remove the chemical. After handling any chemicals, hands should be washed thoroughly.

When assembling the glass cell or dealing with other glassware, special attention should be paid to ensure it is not dropped or otherwise damaged. Broken glassware causes a hazard within the lab and should be disposed of in clearly marked glass waste disposal containers. When placing the glass cell on the hot plate/stir plate, it should be attached to a support rod using a chain. This helps to ensure that the glass cell cannot be bumped from the hot plate. A purge line is installed in the glass cell to ensure that it does not get pressurized by the gas inlet line.

Any electrical wires connected to or near the equipment should be inspected to ensure they are not broken or frayed in any way. Additionally, they should be placed away from the hot plate surface to ensure their coating does not melt if the hot plate were to be turned on.

When handling the flowtube, special attention should be paid not to drop the apparatus, since it is heavy and could cause damage to person or property if dropped as well damaging the apparatus. If the flowtube is turned on, nothing should be placed near the impeller or the opening at the bottom of the specimen holder to avoid potential injury. When operating the flowtube, the voltage from the controller should not exceed 1.2 V; if this limit is exceeded a fuse will be blown. When operating the flowtube, care should be taken to ensure that water does not come into contact with any electrical components.

For all tests performed in a glass cell, the chemicals used in the concentrations required may be disposed of by pouring the electrolyte solution down a sink drain within the lab. If there is any doubt as to whether the chemical/solution may be disposed of via the plumbing system, the SDS should be referenced. If any test involves the use of inhibitors, the electrolyte solution should be disposed of in the waste container designated for inhibitor waste.

## Chapter 4: Corrosion and Mass Transfer Results

### 4.1 Preliminary RCE Experiments

#### 4.1.1 *Equipment*

- 2 L glass cell
- Stir bar
- N<sub>2</sub> gas line
- CO<sub>2</sub> gas line
- Pine rotator
- Gamry potentiostat
- Counter electrode
- Saturated KCl Ag|AgCl reference electrode
- Luggin capillary
- RCE shaft
- Ni RCE specimen
- 1018 mild steel RCE specimen

#### 4.1.2 *Experimental Apparatus*

Mass transfer and corrosion experimentation were performed in a 2 L glass cell on a hot plate/stirrer plate. The glass cell was sparged with N<sub>2</sub> gas before experiments were performed for mass transfer experimentation to facilitate deoxygenation. For corrosion experiments, the cell was sparged with N<sub>2</sub> gas for one set of experiments and CO<sub>2</sub> gas for the second set of experiments. All experiments were performed using a rotating cylinder electrode.

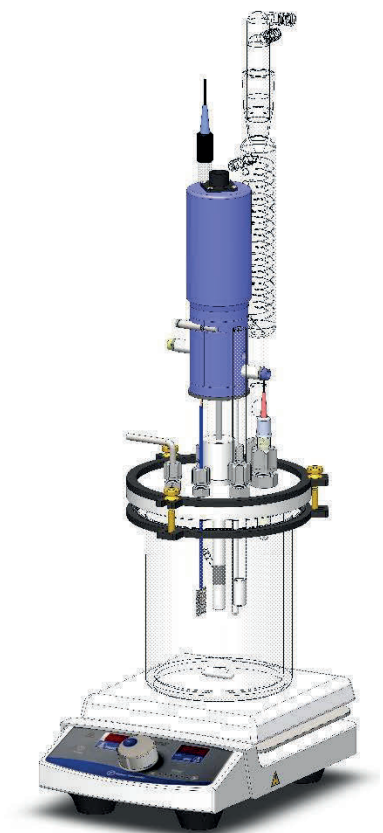


Figure 5. 2 L glass cell set up for RCE experimentation (Cody Shafer)

#### ***4.1.3 Materials Tested***

Mass transfer experiments were performed using a ferricyanide/ferrocyanide solution with a nickel RCE specimen.

Corrosion experiments were performed using a 1018 mild steel RCE specimen.

Compositional data is shown in Appendix C: Material Composition Data.

#### 4.1.4 Test Matrices

Table 2. Test Matrix for RCE Mass Transfer Experimentation

Parameter	Conditions
Material & Working Electrode Characteristics	Ni Surface Area: 5.25 cm <sup>2</sup> Density: 8.79 g/cm <sup>3</sup>
Temperature	30°C
Partial Pressure (N <sub>2</sub> )	0.97 bar
Electrolyte	0.5 M of NaOH 0.01 M of K <sub>3</sub> Fe(CN) <sub>6</sub> 0.01 M of K <sub>4</sub> Fe(CN) <sub>6</sub> ·3H <sub>2</sub> O
RCE Speed	500, 1000, 1500, 2000, 6000 RPM
Electrochemical Techniques	Potentiodynamic Sweep <ul style="list-style-type: none"> <li>• 0.4 V above E<sub>oc</sub> (Anodic)</li> <li>• 1.7 V below E<sub>oc</sub> (Cathodic)</li> <li>• Scan Speed: 5 mV/s</li> </ul>

Table 3. Test Matrix for RCE Corrosion Experimentation

Parameter	Conditions
Material & Working	1018 #5 Mild Steel
Electrode Characteristics	Surface Area: 5.37 cm <sup>2</sup> Density: 7.785 g/cm <sup>3</sup>
Temperature	35°C
Partial Pressure (N <sub>2</sub> or CO <sub>2</sub> )	0.96 bar
Electrolyte	1 wt.% NaCl pH adjusted with HCl or Na <sub>2</sub> CO <sub>3</sub>
pH	4.0±0.1, 5.0±0.1, 6.0±0.1
RCE Speed	500, 1000, 1500, 2000, 6000 RPM
Electrochemical Techniques	<p>LPR</p> <ul style="list-style-type: none"> <li>• 5 mV above E<sub>oc</sub> (Anodic)</li> <li>• 5 mV below E<sub>oc</sub> (Cathodic)</li> <li>• Scan Speed of 0.125 mV/s</li> </ul> <p>Potentiodynamic Sweep</p> <ul style="list-style-type: none"> <li>• 0.1 V above E<sub>oc</sub> (Anodic)</li> <li>• 0.5 V below E<sub>oc</sub> (Cathodic)</li> <li>• Scan Speed of 0.125 mV/s</li> </ul> <p>EIS</p> <ul style="list-style-type: none"> <li>• 5000 Hz to 0.1 Hz</li> </ul>

#### **4.1.5 Procedure**

**4.1.5.1 Ferri-/Ferro- Cyanide Mass Transfer Experiments.** To begin, a solution was made in a 2 L glass cell according to the specifications of 0.5 M sodium hydroxide, 0.01 M potassium ferricyanide, and 0.01 M potassium ferrocyanide in 2 L of deionized water. In order to achieve these concentrations, it was determined that 39.997 g sodium hydroxide, 6.585 g potassium ferricyanide, and 8.448 g potassium ferrocyanide needed to be added to the 2 L of deionized water in the glass cell. This solution was used for all mass transfer experiments. The 2 L glass cell containing the solution was placed on a hot plate/rotator. The glass cell was covered in an insulation wrapper in order to also keep light out of the cell; this is because “in alkaline solutions kept in darkness, the decomposition of cyanide complexes is practically eliminated.”<sup>19</sup>

Prior to data collection, the solution temperature was raised to 30°C and deoxygenated with nitrogen sparging. In order to ensure even distribution of dissolved species and temperature, a stir bar was utilized. During the heating and nitrogen sparging, the stir bar was set to 350 RPM. During this time, it should be noted that the RCE shaft was not inserted in the glass cell; a rubber stopper was utilized to ensure an airtight environment while the nitrogen sparge and solution heating were taking place. The nitrogen gas line was opened in order to allow for the nitrogen sparge. The flow of nitrogen was observed through the gas-out line, which was fed into an Erlenmeyer flask partially filled with water to ensure gas could not enter the system once it was expelled. For the sparging to facilitate deoxygenation, the rate of bubbling in this Erlenmeyer flask was observed. When the rate of bubbles was constant and at a rate slow enough to be

counted visually, it was determined that the nitrogen flow rate was appropriate for the sparge. Once the temperature on the hot plate was set to 30°C, the stir bar was set to 350 RPM, and the nitrogen gas flow rate was deemed acceptable, the glass cell was left for approximately 4 hours or until the solution temperature reached 30°C, whichever came first.

After the solution was brought to temperature and the nitrogen sparge was complete, the nitrogen gas flow rate was decreased to the minimum rate where the outlet line produced a constant rate of bubbles. Also, the stir bar was turned off so it would not interfere with any data collection. At this point, the nickel RCE specimen was polished using 600 grit abrasive paper on a drill press to ensure even polishing. Once polished, the nickel electrode was installed onto the RCE shaft. The RCE shaft was then inserted into the Pine<sup>TM</sup> rotator. The rubber stopper on the glass cell lid was then removed and replaced with the RCE shaft. The electrical connections to the Gamry potentiostat were then affixed to the Pine<sup>TM</sup> rotator, counter electrode, and reference electrode as described in the procedure for using the Gamry potentiostat. At this point, data collection was able to begin.

The Pine rotator was set to 500 RPM, and this rotational speed was verified using a light tachometer. Once the rotational speed was set, the Luggin capillary was examined to be sure there were no air bubbles, and it was as close as possible to the rotating specimen without touching. Adjustments were then made as necessary in order to ensure a proper and reproducible experimental setup. Once this was done, an open circuit potential (OCP) experiment was performed. The OCP test was allowed to run for 10

minutes to ensure that recorded values were stable. The OCP was considered to be stable if the potential value did not vary by greater than 0.001 V vs the reference electrode for at least 30 seconds. After this, potentiodynamic sweeps were performed.

For the potentiodynamic sweeps, the initial voltage was set to 0 V vs.  $E_{oc}$ , scan rate was set to 5 mV/s, sample period was set to 1 s, sample area was set to 5.25 cm<sup>2</sup>, density was set to 8.79 g/cm<sup>3</sup>, and the initial delay was set to 600 s. Final voltage was set to -1.7 V vs.  $E_{oc}$  for the cathodic sweeps and was set to 0.4 V vs.  $E_{oc}$  for anodic sweeps. For all potentiodynamic sweeps, cathodic sweeps were performed directly before anodic sweeps. When the experimentation started, the initial delay allowed OCP data collection. This OCP measurement was allowed to run for at least 2 minutes prior to each experiment. After 2 minutes, the OCP was observed to determine if it had stabilized. Once the OCP appeared stable, the remaining time on the initial delay was skipped and the potentiodynamic sweep was allowed to take place. All potentiodynamic sweeps were allowed to run until completion. The procedure for potentiodynamic sweeps was repeated for the anodic sweep at the same rotational speed as the cathodic sweep immediately after the cathodic sweep was performed. Once both the cathodic and anodic sweeps were performed for a given rotational speed, the rotational speed was changed to the next desired speed, the rotator speed was verified with a light tachometer, and the potentiodynamic sweeps were performed for the new rotational speed. This procedure was repeated for 500 RPM, 1000 RPM, 1500 RPM, 2000 RPM, and 6000 RPM. Two independent sets of data were collected.

Once experimentation was completed shutdown procedure was as follows. The Gamry potentiostat electrical connections were disconnected from the Pine rotator, counter electrode, and reference electrode. The Pine rotator was then removed from the glass cell; the rubber stopper was inserted in the lid to replace the rotator shaft. The rotator shaft was wiped down with a paper towel to ensure excess solution did not remain. The nickel RCE was then removed from the shaft; the inside of the specimen was examined to ensure moisture did not leak behind it. The nickel RCE was then placed in a specimen bag. The hot plate was then turned off and the nitrogen gas line was turned completely off.

**4.1.5.2 1018 Mild Steel Corrosion Experiments.** To begin, a 1 wt.% NaCl electrolyte was prepared in a 2 L glass cell by dissolving 20.115 g of NaCl in 2 L of deionized water, the glass cell was then placed on a hot plate/magnetic stirrer. This aqueous electrolyte was used for all subsequent experiments.

Sparging the solution with nitrogen was performed following the same procedure that was used with the ferri-/ferro- cyanide experiments above. Through use of an Orbisphere<sup>TM</sup> 410, it was determined that this was an adequate amount of time to ensure oxygen concentration was below 10 ppb. The Orbisphere<sup>TM</sup> was removed from the setup once it was determined that there was no oxygen ingress, all data was collected after the Orbisphere<sup>TM</sup> was removed. Any time the lid was opened to insert the shaft or adjust the pH, the nitrogen flow rate was increased for approximately 30 seconds before the seal was broken. The higher nitrogen flow rate was reduced back to the previously established rate about a minute after the seal was made on the lid, again to ensure oxygen ingress did

not occur. The RCE shaft was installed into the Pine rotator during the sparge, where it remained for the duration of experimentation. After the solution was brought to temperature and the nitrogen sparge was complete, the stir bar was turned off so it would not interfere with any data collection.

When the solution was nearly at temperature, the 1018 mild steel RCE specimen was polished using 600 grit abrasive paper on a drill press to ensure even polishing. Deionized (DI) water was sprayed on the specimen as it was being polished. The interior of the specimen was polished by wrapping the 600-grit abrasive paper around the screw used to attach it to the drill press; it was inserted into the center of the specimen and rotated by hand to polish the inside surface. After polishing the exterior and interior of the specimen, it was sprayed with isopropyl alcohol. It was then cleaned with the ultrasonic cleaner using the following procedure. The specimen was placed in a beaker and filled to just above the height of the specimen with isopropyl alcohol. The beaker was placed in the center of the ultrasonic cleaner. The ultrasonic cleaner was adjusted to the 50 W setting and set for 4 minutes. Once the cleaning was complete, the specimen was removed from the isopropyl alcohol using plastic forceps. The forceps were inserted in the middle of the specimen to ensure no contact with the surface that will undergo corrosion. The specimen was placed onto a paper towel to allow any remaining isopropyl alcohol to dry. Once polished and cleaned, the 1018 mild steel specimen was installed onto the RCE shaft while still in the paper towel to avoid contamination from the gloves being worn. The rubber stopper on the glass cell lid was then removed and replaced with the RCE shaft. The electrical connections to the Gamry potentiostat were then connected

as described in the mass transfer experimentation section. The pH of the solution was measured and decreased using 0.1 M HCl solution. For the first set of experiments, the desired pH was 4.00, so the HCl was added until the pH was  $4.00 \pm 0.02$ . If it was necessary to raise the pH, 0.1 M  $\text{Na}_2\text{CO}_3$  solution was used. During each experiment, the pH was adjusted when it changed outside a tolerance of  $\pm 0.1$  pH units. Any HCl or  $\text{Na}_2\text{CO}_3$  added to the solution was noted in the lab notebook. At this point, data collection was able to begin.

The Pine<sup>TM</sup> rotator was set to 1000 RPM, and this rotational speed was verified using a light tachometer. Once the rotational speed was set, the procedure described above for mass transfer testing was followed to prepare the system for an open circuit potential (OCP) experiment. This OCP experiment was performed similar to the ferri-/ferro- cyanide experiments above. As above, the OCP was considered to be stable if the potential value did not vary by greater than 0.001 V vs the reference electrode for at least 30 seconds. It should be noted that if the pH fluctuated between experiments, then it was adjusted using either HCl or  $\text{Na}_2\text{CO}_3$  (whichever was applicable); pH adjustments were not made while an experiment was being performed.

For the LPR experiments, the initial voltage was set to  $-0.005$  V vs.  $E_{oc}$ , the final voltage was set to  $0.005$  V vs.  $E_{oc}$ , the scan rate was set to  $0.125$  mV/s, the sample period was set to 1 s, sample area was set to  $5.37$  cm<sup>2</sup>, density was set to  $7.785$  g/cm<sup>3</sup>, and the initial delay was set to 600 s. The initial delay allowed an additional OCP test to run. This OCP was allowed to run for at least 2 minutes prior to each experiment. After 2 minutes, the OCP was observed to see if it had stabilized, using the same criteria for stabilization

described above. Once the OCP appeared stable, the remaining time on the initial delay was skipped and the LPR experiment was allowed to take place.

For the potentiodynamic sweeps, the parameters were set as follows: the initial voltage was set to 0 V vs.  $E_{oc}$ , scan rate was set to 0.125 mV/s, sample period was set to 1 s, sample area was set to 5.37 cm<sup>2</sup>, density was set to 7.785 g/cm<sup>3</sup>, and the initial delay was set to 600 s. Final voltage was set to -0.5 V vs.  $E_{oc}$  for the cathodic sweeps. The initial delay followed the same procedure as for the LPR experiments and the potentiodynamic sweep was allowed to take place following its completion. The cathodic potentiodynamic sweep was run until the water reduction line was visible on the curve as a straight line; at that point, the experiment was stopped.

For the potentiostatic EIS experiments, the parameters were set as follows: the initial frequency was set to 5000 Hz, the final frequency was set to 1 Hz, points/decade was set to 8, the AC voltage was set to 5 mV rms, DC voltage was set to 0 V vs.  $E_{oc}$ , sample area was set to 5.37 cm<sup>2</sup>, and the initial delay was set to 600 s. The initial delay again followed the same procedure as for the LPR and potentiodynamic sweeps. The EIS experiment was allowed to take place following the initial delay.

The procedure for anodic potentiodynamic sweeps was nearly identical to the procedure for the cathodic potentiodynamic sweeps. The OCP of the anodic sweep was desired to be within a tolerance of  $\pm 10$  mV of the corresponding cathodic sweep. If the OCP was outside of this range and stable, the experiment could not proceed. The only difference in the experimental setup parameters was that the final voltage was set to 0.1 V vs.  $E_{oc}$  for anodic sweeps. When the experimentation started, the initial delay was

performed as previously described and the potentiodynamic sweep was allowed to take place. The anodic potentiodynamic sweeps were allowed to run to completion.

The order of experiments was as follows. The first experiment to be performed was an OCP test. After the OCP test was complete and stable, the rotator was stopped so a visual inspection could be performed. During this visual inspection, it was verified that uniform corrosion appeared to be occurring on the surface of the 1018 mild steel specimen. After that, the rotator was turned back on and an LPR experiment was performed. After the first LPR measurement, the specimen was allowed to continue rotating in solution for 30 minutes. After 30 minutes, a second LPR experiment was performed to verify reproducibility and ensure a film had not formed on the surface of the specimen. Reproducibility for these experiments allowed for a tolerance of  $\pm 0.2$  mm/year for the corrosion rate. After that, an EIS experiment was performed. After the EIS experiment, a cathodic potentiodynamic sweep was performed. Following the cathodic potentiodynamic sweep, another OCP test was performed to ensure the open circuit potential returned to the same value  $\pm 5$  mV it had been at prior to the cathodic potentiodynamic sweep. Once the OCP did not fluctuate by more than 0.001 V over 30 seconds, LPR, EIS, and cathodic potentiodynamic sweep experiments could be performed again following the above procedure. After all desired experimentation was completed, the last experiment performed was an anodic potentiodynamic sweep. By performing this experiment last, corrosion of the specimen due to the anodic potentiodynamic sweep would not affect the specimen or solution for any other experiments.

Two independent sets of data were collected. Once two reproducible cathodic sweeps were obtained, the rotational speed was changed to the next desired speed, the rotator speed was verified with a light tachometer, and the electrochemical experiments were performed for the new rotational speed. This procedure was repeated for 500 RPM, 1000 RPM, 1500 RPM, and 2000 RPM. Once all rotational speeds were tested, the experimentation was complete for that pH. The above procedure was repeated for pH values of 4.00, 5.00, and 6.00. After all experiments were performed twice at all rotational speeds at all pH set points, the sparge gas was changed to CO<sub>2</sub> and all experiments were performed again using the CO<sub>2</sub> saturated environment. It should be noted that each pH or sparge gas experimental condition was established in a new solution each time. The shutdown procedure for these experiments is identical to the shutdown procedure implemented for ferri-/ferro- cyanide experiments.

After all experimentation was complete for the day or the solution needed to be replaced for other reasons, the procedure to clean the glass cell is as follows. The lid was removed from the glass cell and placed to the side, and usually propped up using the sparge tube to avoid pressure on the thermocouple, Luggin capillary, or counter electrode. The thermocouple, Luggin capillary, and counter electrode were sprayed with deionized water and then dried with a paper towel to ensure they were clean. The glass cell was removed from the hot plate after removing the chain, and the contents were disposed of as appropriate. The glass cell was then rinsed with DI water. If discoloration of the solution occurred or there was another apparent need for a more complete clean, hand soap was pumped into the glass cell which was filled approximately halfway with

DI water. The soap mixture was then rubbed over all surfaces of the glass cell and stir bar by hand. The soap mixture was then dumped down the drain, and the glass cell was rinsed out three times with DI water to ensure essentially all the soap was removed. After it was rinsed with DI water, the glass cell was then rinsed with isopropyl alcohol to eliminate any remaining residual soap. The isopropyl alcohol was then dumped out and the glass cell was rinsed one more time with DI water. After this, wet surfaces and the stir bar were dried with paper towels and the glass cell was reattached to the hot plate using the chain to hold it in place. The lid was then placed back on the glass cell and tightened. Prior to leaving for the night, DI water was put inside the glass cell to ensure the Luggin capillary did not dry out. If time permitted prior to leaving the lab for the evening, 20.115 g of NaCl was added to 2 L of DI water in the glass cell so the solution would be ready for experimentation the following day. Otherwise, the glass cell was filled with DI water to ensure the Luggin capillary did not dry out overnight, and the solution was made in the morning prior to the nitrogen or carbon dioxide sparge.

## 4.2 Preliminary RDE Experiments

### 4.2.1 *Equipment*

- 1 L glass cell
- Stir bar
- CO<sub>2</sub> gas line
- Pine rotator
- Gamry potentiostat
- Counter electrode
- Saturated KCl Ag|AgCl reference electrode
- Luggin capillary
- RDE shaft
- E4 ChangeDisk™ Internal Contact Pin
- PCTFE E4 ChangeDisk™ Body
- PTFE ChangeDisk™ RDE Tip
- X65 mild steel RDE specimen

### 4.2.2 *Experimental Apparatus*

Corrosion experimentation was performed in a 1 L glass cell on a hot plate/stirrer plate. The glass cell was sparged with CO<sub>2</sub> gas before experiments were performed. All experiments were performed using a rotating disk electrode.



Figure 6. 1 L glass cell set up for RDE experimentation (Cody Shafer)

#### **4.2.3 *Materials Tested***

Corrosion experiments were performed using an X65 mild steel RDE specimen.

Compositional data is shown in Appendix C: Material Composition Data.

#### 4.2.4 Test Matrix

Table 4. Test Matrix for RDE Corrosion Experimentation

Parameter	Conditions
Material & Working	X65 Mild Steel
Electrode Characteristics	Surface Area: 0.193 cm <sup>2</sup>
Temperature	30°C
Partial Pressure (CO <sub>2</sub> )	0.97 bar
Electrolyte	1 wt.% NaCl pH adjusted with HCl or Na <sub>2</sub> CO <sub>3</sub>
pH	4.0±0.1
RDE Rotational Speed	250, 500, 1000, 2000, 4000, 8000 RPM
Electrochemical Techniques	<p>LPR</p> <ul style="list-style-type: none"> <li>• 5 mV above E<sub>oc</sub> (Anodic)</li> <li>• 5 mV below E<sub>oc</sub> (Cathodic)</li> <li>• Scan Speed of 0.125 mV/s</li> </ul> <p>Potentiodynamic Sweep</p> <ul style="list-style-type: none"> <li>• 0.1 V above E<sub>oc</sub> (Anodic)</li> <li>• 0.4 V below E<sub>oc</sub> (Cathodic)</li> <li>• Scan Speed of 0.125 mV/s</li> </ul> <p>EIS</p> <ul style="list-style-type: none"> <li>• 5000 Hz to 0.1 Hz</li> </ul>

#### ***4.2.5 Procedure***

To begin, a 1 wt.% NaCl electrolyte was prepared in a 1 L glass cell by dissolving 10.057 g of NaCl in 1 L of deionized water, the glass cell was then placed on a hot plate/magnetic stirrer. This aqueous electrolyte was used for all subsequent experiments.

Sparging the solution with carbon dioxide was performed following the same procedure that was used with the RCE experiments above. The glass cell was allowed to sparge for at least 30 minutes before experimentation began. During this time, the sparge tube was inserted nearly to the bottom of the glass cell to ensure the gas bubbles were able to dissolve into solution as effectively as possible. Immediately before experimentation, the sparge tube was moved so it was nearly at the top of the liquid level in the glass cell. It was important to keep the sparge tube as far away from the RDE tip as possible so that bubbles did not form as easily on the RDE specimen. Anytime the lid was opened to insert the shaft or adjust the pH, the same procedure was followed as the RCE experiments to minimize the amount of oxygen within the system. The RDE shaft was installed into the Pine rotator during the sparge, where it remained for the duration of experimentation. After the solution was brought to temperature and the carbon dioxide sparge was complete, the stir bar was turned off so it would not interfere with any data collection.

When the solution was nearly at temperature, the X65 mild steel RDE specimen was polished according to the Procedure detailed in Appendix A: Additional Experimental Methodology. Once polished and cleaned, the RDE tip was installed onto the RDE. The rubber stopper on the glass cell lid was then removed and replaced with the

RDE shaft. The electrical connections to the Gamry potentiostat were then connected as described in the sections for RCE experiments. The pH of the solution was measured and adjusted using the procedure described for RCE experiments until the pH was  $4.00 \pm 0.02$ . Any HCl or  $\text{Na}_2\text{CO}_3$  added to the solution was noted in the lab notebook. At this point, data collection was able to begin.

During experimentation with the RDE, an issue of bubbles forming on the RDE tip was noted. This caused problems with data collection, as bubbles on the RDE specimen surface impeded the ability of the potentiostat to correctly collect data. This issue was especially pervasive at lower rotational speeds. In order to reduce the impact of these bubbles forming, the RDE was visually inspected periodically during experimentation. If bubbles were seen to be forming on or near the bottom surface of the RDE tip, any experiment being performed was paused, the rotational speed was increased until the bubbles were dispelled from the surface, the rotational speed was returned to the desired value, and the experiment was resumed.

The Pine rotator was set to the desired rotational speed, and this rotational speed was verified using a light tachometer. Once the rotational speed was set, the Luggin capillary was examined to ensure there were no air bubbles within it, and it was close to the rotating specimen while also being between the counter electrode and the rotating specimen. Adjustments were then made as necessary in order to ensure a proper and reproducible experimental setup. For example, the counter electrode was checked to ensure that it was parallel to and directly underneath the bottom of the RDE specimen. Once this was done, an open circuit potential (OCP) test was performed as described

above for RCE experiments. It should be noted that if the pH fluctuated between experiments, then it was adjusted in the same manner as it was adjusted for RCE experiments.

For the LPR experiments, the parameters were set the same as they were for the RCE experiments with the exception of the sample area, which was set to  $0.193 \text{ cm}^2$ . The LPR procedure was followed in the same manner as it was described for RCE experimentation. Following this initial LPR, a second LPR experiment was performed for redundancy. For this experiment, the initial voltage was set to  $0.005 \text{ V vs. } E_{oc}$ , the final voltage was set to  $-0.005 \text{ V vs. } E_{oc}$  with all other parameters remaining identical. If the corrosion rate, polarization resistance, corrosion current, and corrosion potential all appeared to be the same between the two LPR runs, the LPR measurements were considered to be successful and complete.

For the potentiodynamic sweeps, the parameters were set to be the same as for RCE experiments with the exception of the sample area, which was set to  $0.193 \text{ cm}^2$ . Final voltage was set to  $-0.4 \text{ V vs. } E_{oc}$  for the cathodic sweeps. The potentiodynamic sweep procedure was followed as it is written for RCE experiments.

For the potentiostatic EIS experiments, the parameters were set exactly as they were for RCE experiments except for the sample area, which was set to  $0.193 \text{ cm}^2$ . The procedure for performing the EIS experiments remains identical to the procedure described in the RCE experimentation section.

The procedure for anodic potentiodynamic sweeps was essentially identical to the procedure for the cathodic potentiodynamic sweeps. The OCP of the anodic sweep was

desired to be within a tolerance of  $\pm 2$  mV of the corresponding cathodic sweep. If the OCP was outside of this range and stable, the experiment could not proceed. The only difference in the experimental setup was that the final voltage was set to 0.1 V vs.  $E_{oc}$  for anodic sweeps. The anodic potentiodynamic sweeps were allowed to run to completion following the procedure described above for RCE experimentation.

The order of experimentation was as follows. The first experiment to be performed was an OCP test. After that, the rotator was turned back on and the LPR experiments were performed. Reproducibility for these LPR experiments allowed for a tolerance of  $\pm 0.2$  mm/year for the corrosion rate. After that, an EIS experiment was performed. After the EIS experiment, a cathodic potentiodynamic sweep was performed. Following the cathodic potentiodynamic sweep, another OCP test was performed to ensure the open circuit potential returned to the same value it had been at prior to the cathodic potentiodynamic sweep. Once the OCP was stable, LPR and cathodic potentiodynamic sweep experiments could be performed again following the above procedure. After all desired experimentation was completed, the last experiment performed was an anodic potentiodynamic sweep. By performing this experiment last, corrosion of the specimen due to the anodic potentiodynamic sweep would not affect the specimen or solution for any other experiments.

Two independent sets of data were collected. Once two reproducible cathodic sweeps were obtained, the anodic potentiodynamic sweep was performed, and the RDE was removed from the solution. Following this, the experiment solution was discarded

and remade before future experimentation. This procedure was repeated for 250 RPM, 500 RPM, 1000 RPM, 2000 RPM, 4000 RPM, and 8000 RPM.

The shutdown procedure for these experiments is nearly identical to the shutdown procedure implemented for RCE experiments. The only noteworthy change is that the specimen bag the RDE specimen was placed into was filled with nitrogen gas prior to being closed/sealed each day. This is to ensure dry air is in contact with the RDE specimen so that corrosion is less likely to occur between days of experimentation.

After all experimentation was complete for the day or the solution needed to be replaced for other reasons, the procedure to clean the glass cell is as follows. The lid was removed from the glass cell and attached to the clamp above the hot plate to avoid pressure on the thermocouple, Luggin capillary, or counter electrode. The thermocouple, Luggin capillary, and counter electrode were sprayed with deionized water and then dried with a paper towel to ensure they were clean. The glass cell was removed from the hot plate, and the post-experiment electrolyte disposed of as appropriate. The glass cell was rinsed with DI water then isopropyl alcohol to eliminate any remaining residues. The isopropyl alcohol was then dumped out and the glass cell rinsed three more times with DI water. After this, wet exterior surfaces were dried with paper towels, and the new experimental solution was created. The glass cell was then placed back on the hot plate. The lid was then placed back on the glass cell and tightened. It should be noted that when the glass cell was left overnight, the experimental solution from the previous day was left in the glass cell to ensure the Luggin capillary did not dry out.

## **Chapter 5: Preliminary Mass Transfer and Corrosion Results and Discussion**

### **5.1 Preliminary RCE Experiments**

#### **5.1.1 *Mass Transfer Experiments***

Potentiodynamic sweep data was collected from the potentiostat, as described in the RCE experimental Procedure section of this thesis and are displayed below in Figure 7. The potentiodynamic sweep data for the anodic sweeps were taken directly following the potentiodynamic sweep data for the cathodic sweeps. This caused a difference in ferricyanide concentration in solution, which caused a different limiting current in the anodic curve compared to the cathodic curve. The difference was more prominent at the lower rotational speeds evaluated. For this reason, the cathodic limiting currents were used for all future discussions and calculations. The limiting current region referenced in Figure 7 and other figures within this thesis refer to the potential range where the electrochemical reaction is limited by charge transfer. This region can be visually identified as a vertical or nearly vertical line within the potentiodynamic sweep data. Figure 7 below shows a clearly defined cathodic limiting current for all rotational speeds evaluated. As the rotational speed was increased, it was shown that the limiting current also increased.

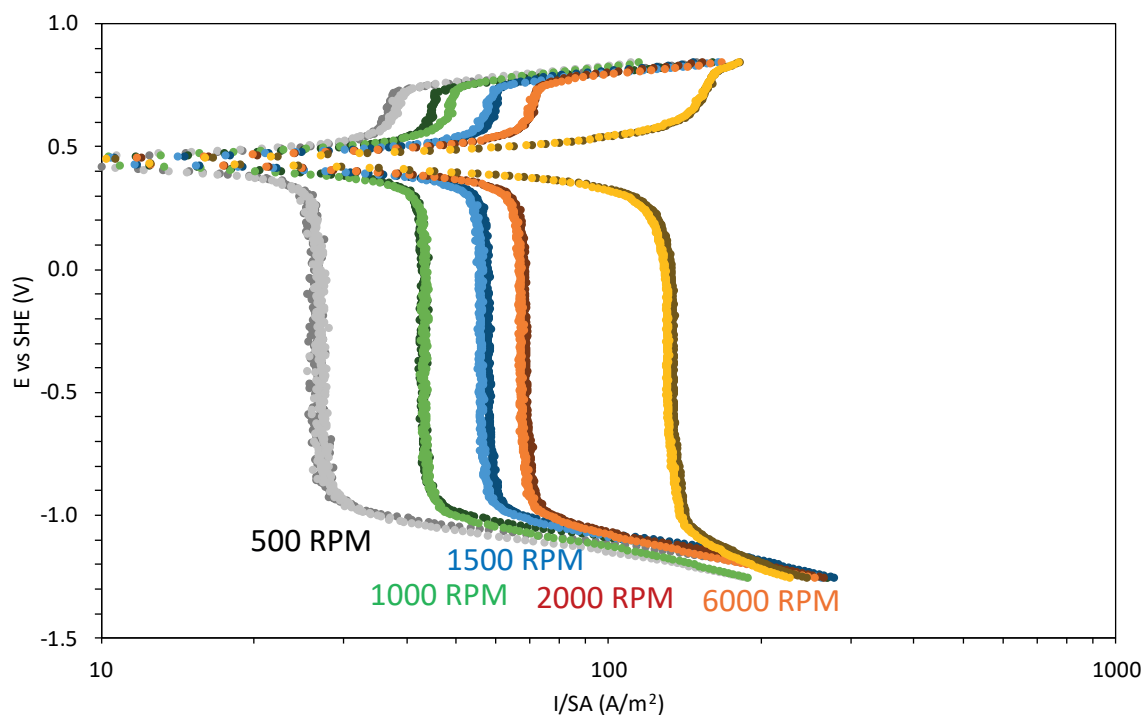


Figure 7. Potentiodynamic sweep data showing the effect of rotational rate on nickel RCE mass transfer in  $N_2$  sparged, 0.01 M ferri-/ferro- cyanide, and 0.5 M NaOH solution at  $30^\circ C$  for 500 RPM, 1000 RPM, 1500 RPM, 2000 RPM, and 6000 RPM rotational rates.

Once the potentiodynamic sweep data was collected, the limiting current was extracted, the rotational speed was converted to pipe velocity by Equation (2), and the mass transfer coefficient was calculated by Equation (1). For the purposes of this analysis, a pipe diameter of 10.1 cm was used for calculations. The results are tabulated in Table 5 below.

Table 5. Superficial Velocity, Limiting Current, and Mass Transfer Coefficient for Each Rotational Speed Examined in Mass Transfer Experimentation

Rotational Speed (RPM)	10.1 cm Diameter Pipe Superficial Velocity (m/s)	Limiting Current ( $A/m^2$ )	$k_m$ (m/s)
500	0.70	26.75	2.77E-05
1000	1.22	43.15	4.47E-05
1500	1.68	56.77	5.88E-05
2000	2.12	67.59	7.01E-05
6000	5.10	130.16	1.35E-04

Using the values shown in Table 5, nondimensional values were calculated using Equations (4), (5), and (6). They are tabulated in Table 6 below.

Table 6. Tabulated Nondimensional Numbers for Mass Transfer Experiments

Rotational Speed	Re	Sc	Sh
500 RPM	5100	841.2	364.0
1000 RPM	10201	841.2	587.2
1500 RPM	15301	841.2	772.6
2000 RPM	20401	841.2	919.8
6000 RPM	61204	841.2	1771.3

In order to compare the experimental correlation to the correlation in Eisenberg's paper, Sherwood Number was plotted as a function of Reynolds Number as shown in Figure 8 below. Eisenberg noted that there was a 7% error in his Sherwood correlation, which is included in Figure 8 as gray lines on either side of the Eisenberg correlation.<sup>19</sup> Based on the data shown in Figure 8, it can be concluded that the experimental correlation is not significantly different than the Eisenberg correlation.

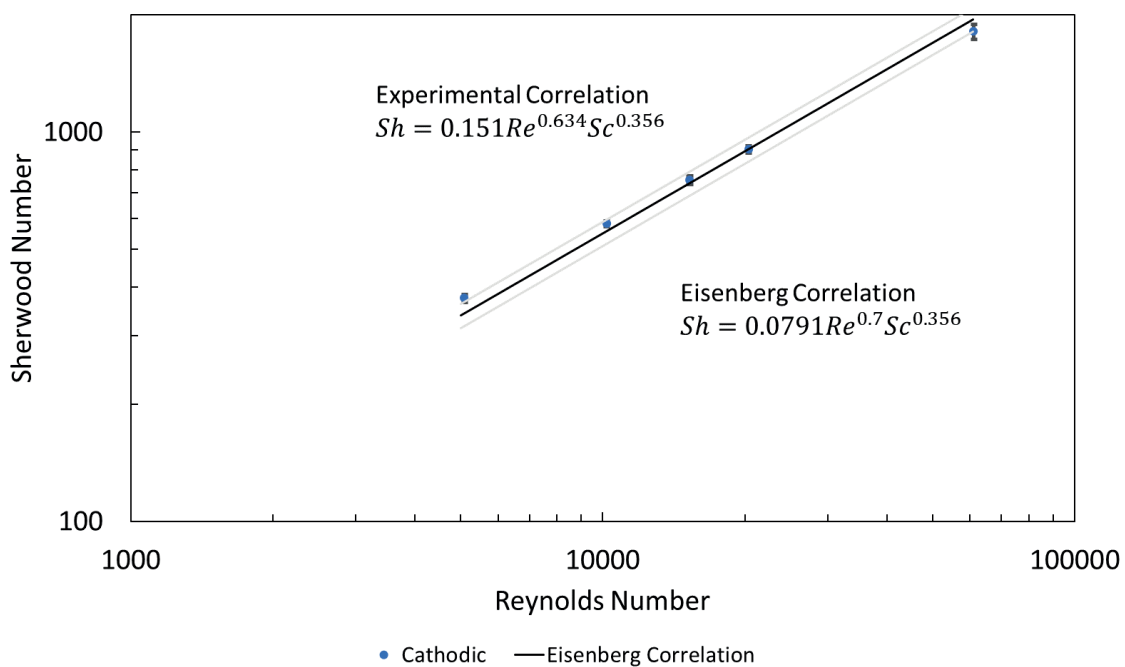


Figure 8. Sherwood Correlation Resulting from Mass Transfer Experiments Compared to Correlation from the Eisenberg Paper<sup>19</sup>

### 5.1.2 Corrosion Experiments

Similar to the mass transfer experiments above, the RCE corrosion experiments were performed in accordance with the Procedure section above. As described, these tests

were performed at 500 RPM, 1000 RPM, 1500 RPM, and 2000 RPM. The experiments were also performed at pH  $4.0\pm 0.1$ ,  $5.0\pm 0.1$ , and  $6.0\pm 0.1$  as well as in both CO<sub>2</sub> and N<sub>2</sub> sparged environments. At each rotational speed, two runs are shown. At each rotational speed, the runs were determined to be repeatable if the limiting current region appeared to be in an identical location upon visual inspection. Also included on these potentiodynamic sweeps are the plotted corrosion current and corrosion potential points, as determined using the LPR experimentation. For all tables, both repeatable runs were averaged to obtain the tabulated results.

The results for the potentiodynamic sweeps performed in a CO<sub>2</sub> sparged environment at pH  $4.0\pm 0.1$  are shown in Figure 9, Table 7, and Table 8, below. As shown, there was a clear increase in the cathodic limiting current as the rotational speed was increased. It was also shown in the experimental results that there is an increasing corrosion rate with increasing rotational speed, which indicates that the corrosion rate is controlled by the limiting current. This follows the same trend as observed when the parameters are modeled using ICMT's FREECORP™ software.<sup>21</sup> For all FREECORP™ simulations, an equivalent pipe diameter of 10.1 cm was utilized. All RCE experimental rotational speeds were converted to this equivalent pipe flow by a mass transfer correlation using Equation (2), similar to the mass transfer experimentation above. As the experimental corrosion rates were within 20% of their respective FREECORP™ corrosion rates and the same trend was visible, it can be concluded that these experimental results validate the FREECORP™ software<sup>21</sup> in these conditions.

The corrosion rates calculated by FREECORP™ were relatively similar to experimental results, as shown in Table 8, Table 10, Table 12, and Table 14 below. The experimental results were determined by analyzing the potentiodynamic sweep data and determining the Tafel Slope, which is the slope of the line that runs through the corrosion current and corrosion potential point on the graph and also intersects the anodic or cathodic potentiodynamic sweep data as a tangent line. These Tafel Slope values were recorded and utilized in Equations (20), (21), and (22), in order to calculate the corrosion rate for the experimental data.

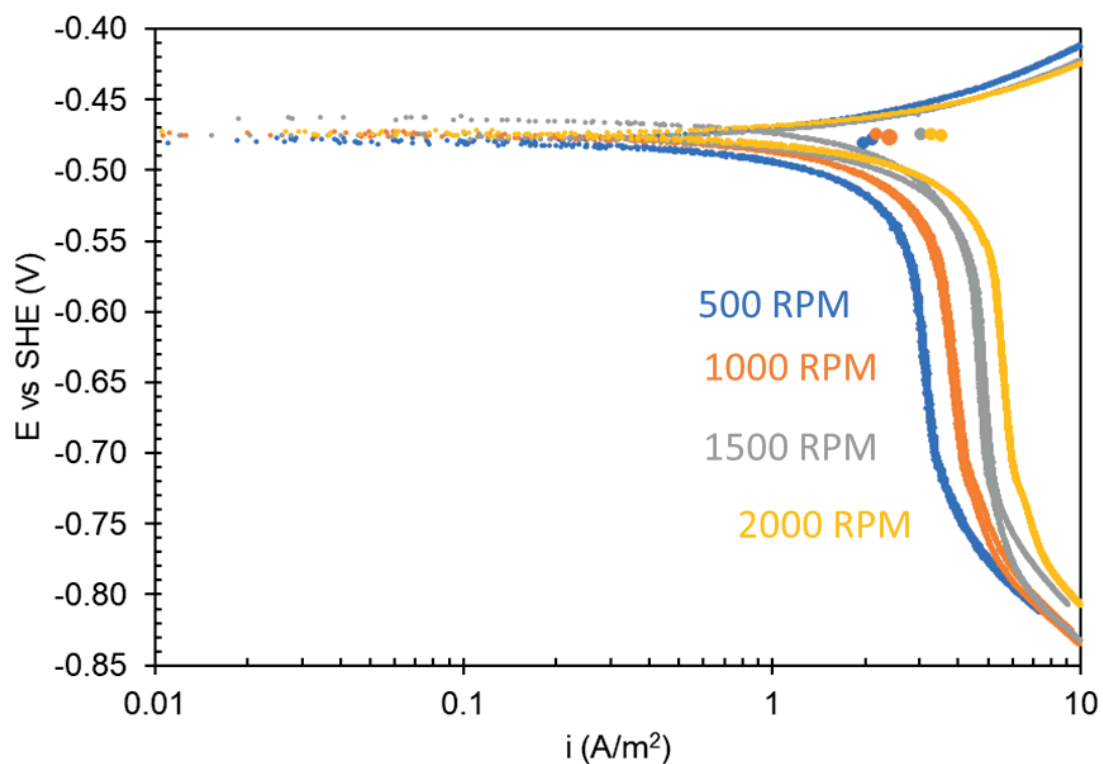


Figure 9. Potentiodynamic sweep data showing the effect of rotational rate on 1018 mild steel RCE corrosion in  $CO_2$  sparged,  $pH\ 4.0\pm 0.1$ , and 1 wt% NaCl electrolyte solution at  $35^\circ C$  in for 500 RPM, 1000 RPM, 1500 RPM, and 2000 RPM RCE rotational rates.

Table 7. Linear Polarization Resistance Data for RCE corrosion experiments in CO<sub>2</sub> sparged environment at pH 4.0±0.1

Rotational Speed (RPM)	pH	Corrosion Rate (mm/year)	R <sub>p</sub> (Ω)	i <sub>corr</sub> (A/m <sup>2</sup> )	E <sub>corr</sub> (V)
500	4.02±0.01	2.42±0.09	21.15±0.88	2.28±0.10	-0.479±0.001
1000	4.02±0.00	2.70±0.12	18.64±0.91	2.59±0.13	-0.476±0.001
1500	3.99±0.01	3.54±0.02	13.86±0.10	3.48±0.03	-0.468±0.007
2000	4.04±0.00	4.01±0.14	11.86±0.50	4.07±0.17	-0.475±0.001

Table 8. Comparison of LPR corrosion rate to FREECORP™ in CO<sub>2</sub> sparged environment at pH 4.0±0.1 through 10.1 cm diameter pipe

Rotational Speed (RPM)	10.1 cm Diameter Pipe Flow Velocity (m/s)	Experimental Corrosion Rate (mm/year)	FREECORP™ Corrosion Rate (mm/year)
500	0.68	2.68±0.11	2.96
1000	1.19	3.05±0.15	3.52
1500	1.64	4.09±0.03	3.84
2000	2.06	4.78±0.20	4.07

The results for the potentiodynamic sweeps performed in a CO<sub>2</sub> sparged environment at pH 5.0±0.1 are shown in Figure 10, Table 9, and Table 10, below. As

shown, there was a slight increase in the cathodic limiting current as the rotational speed was increased. For these conditions, the experimental results, which also show a very small increase in corrosion rate with increasing rotational speed, indicate that the corrosion rate is likely controlled by the limiting current. FREECORP™ corrosion rates follow a similar trend as compared to the experimental results and experimental corrosion rates were found to be within 10% of their respective FREECORP™ corrosion rates. This indicates that the experimental results validated the model used in FREECORP™.

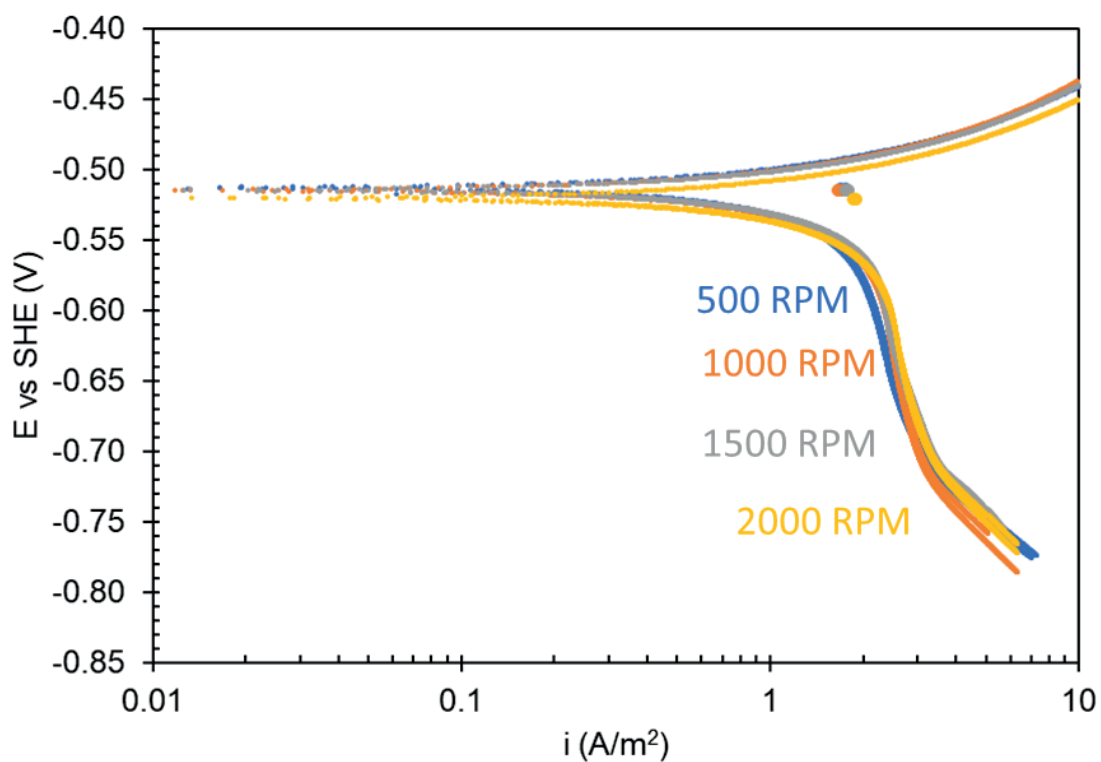


Figure 10. Potentiodynamic sweep data showing the effect of rotational rate on 1018 mild steel RCE corrosion in CO<sub>2</sub> sparged, pH 5.0±0.1, and 1 wt% NaCl electrolyte solution at 35°C in for 500 RPM, 1000 RPM, 1500 RPM, and 2000 RPM RCE rotational rates.

Table 9. Linear Polarization Resistance Data for RCE corrosion experiments in CO<sub>2</sub> sparged environment at pH 5.0±0.1

Rotational Speed (RPM)	pH	Corrosion Rate (mm/year)	R <sub>p</sub> (Ω)	i <sub>corr</sub> (A/m <sup>2</sup> )	E <sub>corr</sub> (V)
500	5.01±0.00	2.03±0.03	24.57±0.37	1.26±0.05	-0.514±0.000
1000	4.99±0.00	1.98±0.03	24.09±0.17	1.24±0.04	-0.515±0.000
1500	5.03±0.00	2.08±0.02	23.62±0.36	1.28±0.04	-0.515±0.000
2000	5.02±0.00	2.20±0.02	22.13±0.59	1.36±0.05	-0.521±0.000

Table 10. Comparison of LPR corrosion rate to FREECORP™ in CO<sub>2</sub> sparged environment at pH 5.0±0.1 through 10.1 cm diameter pipe

Rotational Speed (RPM)	10.1 cm Diameter Pipe Flow Velocity (m/s)	Experimental Corrosion Rate (mm/year)	FREECORP™ Corrosion Rate (mm/year)
500	0.66	1.43±0.05	1.46
1000	1.15	1.41±0.04	1.53
1500	1.58	1.46±0.04	1.58
2000	1.99	1.55±0.06	1.61

The results for the potentiodynamic sweeps performed in a CO<sub>2</sub> sparged environment at pH 6.0±0.1 are shown in Figure 11, Table 11, and Table 12 below. As

shown, there was almost no change in the cathodic limiting current as the rotational speed was increased. This is further validated by the experimental results, which show a negligible increase in corrosion rate with increasing rotational speed. FREECORP™ corrosion rates follow a similar trend as compared to the experimental results. Similar to above, the experimental corrosion rates were within 20% of their respective FREECORP™ corrosion rates, which validates the model used in the FREECORP™ software.<sup>21</sup>

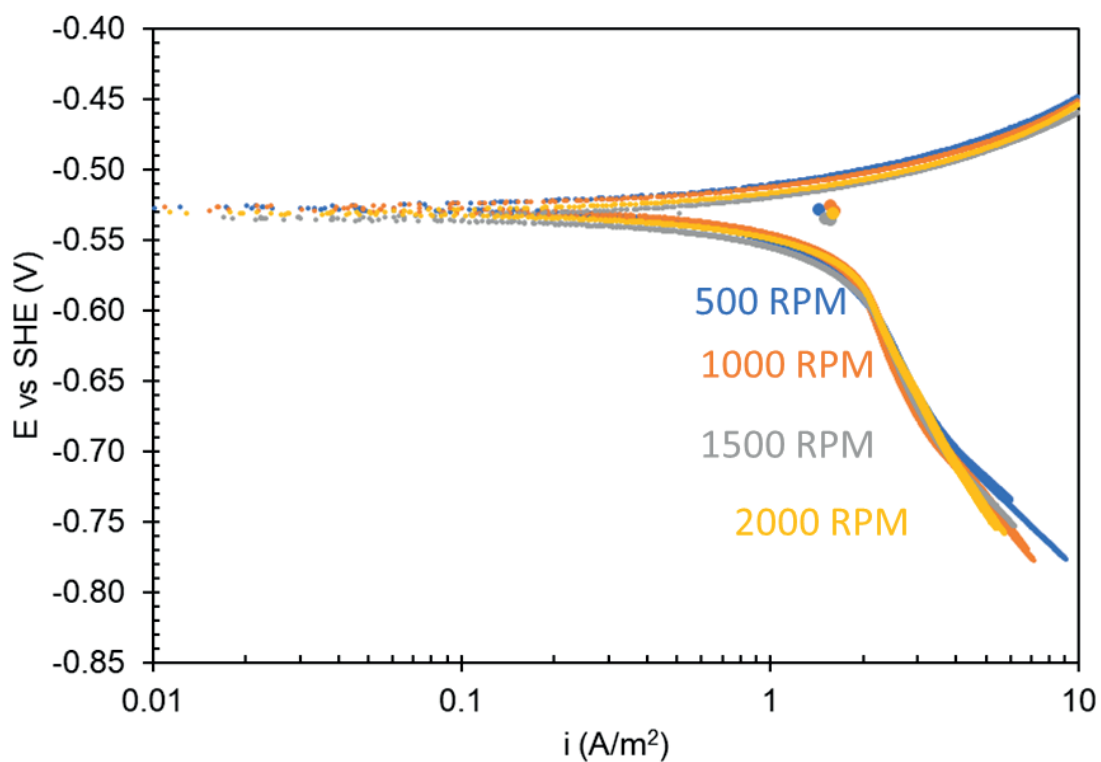


Figure 11. Potentiodynamic sweep data showing the effect of rotational rate on 1018 mild steel RCE corrosion in CO<sub>2</sub> sparged, pH 6.0±0.1, and 1 wt% NaCl electrolyte solution at 35°C in for 500 RPM, 1000 RPM, 1500 RPM, and 2000 RPM RCE rotational rates.

Table 11. Linear Polarization Resistance Data for RCE corrosion experiments in CO<sub>2</sub> sparged environment at pH 6.0±0.1

Rotational Speed (RPM)	pH	Corrosion Rate (mm/year)	R <sub>p</sub> (Ω)	i <sub>corr</sub> (A/m <sup>2</sup> )	E <sub>corr</sub> (V)
500	6.03±0.00	1.71±0.01	29.76±0.20	0.89±0.00	-0.528±0.001
1000	5.99±0.00	1.87±0.03	26.73±0.52	1.03±0.06	-0.528±0.002
1500	5.99±0.00	1.82±0.04	27.68±0.64	0.96±0.04	-0.535±0.000
2000	6.00±0.00	1.89±0.00	26.56±0.02	1.03±0.01	-0.531±0.000

Table 12. Comparison of LPR corrosion rate to FREECORP™ in CO<sub>2</sub> sparged environment at pH 6.0±0.1 through 10.1 cm diameter pipe

Rotational Speed (RPM)	10.1 cm Diameter Pipe Flow Velocity (m/s)	Experimental Corrosion Rate (mm/year)	FREECORP™ Corrosion Rate (mm/year)
500	0.66	1.05±0.00	1.31
1000	1.15	1.21±0.07	1.31
1500	1.60	1.13±0.04	1.32
2000	2.01	1.21±0.01	1.32

Potentiodynamic sweeps were then compared for each of the three pH values evaluated, as shown in Figure 12 below. As shown, there is a significant difference in the

sweeps as the pH is increased. The corrosion rate decreases as pH increases. This is because the  $H^+$  concentration in solution is decreasing with increasing pH. The reduction of  $H^+$  is the primary cathodic reaction within this electrochemical system. Thus, the observed corrosion rate is lower because there is less reactant present in solution compared to experiments at a lower pH.

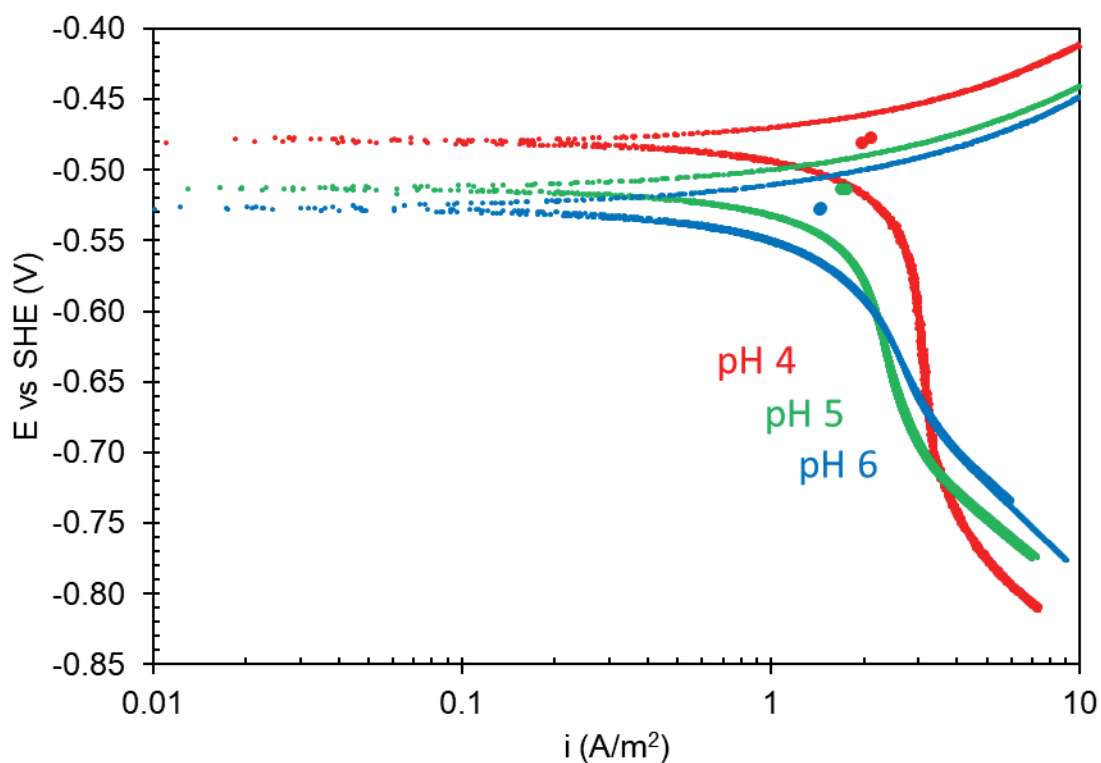


Figure 12. Potentiodynamic sweep data showing the effect of pH on 1018 mild steel RCE corrosion in  $CO_2$  sparged and 1 wt% NaCl electrolyte solution at  $35^\circ C$  for pH  $4.0 \pm 0.1$ ,  $5.0 \pm 0.1$ , and  $6.0 \pm 0.1$  at 500 RPM rotational rate.

The results for the potentiodynamic sweeps performed in a N<sub>2</sub> sparged environment at pH 5.0±0.1 are shown in Figure 13, Table 13, and Table 14, below. It should be noted that corrosion experimentation in an N<sub>2</sub> sparged environment were only performed at pH 5.0±0.1. As shown, there was not a clear cathodic limiting current region. Additionally, the experimental corrosion results show a very small increase in corrosion rate with increasing rotational speed. This is due to the fact that there are far fewer H<sup>+</sup> ions in solution when compared to experiments performed at a lower pH, such as the pH 4 experiments performed in the CO<sub>2</sub> sparged environment. FREECORP™ corrosion rates follow a similar trend as compared to the experimental results. Similar to above the FREECORP™ model was validated by these corrosion experiments because the experimental corrosion rates were within 20% of their corresponding FREECORP™ corrosion rates.

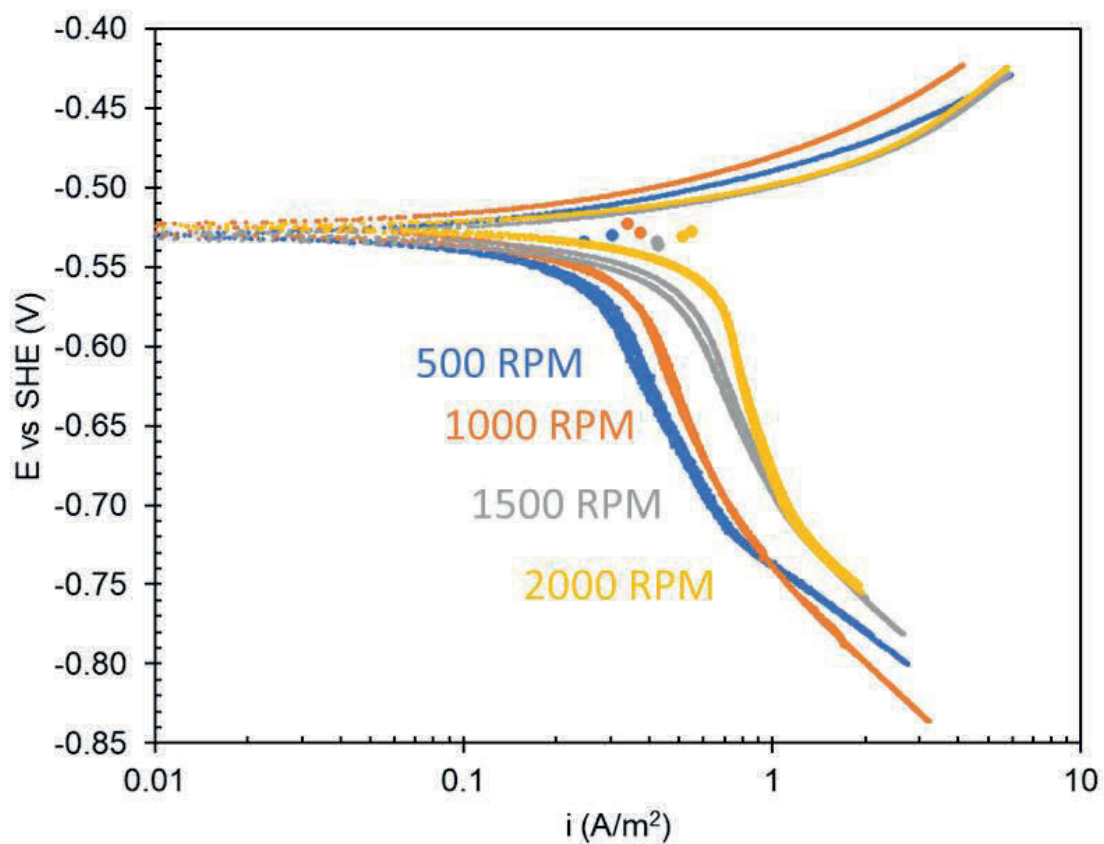


Figure 13. Potentiodynamic sweep data showing the effect of rotational rate on 1018 mild steel RCE corrosion in  $N_2$  sparged,  $pH\ 5.0\pm 0.1$ , and 1 wt% NaCl electrolyte solution at  $35^\circ C$  in for 500 RPM, 1000 RPM, 1500 RPM, and 2000 RPM RCE rotational rates.

Table 13. Linear Polarization Resistance Data for RCE corrosion experiments in N<sub>2</sub> sparged environment at pH 5.0±0.1

Rotational Speed (RPM)	pH	Corrosion Rate (mm/year)	R <sub>P</sub> (Ω)	i <sub>corr</sub> (A/m <sup>2</sup> )	E <sub>corr</sub> (V)
500	4.92±0.03	0.32±0.03	177.23±18.88	0.28±0.03	-0.533±0.002
1000	4.98±0.01	0.42±0.02	131.52±4.55	0.37±0.01	-0.526±0.003
1500	4.91±0.02	0.50±0.00	110.89±0.78	0.44±0.00	-0.535±0.001
2000	4.90±0.02	0.62±0.02	88.41±3.37	0.56±0.02	-0.530±0.002

Table 14. Comparison of LPR corrosion rate to FREECORP™ in N<sub>2</sub> sparged environment at pH 5.0±0.1 through 10.1 cm diameter pipe

Rotational Speed (RPM)	10.1 cm Diameter Pipe Flow Velocity (m/s)	Experimental Corrosion Rate (mm/year)	FREECORP™ Corrosion Rate (mm/year)
500	0.66	0.32±0.03	0.27
1000	1.15	0.42±0.02	0.36
1500	1.58	0.50±0.00	0.42
2000	1.99	0.63±0.02	0.46

The effect of the sparge gas can be analyzed by plotting the potentiodynamic sweeps resulting from each sparge gas environment, as shown in Figure 14 below. The

corrosion rate is significantly lower in the N<sub>2</sub> sparged environment, compared to the CO<sub>2</sub> sparged environment. This is caused by the water chemistry as discussed in the Background on Corrosion section; as the CO<sub>2</sub> dissolves in solution, it influences and increases the corrosion rate.<sup>4</sup> This is caused by carbonic acid within solution dissociating and causing a buffering effect.

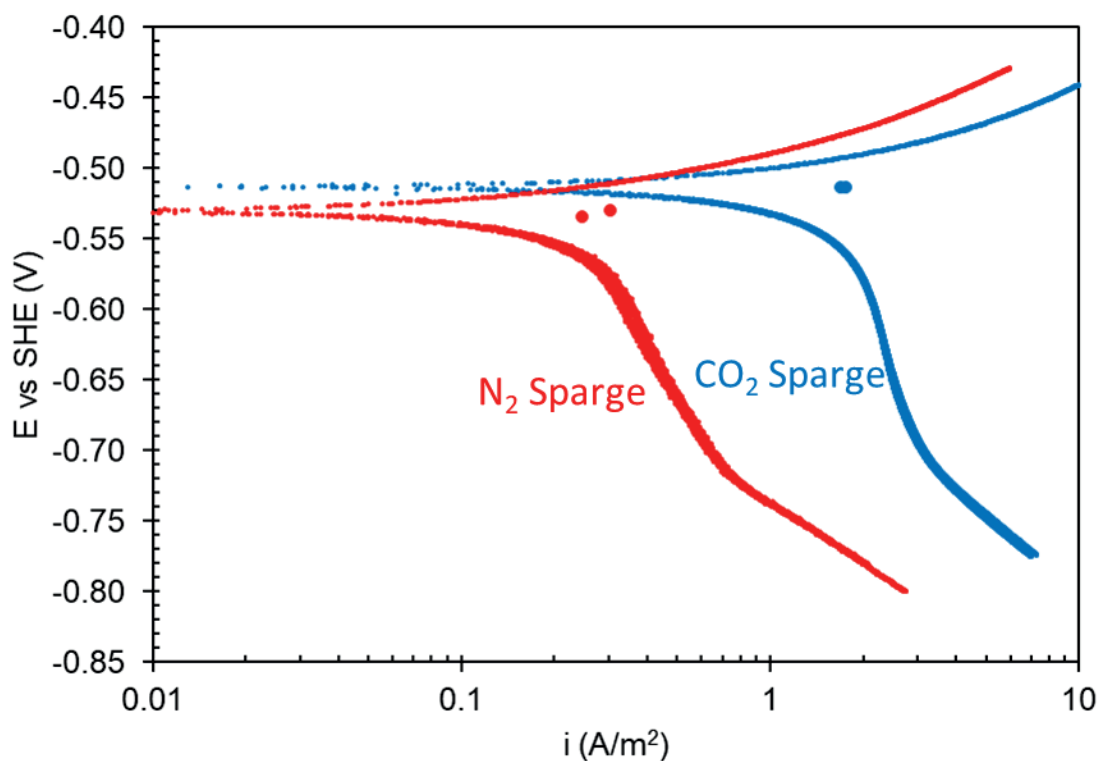


Figure 14. Potentiodynamic sweep data showing the effect of N<sub>2</sub> or CO<sub>2</sub> sparge gas on 1018 mild steel RCE corrosion in pH 5.0±0.1 and 1 wt% NaCl electrolyte solution at 35°C at 500 RPM rotational rate.

## 5.2 Preliminary RDE Experiments

Similar to the RCE corrosion experiments above, the RDE corrosion experiments primarily resulted in potentiodynamic sweep data was collected utilizing the potentiostat, as described in the RDE experimental Procedure section of this thesis, and results are displayed below in Figure 15, Table 15, and Table 16. As described, these tests were performed at 250 RPM, 500 RPM, 1000 RPM, 2000 RPM, 4000 RPM, and 8000 RPM. The experiments were performed at  $\text{pH } 4.0 \pm 0.1$ , in a  $\text{CO}_2$  sparged environment. At each rotational speed, two runs are shown. At each rotational speed, the runs were determined to be repeatable if the limiting current regions from each individual run appeared to be indistinguishable from one another upon visual inspection when plotted together. For all tables, both repeatable runs were averaged to obtain the tabulated results.

As shown, there was a clear increase in limiting current and corrosion rate as the rotational speed was increased. The mass transfer coefficients calculated from this data can be compared to CFD models generated in Ansys Fluent<sup>22</sup> in order to understand the validity of those models. Similar to the RCE experiments above, Table 16 shows that the corrosion rates for RDE experiments follow the same trend as seen when the parameters are modeled using FREECORP™. As with the RCE experiments, the rotational speed of the RDE can be converted to an equivalent pipe flow through a 10.1 cm diameter pipe using Equation (17). Then Equations (20), (21), and (22) were utilized in order to calculate the corrosion rate for the experimental data after the Tafel slopes were determined for each experimental run. Through this analysis, it was determined that the

experimental corrosion rates were all within 20% of their corresponding FREECORP™ corrosion rates. This validates the model used within the FREECORP™ software.<sup>21</sup>

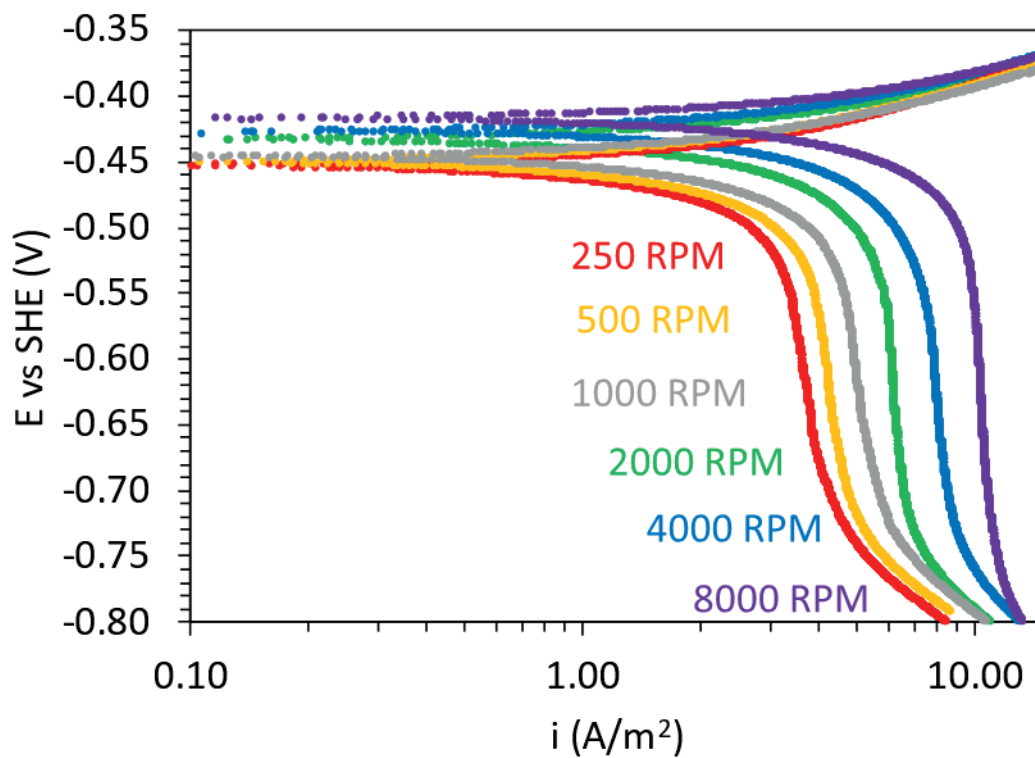


Figure 15. Potentiodynamic sweep data showing the effect of rotational rate on X65 mild steel RDE corrosion in CO<sub>2</sub> sparged, pH 4.0±0.1, and 1 wt% NaCl electrolyte solution at 30°C in for 250 RPM, 500 RPM, 1000 RPM, 2000 RPM, 4000 RPM, and 8000 RPM RDE rotational rates.

Table 15. Linear Polarization Resistance Data for RDE corrosion experiments in CO<sub>2</sub> sparged environment at pH 4.0±0.1

Rotational Speed (RPM)	pH	Corrosion Rate (mm/year)	R <sub>P</sub> (Ω)	i <sub>corr</sub> (A/m <sup>2</sup> )	E <sub>corr</sub> (V)
250	3.99±0.01	2.871±0.12	477.24±22.69	2.83±0.13	-0.480±0.001
500	4.05±0.00	3.030±0.04	446.00±6.48	3.02±0.04	-0.476±0.001
1000	3.93±0.00	3.550±0.09	382.69±11.42	3.52±0.01	-0.471±0.001
2000	3.93±0.01	4.565±0.08	291.38±5.71	3.04±0.02	-0.461±0.001
4000	3.96±0.02	5.636±0.18	225.62±8.57	4.25±0.19	-0.452±0.001
8000	3.98±0.01	6.696±0.22	179.90±8.01	4.97±0.41	-0.445±0.001

Table 16. Comparison of LPR corrosion rate to FREECORP™ in CO<sub>2</sub> sparged environment at pH 4.0±0.1 through 10.1 cm diameter pipe

Rotational Speed (RPM)	10.1 cm Diameter Pipe Flow Velocity (m/s)	Experimental Corrosion Rate (mm/year)	FREECORP™ Corrosion Rate (mm/year)
250	0.87	2.76±0.13	2.42
500	1.31	2.94±0.04	2.76
1000	1.96	3.43±0.01	3.13
2000	2.93	2.96±0.02	3.50
4000	4.38	4.13±0.18	3.85
8000	6.55	4.83±0.40	4.82

### 5.3 Experimental Summary

Throughout the course of this research, experimental data was collected for the mass transfer of ferricyanide/ferrocyanide, baseline corrosion experimentation using 1018 mild steel RCE specimens, and baseline corrosion experimentation using an X65 mild steel RDE specimen. The primary goal of these experiments was to validate known models. In the case of the mass transfer testing, the goal was to validate the mass transfer correlation proposed the Eisenberg Paper.<sup>19</sup> In the case of the corrosion experiments, the purpose was to validate the models utilized in the FREECORP™ software developed at the ICMT.<sup>21</sup> All experimentally determined values were within the error tolerance, as discussed in the experiment's individual section. As such, it can be concluded that all

physical experimentation successfully validated the theoretical models to which they were compared. This data can be utilized in future work to validate other models, such as CFD simulations. Once CFD models are created for the experimental systems discussed within this document, the results contained may be used to verify whether the CFD model is able to accurately model corrosion in the simulated environment.

## **Chapter 6: Methodology for Modeling Flowtube Using CFD**

### **6.1 Simplified Preliminary Model and Introduction to CFD Modeling**

#### ***6.1.1 Rationale for CFD Modeling***

In order to simulate the movement of fluids within and around the flowtube, computational fluid dynamics (CFD) is utilized. Computational Fluid Dynamics software, like the Ansys Fluent software<sup>22</sup> used for this analysis, operates by solving a series of equations at various locations throughout a model. These equations are detailed in Appendix B: Equations within the Ansys Fluent Background section. Ansys Fluent solves the equations (or a subset of them as necessary) at every discretized point within the system and reports residuals. These residuals are determined by taking all the variables to one side of each equation at every discretized point within the system and determining the difference. A perfect solution would be a case where all the residuals are equal to zero.<sup>18</sup> Within Ansys Fluent, the experimental parameters, such as mesh size, turbulence models, or time step, are manipulated until every residual is equal to or less than  $10^{-3}$ . Once that threshold is met, the system is considered to have converged. The results at this point are what have been reported as the solution.

These simulations were performed using the CFD approach due to the versatility of the CFD simulation software and the relative simplicity of changing parameters in a CFD simulation compared to changing parameters in a physical model. CFD simulations allow for complex geometries, such as the flowtube, to be modeled in a virtual space. By simulating fluid flow within the CFD software, design considerations can be explored without the need to fabricate expensive physical prototypes. CFD simulations also have

the ability to simulate mass transfer and corrosion, which are especially useful for the topic of this thesis. The results of the following CFD simulations will primarily serve to validate that the Ansys Fluent software<sup>22</sup> can accurately model the observed fluid dynamics from the physical prototype flowtube. These results can then be expanded upon to create predictions for how design changes may affect pertinent metrics within future prototype versions.

### ***6.1.2 Translation to SpaceClaim***

Before the flowtube can be modeled in CFD, a structural model of the components must be created. For the purposes of this simulation, Ansys SpaceClaim was used to create a computer aided design (CAD) drawing of the specimen holder and impeller. This CAD drawing is known as the “geometry” used in the CFD simulation. It should be noted that the geometry created for the flowtube specimen holder is simplified and therefore will differ from the schematic shown above as well as the first prototype that was created. First, the entire specimen holder was modeled as one solid piece. This ignores any imperfections caused by the interfaces between the electrochemical specimens and reference electrodes. Additionally, the specimen holder is free floating within the glass cell in this example, which ignores the impact of any support structures that exist to hold the flowtube to the lid of the glass cell. Furthermore, the impeller is located directly above the specimen holder in the model. This ignores the impact of the flow straighteners and counter electrode holder, which will exist in the final flowtube design. This also means that the central counter electrode will be free floating within the glass cell for this simulation, separate from the specimen holder. Lastly, the beveled edge

on the inner diameter of the bottom of the specimen holder and the bullnose edge on the bottom of the central counter electrode were ignored in order to make the entire geometry a simple annulus flow. A visual representation of the geometry created is shown below in Figure 16 and Figure 17.

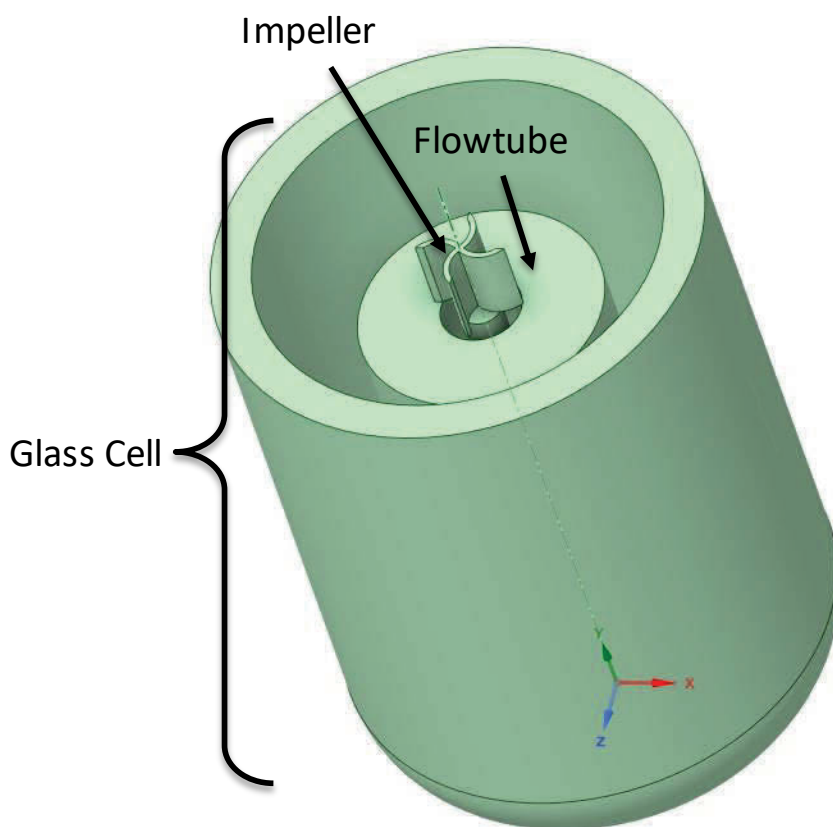


Figure 16. CAD drawing of simplified flowtube in a glass cell

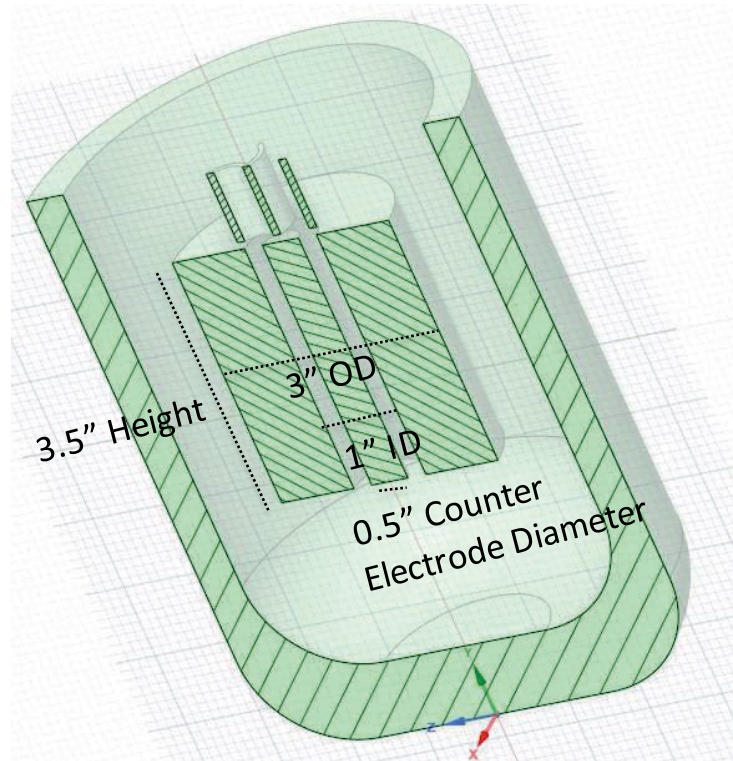


Figure 17. Cross-section view of CAD drawing of simplified flowtube in a glass cell

Once the geometry of the physical specimen holder, impeller, and glass cell were created, the volume enclosed by the glass cell was “filled” with a modeled fluid to allow modeling of the moving fluid within the system. In addition to the main fluid body within the glass cell, a separate fluid body was created around the impeller itself. This smaller body, known as an enclosure, allows for rotational motion to be set in only a small volume, where it can then affect the bulk fluid body around it. This so-called volume extraction can be visualized using Figure 18 and Figure 19 below.

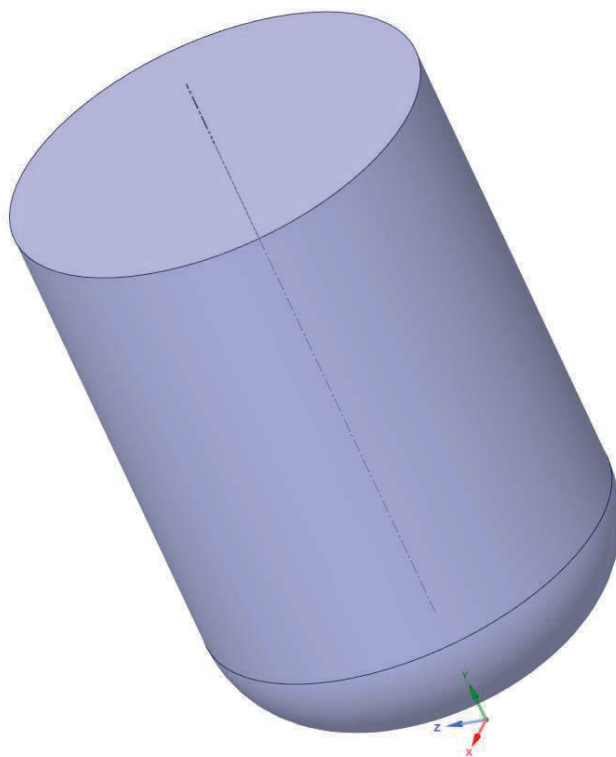


Figure 18. External view of volume enclosed by glass cell

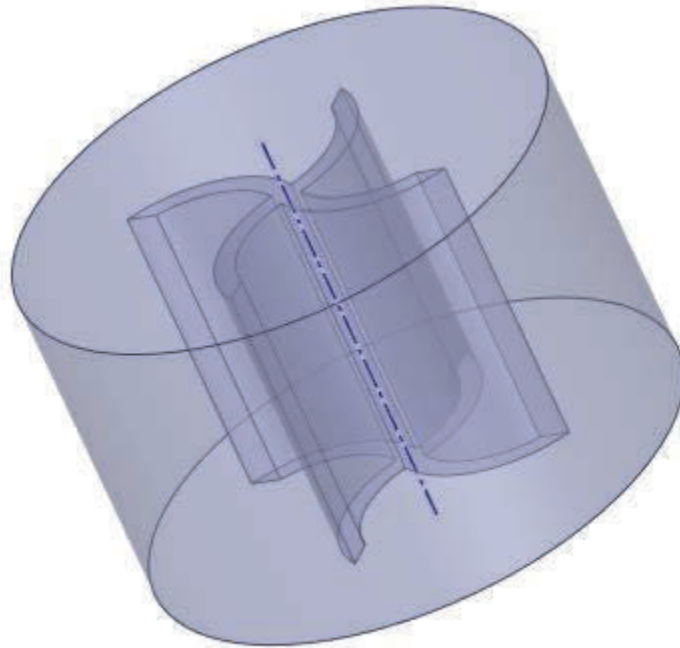


Figure 19. Enclosure volume surrounding impeller

It should be noted that once the fluid volumes were created, all physical components were suppressed within the model. This is because the solid components are irrelevant to this model. There is no expected interaction between the fluid and solid components beyond simple wall interface interactions.

### **6.1.3 Meshing**

After the volume was created, the system was meshed. Meshing is performed to discretize the spatial parameters of the specified geometry. As mentioned earlier, these discretized points are the locations at which the equations discussed within the Ansys Fluent Background section are solved. Much flexibility exists on how this mesh can be

created and the resolution of the mesh created. The resolution of the mesh is limited by the computer being used to run the simulations, as a finer mesh will result in more calculations to be performed per iteration. By removing the solid components earlier, a finer mesh was created within the fluid volume because no mesh was needed within the solid components. For the purposes of this preliminary model, a uniform mesh with element size of 2.5 mm was created. This mesh contained 486,182 nodes. This mesh can be visualized in Figure 20 and Figure 21 below. For subsequent simulations, the bulk mesh was increased to 3 mm element sizing and an inflation was added within the specimen holder and around the impeller. The mesh sizing around those regions of interest was decreased to 1 mm. This was determined to be beneficial because the finer mesh around the regions of interest allowed for more accurate calculations to be performed close to the specimen surface as well as nearest the moving impeller. Increasing the bulk fluid mesh sizing outside of these regions of interest did not have any significant impact on the superficial fluid velocity, turbulent kinetic energy, or  $y^+$  values observed within the regions of interest. As a result, it was determined that the larger mesh sizing within the bulk solution was acceptable for the model. It is desired to have a larger mesh sizing where possible so that computational resources are not devoted to performing calculations on nodes that do not impact the regions of interest.

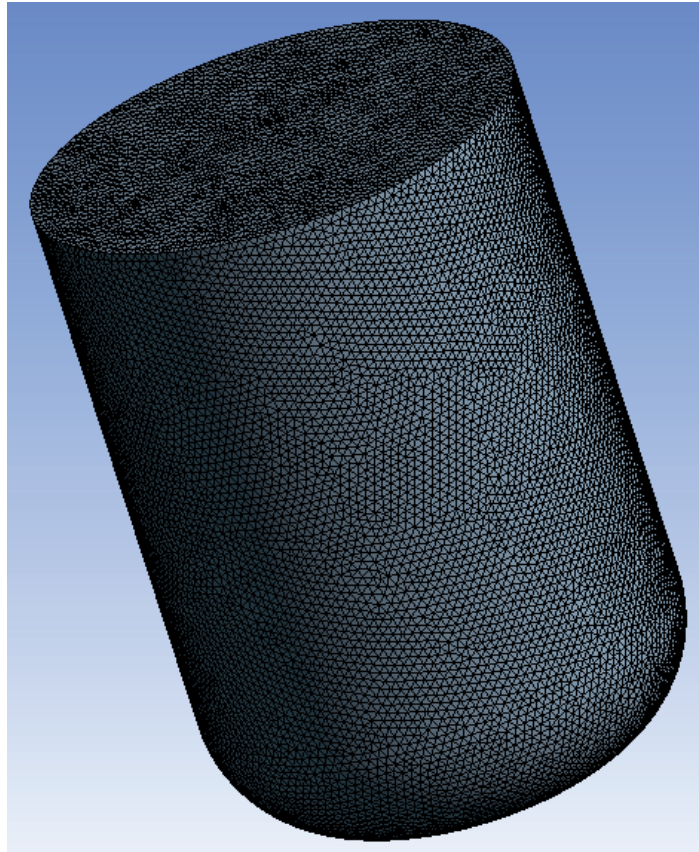


Figure 20. External view of mesh on volume enclosed by the glass cell

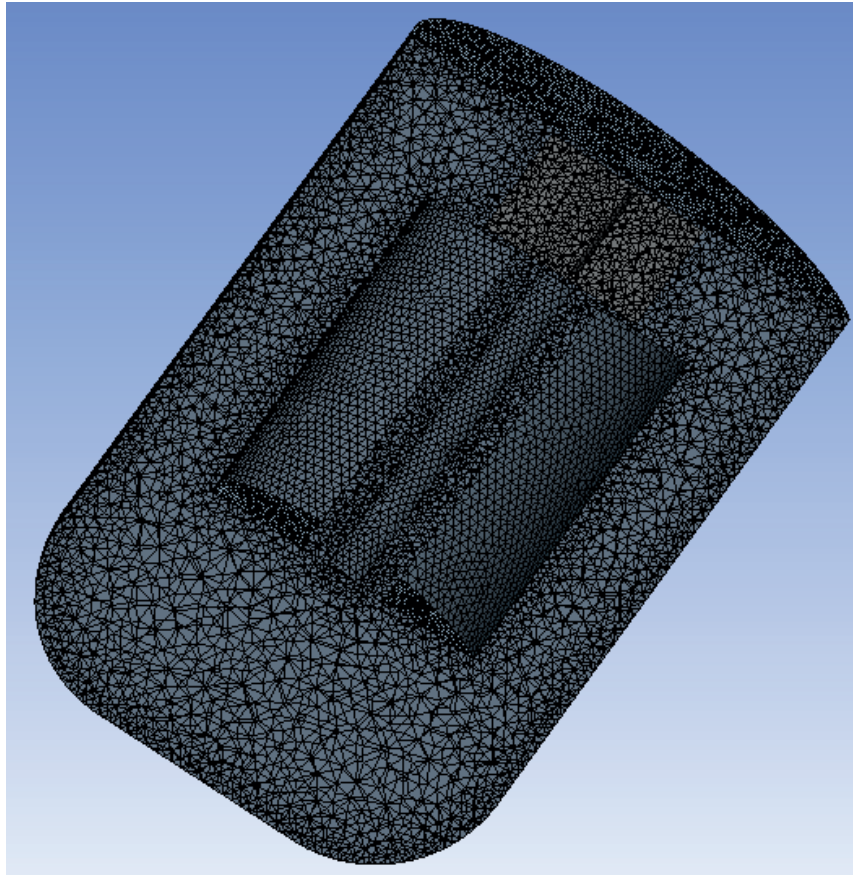


Figure 21. Cross-section view of mesh on volume enclosed by the glass cell

Within the meshing software, named selections were created for the bulk fluid, fluid within the enclosure surrounding the impeller, and the bottom plate of the glass cell. This will allow for specific boundary conditions or initial conditions to be implemented later in the CFD simulation.

#### **6.1.4 Ansys Fluent CFD Modelling**

After meshing was complete, the meshed geometry was imported into Ansys Fluent for use in CFD modeling. For these simulations, the standard k- $\epsilon$  model with a standard wall function was used to model viscous flow near the solid boundaries.

Similarly, the species transport model was used for modeling the salt mixture. According to the online theory guide for Ansys Fluent, “ANSYS FLUENT can model the mixing and transport of chemical species by solving conservation equations describing convection, diffusion, and reaction sources for each component species.”<sup>17</sup> The boundary condition was set to a constant concentration of 0.01 mass fraction salt, which will cause the entire system to eventually reach an equilibrium of 0.01 mass fraction salt. This is desired because the real simulation will achieve a similar salt concentration for electrochemical experimentation. It should be noted that salt does not exist within Ansys Fluent as a chemical. As such, a custom chemical was created to stand in place of salt. This custom chemical was created using the chemical properties of water as its foundation, and the molecular weight of the custom chemical was changed to that of NaCl, 58.44 g/mol, in order to allow Ansys Fluent to recognize the new chemical as different from water. This was the only change made to the new species when compared to water. After the custom chemical was created, the boundary condition was set for the bottom of the glass cell as a source for this chemical. It should be noted that this mass transport simulation exists as a proof of concept. In the future, mass transfer considerations at the surface of the electrochemical specimens will be modeled; mass transfer is the link between fluid flow and corrosion.

After this, frame motion was used to model the rotating motion of the impeller. The impeller was set to have rotational frame motion about the y-axis at a rotational rate of 5000 RPM for the transient experiments and 1000 RPM, 2000 RPM, and 5000 RPM for the steady state experiments. It should be noted that all the rotational speeds are

negative due to the orientation of the impeller in this model in order to induce the desired flow pattern. A gravitational acceleration of  $-9.81 \text{ m/s}^2$  in the y direction was also added for a more realistic simulation. All other conditions within the cell were left at default values, such as the no slip wall condition.

## **6.2 Replication of Physical Prototype Model**

For this trial, the flowtube was modeled more closely to the physical prototype. Unlike the preliminary trial, the beveled edge was added to the bottom of the specimen holder, the bullnose edge was added to the bottom of the counter electrode, the counter electrode holder was added inside the flowtube, the impeller design was created more accurately to the physical prototype, external baffles were added outside the flowtube, and an internal flow straightener was added above the sample holder. Additionally, the glass cell housing the flowtube was expanded to reflect the 4 L design used in experimentation, rather than the 2 L glass cell used in the previous model. The functional reason for this is to exceed the minimum electrolyte volume to specimen surface area ratio of  $40 \text{ mL/cm}^2$  noted in ASTM standard G31 Section 8.9.2.<sup>20</sup>

The internal flow straightener was originally intended to reduce/eliminate swirling motion inside the specimen holder. This flow straightener was located directly above the central counter electrode and directly below the impeller. Sketches of the prototype flowtube seem to indicate that the original intention was to implement the internal flow straightener at the bottom of the specimen holder as well, but this was never implemented. A close-up view of the internal flow straightener used within the geometry is shown in Figure 24. In addition to the internal flow straightener, external flow

straightening baffles were added to the physical flowtube prototype at a later point in order to eliminate swirling secondary motion observed within the glass cell when the flowtube was in operation. The entire flowtube geometry, as viewed externally, is shown in Figure 22. A cross-section of the entire flowtube geometry is shown in Figure 23 below.

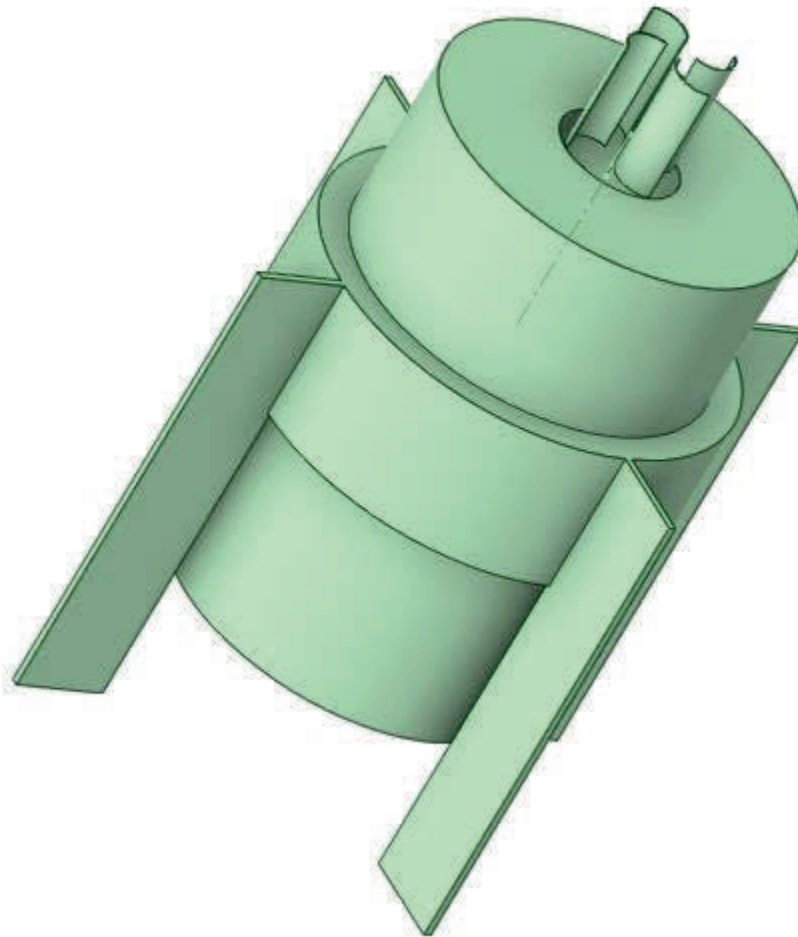


Figure 22. External view of flowtube geometry with external baffles

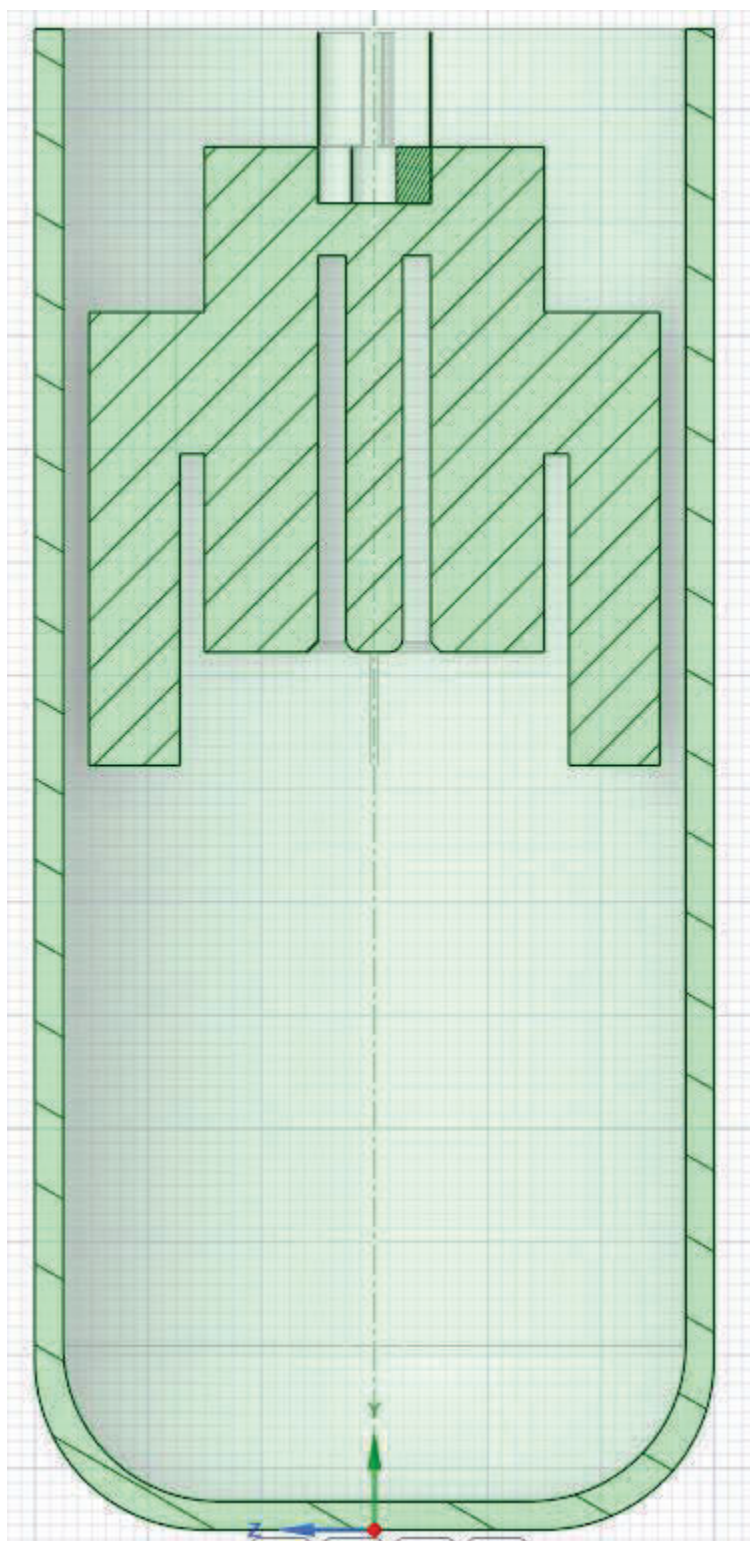


Figure 23. Cross-section view of flowtube with internal flow straightener and external baffles in the 4 L glass cell

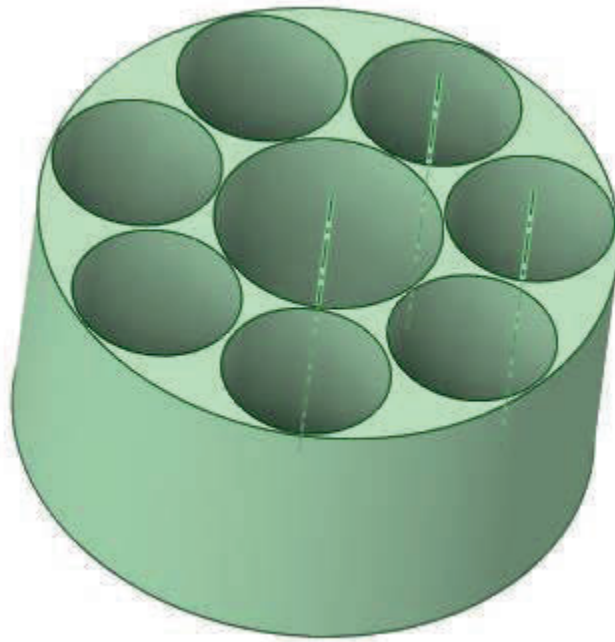


Figure 24. Internal flow straightener geometry used in CFD simulations

Similar to the preliminary trial, a new mesh was created for this geometry. For this geometry, 3 mm mesh sizing was used for the bulk solution, 1 mm mesh sizing was used for the wall of the specimen holder with 1.2 growth rate, 1 mm mesh sizing was used for the top of the flowtube with 1.2 growth rate, and 2 mm mesh was used for the impeller enclosure fluid body. These settings created 183,455 nodes and 946,844 elements in the mesh. The inflations were implemented in order to address the  $y^+$  value issues noted in the previous simulations. The mesh can be seen in Figure 25 below.

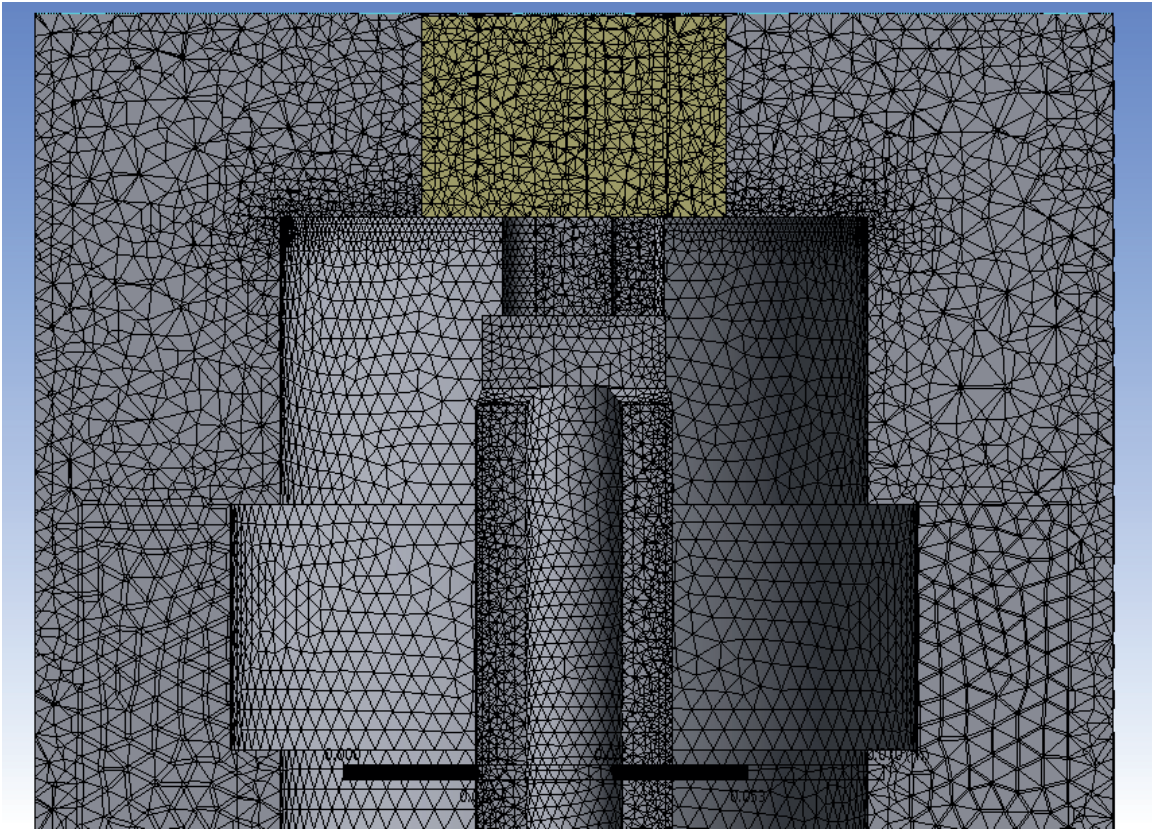


Figure 25. Cross-section of refined mesh used for CFD simulation in 4 L glass cell with baffles and internal flow straightener

### 6.3 Removal of Internal Flow Straightener

In order to facilitate future design considerations, CFD modeling can be utilized in order to determine the anticipated effects of design changes on fluid flow. Within the previous simulation, the simulated flowtube was intended to mimic the physical prototype flowtube as accurately as possible. In this trial, a design consideration for future prototypes is modeled. Specifically, the internal flow straightener was removed. Due to the placement of the internal flow straightener, it appears that the flow within the specimen holder would be unaffected. As such, it is hypothesized that the external flow

straighteners are sufficient in reducing secondary fluid motion. If the internal flow straightener is redundant or unnecessary, the design of future prototypes could be simplified. This design change is reflected in Figure 26 below. Volume was extracted and modeled in a similar manner to the previously described simulations.

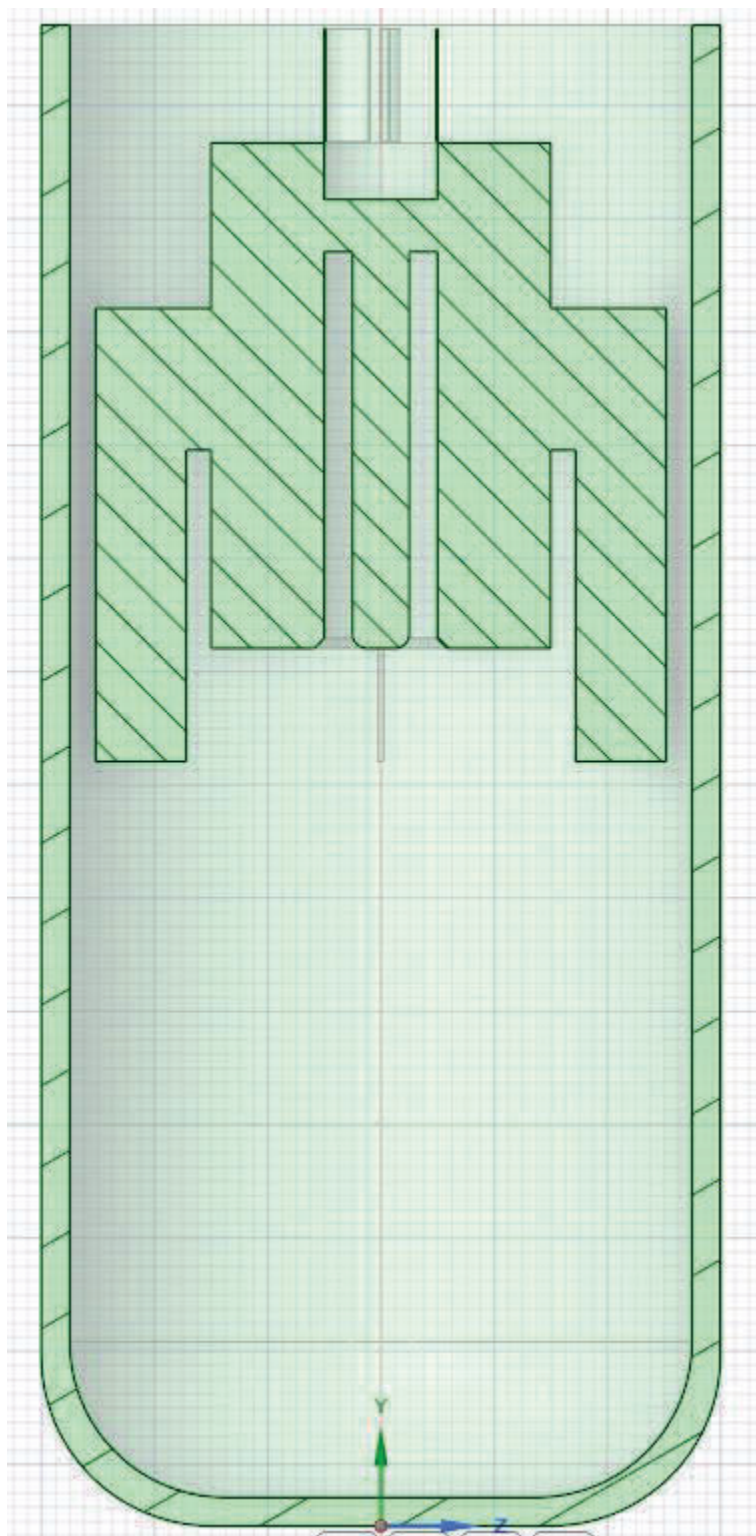


Figure 26. Cross-section view of flowtube geometry with external baffles

In addition to updating the geometry, the mesh was updated for this trial as well. For the 1000 RPM and 2000 RPM simulations, a uniform mesh of 2 mm was used throughout the entire fluid body. These settings caused 310,669 nodes and 1,636,721 elements to be present in the final mesh. This mesh is shown in Figure 27 below.

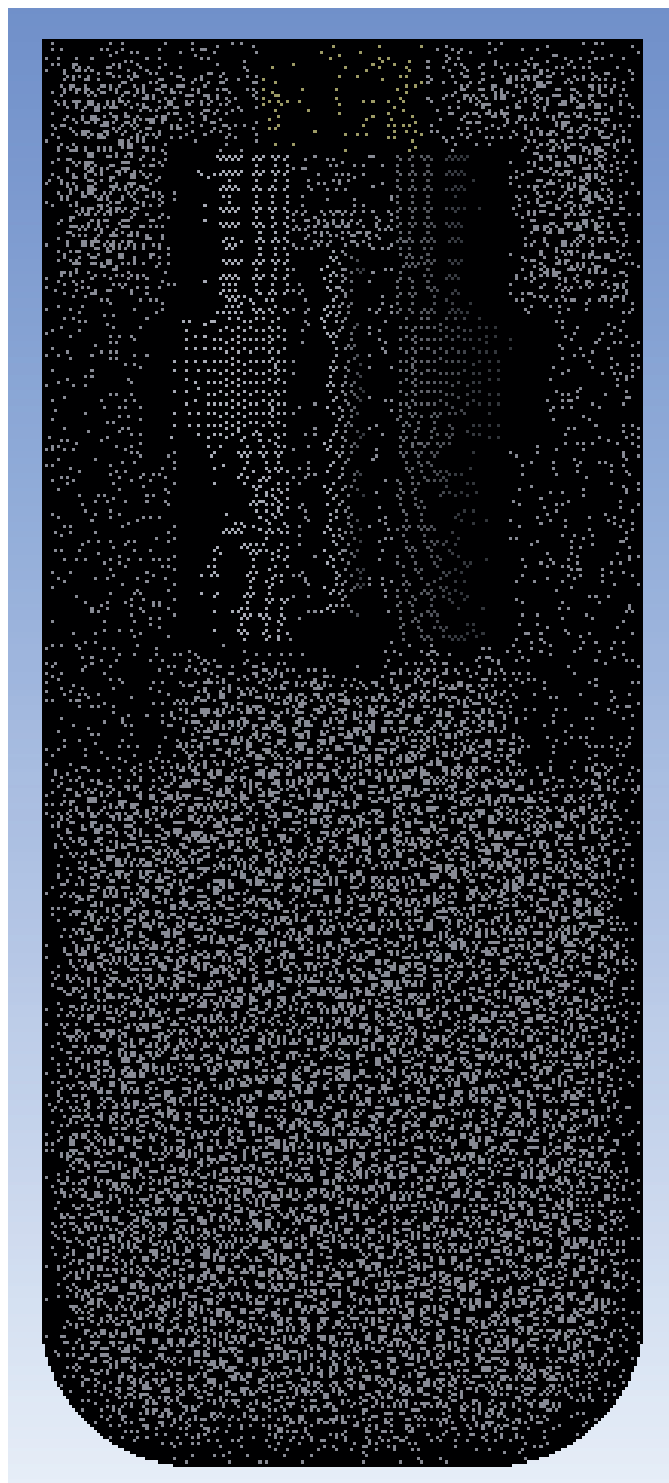


Figure 27. Cross-section of mesh used for 1000 RPM and 2000 RPM simulations in 4 L glass cell with external baffles

A more refined mesh was created for the 5000 RPM trial in order to obtain  $y^+$  values within the desire range. The bulk solution was changed to a uniform mesh size of 3 mm, impeller fluid body was set to a mesh size of 1 mm, and internal specimen holder surface was set to a mesh size of 0.75 mm at the surface with 1.2 growth rate. These settings created a mesh with 233,972 nodes and 1,219,648 elements. This mesh is shown in Figure 28 below.

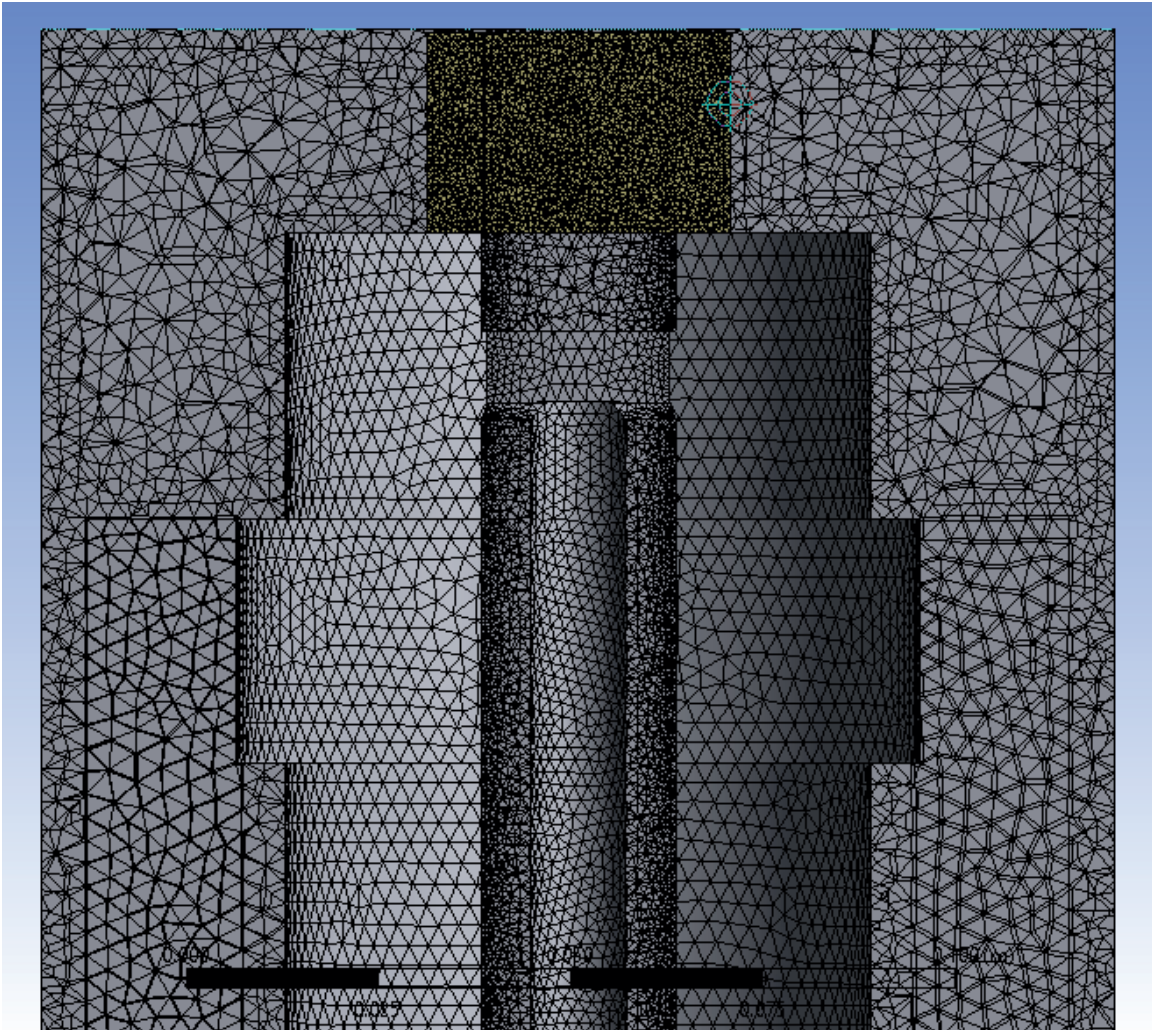


Figure 28. Cross-section of refined mesh used for 5000 RPM simulation in 4 L glass cell with baffles

#### 6.4 Reduced Counter Electrode Diameter

In addition to the removal of components such as the internal flow straightener, design considerations such as altering relative size and shape of components can be examined using CFD. As a proof of concept, the central counter electrode was reduced in diameter from 0.5 inches to 0.25 inches. It should be noted that the effect of this change

on the corrosion of specimens within the flowtube is not considered for this proof-of-concept model. It is possible that this design change would not be viable within a working prototype due to the surface area of the counter electrode being reduced to a point where it becomes insufficient for the corrosion reaction. Once it is established that design considerations, such as changing the size of components or adding/removing components entirely, can be implemented within the CFD model, then future design considerations can be implemented without the need to fabricate an entire physical prototype.

The Ansys SpaceClaim model of the flowtube used to test the smaller counter electrode is shown in Figure 29 below and remains nearly identical to the previous model showcasing the flowtube with external baffles. The only difference is the reduction of diameter of the central counter electrode. Similarly, the mesh sizing was maintained to be identical to the previously discussed simulation to achieve consistency. This consistency allows for future design considerations to be accounted for in a relatively simpler manner.

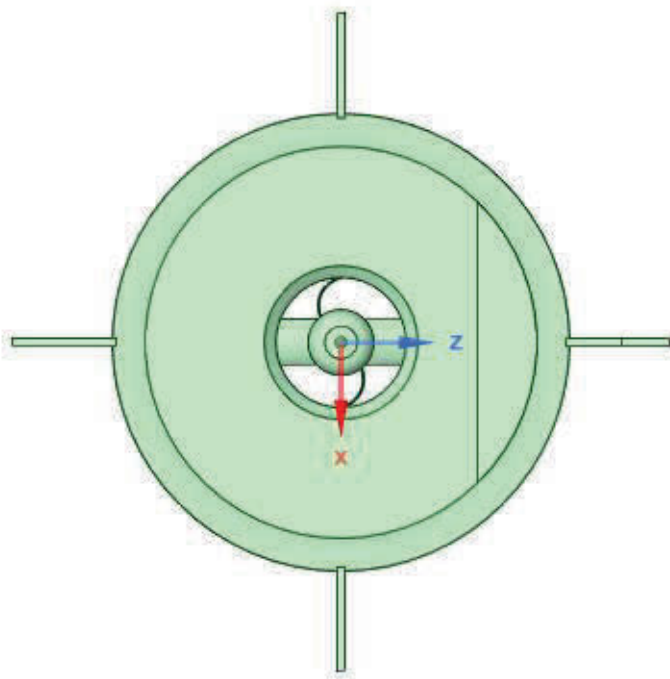


Figure 29. Bottom view of flowtube with 0.25-inch diameter counter electrode

## **Chapter 7: Methodology for Modeling RDE Simulations Using CFD**

### **7.1 Mass Transfer CFD Model for RDE Simulation**

Similar to the Flowtube corrosion testing detailed above, a Rotating Disk Electrode (RDE) was modeled in Ansys Fluent. The rationale for creating a CFD model remains the same as discussed in the Rationale for CFD Modeling section within Chapter 6. The primary purpose for performing the CFD simulations specifically for an RDE is to model a well-known system. This will validate that Ansys Fluent is capable of accurately simulating corrosion. Once it is established that corrosion is accurately simulated for a known system within Ansys Fluent, it is possible to model an unknown system, such as the flowtube, within a CFD model in order to implement future design considerations and understand their implications on corrosion. Furthermore, it becomes possible to model the corrosion without the need for resource intensive laboratory testing. In order to establish the viability of the CFD models, comparison to theoretical and laboratory results is necessary.

Similar to the flowtube simulations described above, the RDE system must first be modeled within Ansys SpaceClaim. Due to the relatively simple nature of an RDE, it is possible to create a two-dimensional geometry rather than a full three-dimensional geometry. Not only is a two-dimensional geometry possible, but also Ansys Fluent allows for the use of half of a cross section of the RDE system due to the axisymmetric nature of the RDE system. Within Ansys Fluent, the geometry is rotated around an axis in order to model the equivalent of a full three-dimensional geometry. This is described in further detail within Chapter 9.3 of the Ansys Fluent User's Guide.<sup>23</sup> For this simulation the

cross-section is intended to mimic the experimental setup shown in Figure 6. The glass cell can be thought of as a cylinder with rounded bottom corners, a height of 100 mm, and an inner diameter of 114 mm. The RDE shaft can be thought of as a cylinder with an outer diameter of 12 mm. The active surface on the tip of the RDE is set as a circle 5 mm in diameter and is centered on the bottom of the RDE shaft. The bottom of the shaft is set 30 mm from the bottom of the glass cell and extends the entire length of the glass cell above that. The RDE shaft is centered within the glass cell. As mentioned above, though, the geometry created in Ansys SpaceClaim is intended to be half of a two-dimensional cross-section of the entire system. As such, the glass cell and RDE shaft are modeled as rectangles and the active area on the tip of the RDE shaft is modeled as a line. Similar to the flowtube, the geometry needs to be “filled” with a modeled fluid and the physical structures of the glass cell and RDE shaft are removed. This allows for the fluid to be modeled alone. However, unlike the flowtube, the glass cell and RDE structure do not need to be modeled before “filling” the glass cell with fluid. Instead, the fluid itself is modeled directly within Ansys SpaceClaim as a rectangle with a smaller rectangle cut out of it to represent the RDE shaft, as shown in Figure 30 below.

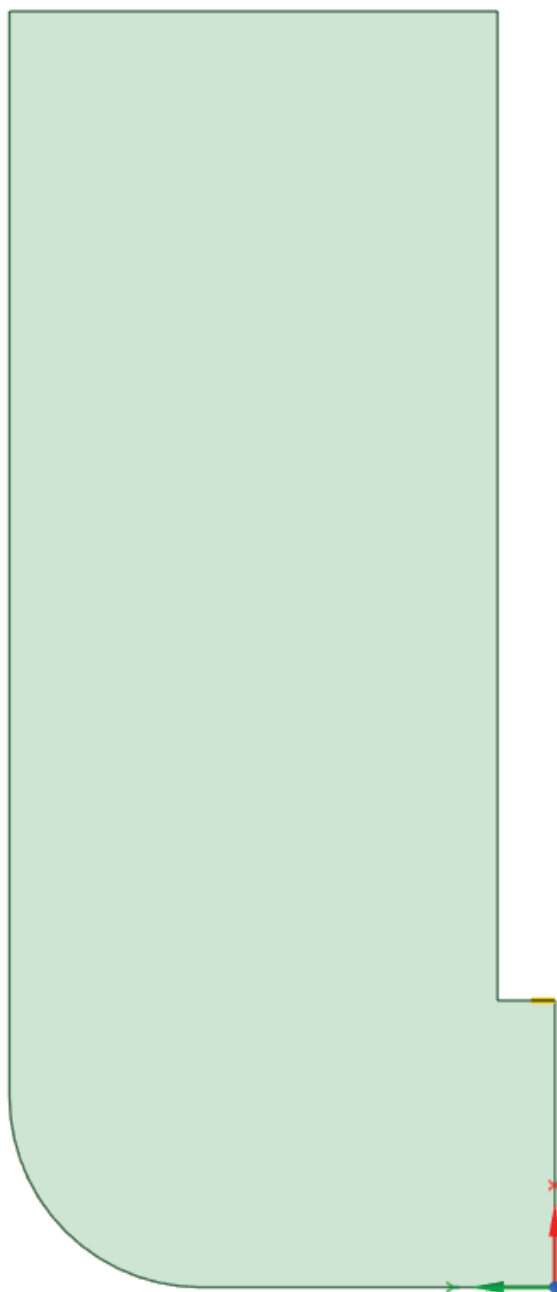


Figure 30. SpaceClaim model of RDE in 1 L glass cell

Before a CFD model can be created for the RDE system described in the Preliminary RDE Experiments section of this thesis, a mass transfer simulation was

created in Ansys Fluent. The reason for this is because mass transfer becomes a limiting factor within the corrosion experiments. Furthermore, establishing that Ansys Fluent is capable of producing verified results for a simpler system, such as mass transfer only, then allows for aid in debugging a more complex situation, such as corrosion. This mass transfer simulation focuses on the diffusion of hydrogen ions ( $H^+$ ) from the bulk solution to the active surface of the RDE. Comparing the results of this simulation at various rotational rates to literature mass transfer equations allows for validation of the model created within Ansys Fluent. In order to set up the mass transfer simulation,  $H^+$  is added as a species within the bulk solution with an initial mass fraction of 0.000139. This mass fraction is equivalent to a pH of  $4.0 \pm 0.1$  in the bulk solution. Also, the diffusivity of the  $H^+$  ions is set to  $3.2 \times 10^{-9} \frac{m^2}{s}$  and the diffusivity of the mixture is set to  $1 \times 10^{-8} \frac{m^2}{s}$ . Additionally, the viscosity of the mixture was set to  $1 \times 10^{-6} \frac{kg}{m \times s}$ .<sup>25</sup> Lastly, the density of the  $H^+$  ions was set to be the same as the density of water in order to simplify the mixing calculations; this is fair as the  $H^+$  will exist as  $H_3O^+$  (hydronium) rather than a free cation. As a simplification necessary to achieve a steady state solution, the walls of the glass cell were designated within Ansys Fluent as sources of  $H^+$  ions. While unrealistic, this simplification is equivalent to adjusting the pH of an experiment due to the consumption of hydrogen ions in the reduction of hydrogen.

After running the simulation within Ansys Fluent, the concentration profile of  $H^+$  ions can be exported and analyzed. Specifically for this analysis, the concentration was observed at every mesh point from the surface of the RDE to 0.4 mm away from the RDE along a straight line 1 mm from the center line of the RDE. Once the concentration

profile was plotted, a trend line was generated to extend through the linear region closest to the RDE surface. The distance associated with the intersection of this line and the concentration within the bulk solution was recorded as the mass transfer boundary layer thickness. For each simulated rotational speed, the mass transfer boundary layer thickness was compared to the calculated theoretical value of the mass transfer boundary layer thickness in order to determine the accuracy of the CFD simulations.

## Chapter 8: Results and Discussion for CFD Model of Flowtube

### 8.1 Simplified Preliminary Model

#### 8.1.1 *Transient Simulation Results*

The first simulation performed was the transient simulation using a rotational rate of 5000 RPM and a salt concentration at the bottom of the glass cell of 0.01 mass fraction. The initial salt concentration for all points within the glass cell was set to 0 mass fraction salt. The transient simulation was performed over the course of 416 timesteps, each timestep being 0.05 seconds. This means the transient simulation ran for 20.8 seconds of equivalent run time for the flowtube. This took roughly 7 hours of computational time to accomplish. It should be noted that steady state was not achieved within this timeframe. Each timestep was allowed to run for 200 iterations before continuing to the next timestep. It is believed that this number of iterations was sufficient to reach near convergence for the model at each timestep. From previous experimentation, it was observed that the system reached relatively consistent values for residuals after 100-200 iterations. For these initial simulation trials, it was determined that 200 iterations per timestep would be sufficient for the following analysis.

For the purposes of this analysis, only the mass fraction of salt as well as the velocity profile were examined in the transient simulation. Evolution of the salt concentration is shown in Figure 31 and Figure 32 below.

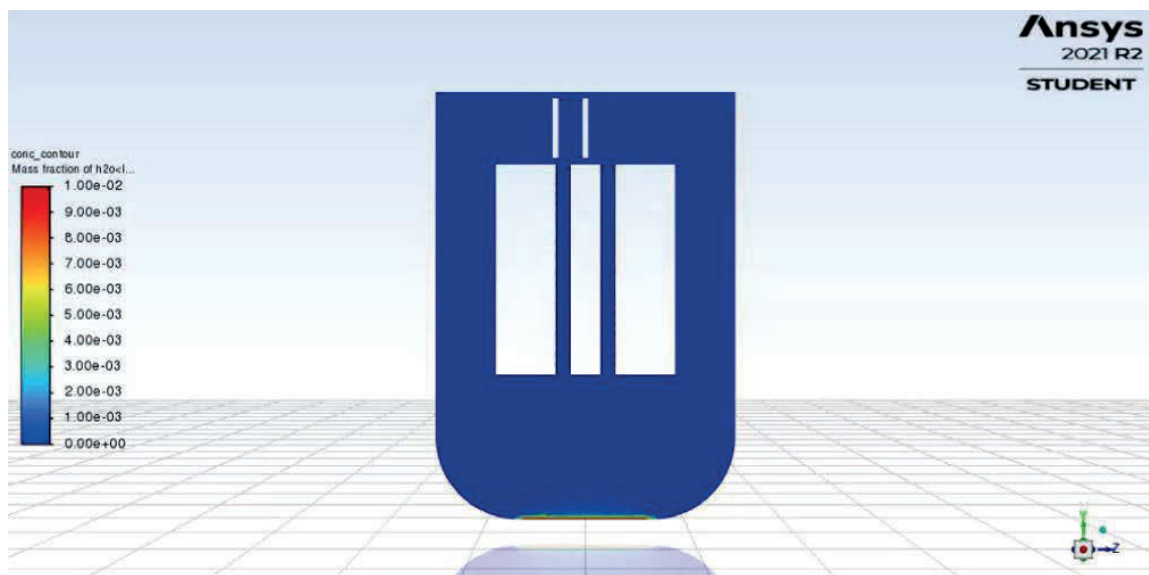


Figure 31. Initial salt concentration on the base of the glass cell

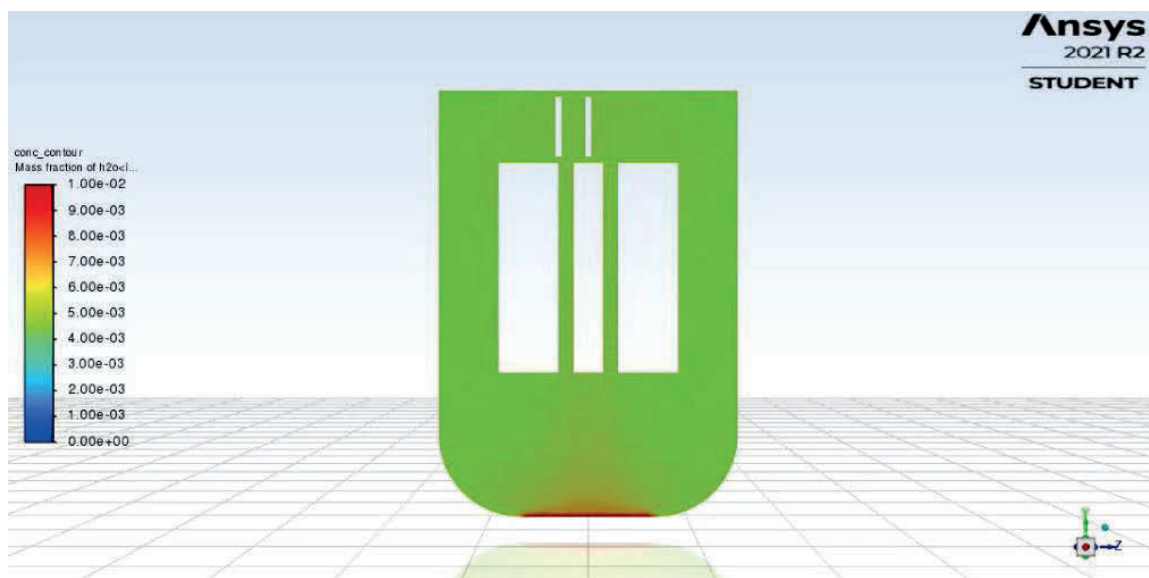


Figure 32. Salt concentration at 20.8 seconds throughout the glass cell

As shown in the figures above, the salt begins at a high concentration at the bottom of the cell. As time progressed and the impeller moved fluid around the glass cell,

the salt was distributed throughout the cell relatively uniformly. Steady state simulations have shown that the concentration will eventually become a homogenous 0.01 mass fraction salt if the simulation is able to run for long enough. The velocity profile, while not the primary focus of the transient experiments, was also examined in this simulation. Evolution of the velocity profile within the glass cell, shown by velocity pathlines, which indicate the trajectory of imaginary particles as they move throughout the glass cell. In this simulation, the imaginary particles were “released” from the bottom of the glass cell and from the outside of the enclosure surrounding the impeller. The evolution of the velocity profile is shown in Figure 33 and Figure 34 below.

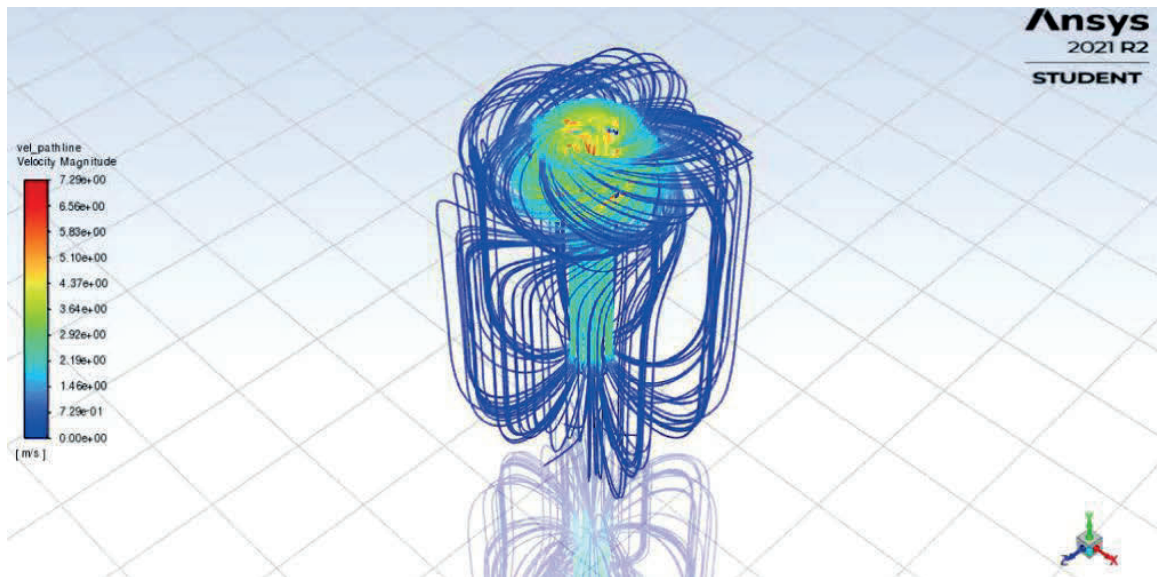


Figure 33. Initial velocity pathlines in glass cell

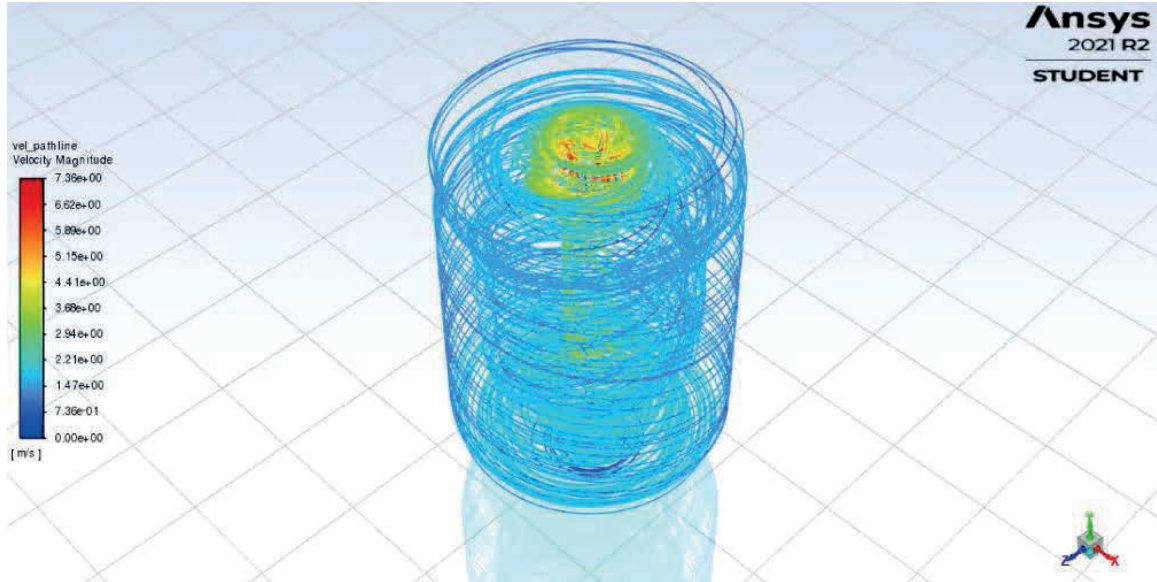


Figure 34. Final velocity pathlines in glass cell

As shown in the figures above, the imaginary particles start mostly surrounding the impeller enclosure with a few starting at the bottom of the glass cell. As the velocity has not yet had time to develop, almost all the motion is surrounding the impeller with very little fluid movement down the sides of the glass cell. Figure 34 shows that, over time, the velocity profile developed into a swirling motion in the bulk solution.

Furthermore, the simulation indicated that the swirling motion was also present within the specimen holder to a lesser degree than in the bulk fluid outside the flowtube. This has been validated by experimentation with the physical flowtube apparatus, which showed the same swirling motion if the internal flow straightener and external flow straightening fins were not in place. This makes sense, as the internal flow straightener and external flow straightening fins were removed from this geometry for simplicity.

Further simulations will showcase the difference those additions make on the velocity profile of the flowtube.

### ***8.1.2 Steady State Simulation Results***

Steady state simulations were performed for rotational rates of 1000 RPM, 2000 RPM, and 5000 RPM. This was done to showcase the difference rotational rate, and therefore fluid velocity, makes on the velocity profile, turbulent kinetic energy, and  $y^+$  values in the glass cell. It should be noted that for all steady state simulations discussed herein, the species transport model was turned off. Through preliminary experimentation, it was found that the salt concentration at steady state will reach a homogeneous concentration of 0.01 mass fraction salt once the system reaches steady state. This is not expected to change with rotational speed. Furthermore, the salt concentration in solution is not expected to have any significant impact on the flow within the system. On top of that, the addition of the species transport model increased the number of iterations it took for the system to reach convergence substantially. Therefore, in the interest of time and because the addition of the species transport model would not add any significant value to this analysis, the salt concentration was removed from the steady state simulations.

For most simulation results, a vertical cross-section will be used to demonstrate the effect of the parameter of interest. Because the flowtube is expected to be axisymmetric, the vertical cross-section will be considered an accurate representation of the system as a whole. Simulation results showcase the velocity profiles represented by velocity vectors in a vertical cross-section of the glass cell as well as a horizontal cross-section of the specimen holder. The vertical cross-section will serve as a representation of

the fluid motion within the glass cell as a whole whereas the horizontal cross-section will more accurately show the bulk fluid motion. The turbulent kinetic energy will be shown as a vertical cross-section of the glass cell. The turbulent kinetic energy is a measure of the turbulence present in the solution. The  $y^+$  value will be shown as a vertical cross-section of the glass cell. The  $y^+$  value is a non-dimensional distance from the wall and can be seen as a representation of a ratio between the turbulent influences and the laminar influences within solution in the vicinity of solid boundaries. In these simulations, the  $y^+$  value can be thought of as aiding in the analysis to understand when the mesh is too coarse or too fine. For the no slip wall functions used within the  $k-\epsilon$  model utilized in these simulations,  $y^+$  values between 11.63 and 100 are desired to show sufficient mesh resolution, as discussed in the Advanced Momentum Transport class.<sup>16</sup> If the  $y^+$  value near the wall exceeds 100, then the mesh needs to be finer, or the flow rate needs to be decreased in order to expand the boundary layer close to the wall. If the  $y^+$  value near the wall is less than 11.63, this is an indication that the mesh should be coarser, or the flow rate needs to be increased in order to decrease the boundary layer. In short, the  $y^+$  value can be used as an indicator for whether or not the simulation is adequately representing the turbulent and laminar flow in the near-wall region. The  $y^+$  values indicate whether the spatial discretization points are a sufficient distance from the boundary to accurately take into account the boundary layer.

8.1.2.1 **1000 RPM.** Results for the 1000 RPM simulation are shown in Figure 35, Figure 36, Figure 37, Figure 38, and Figure 39 below.

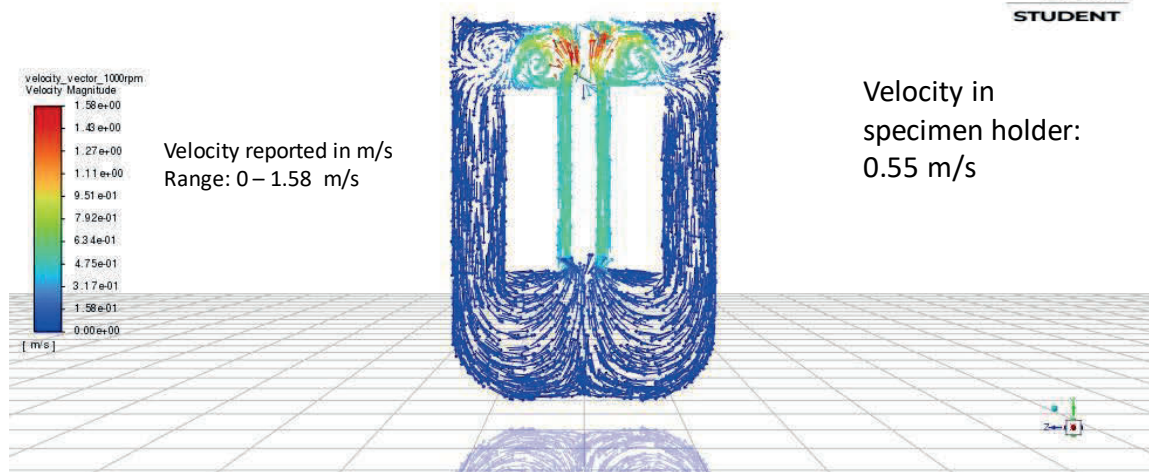


Figure 35. Velocity vectors in vertical cross section of preliminary model at 1000 RPM

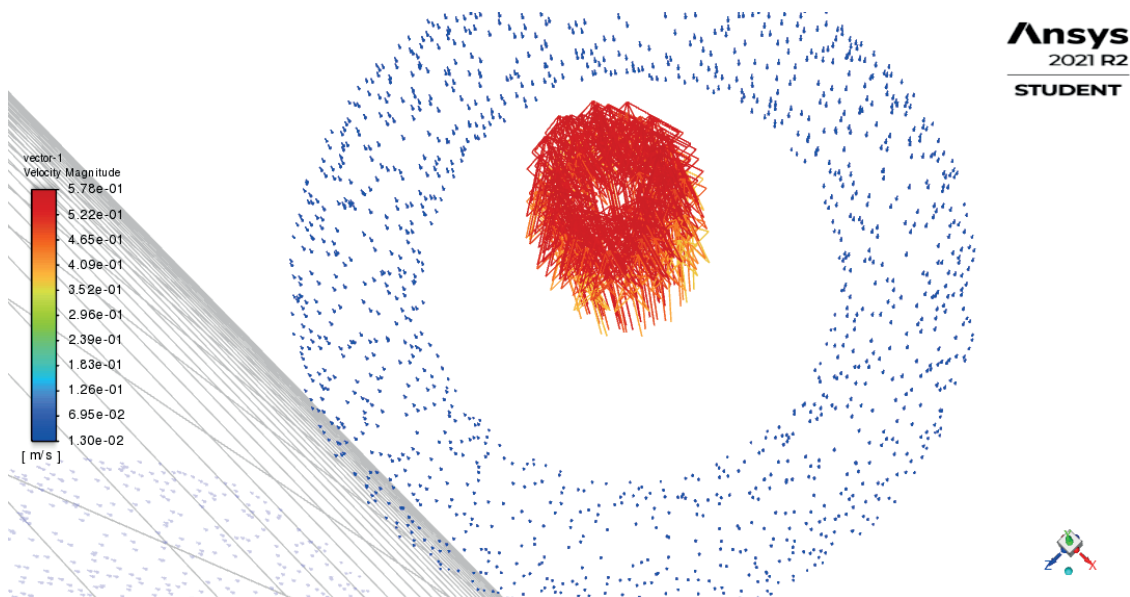


Figure 36. Velocity vectors in horizontal cross section of preliminary model at 1000 RPM

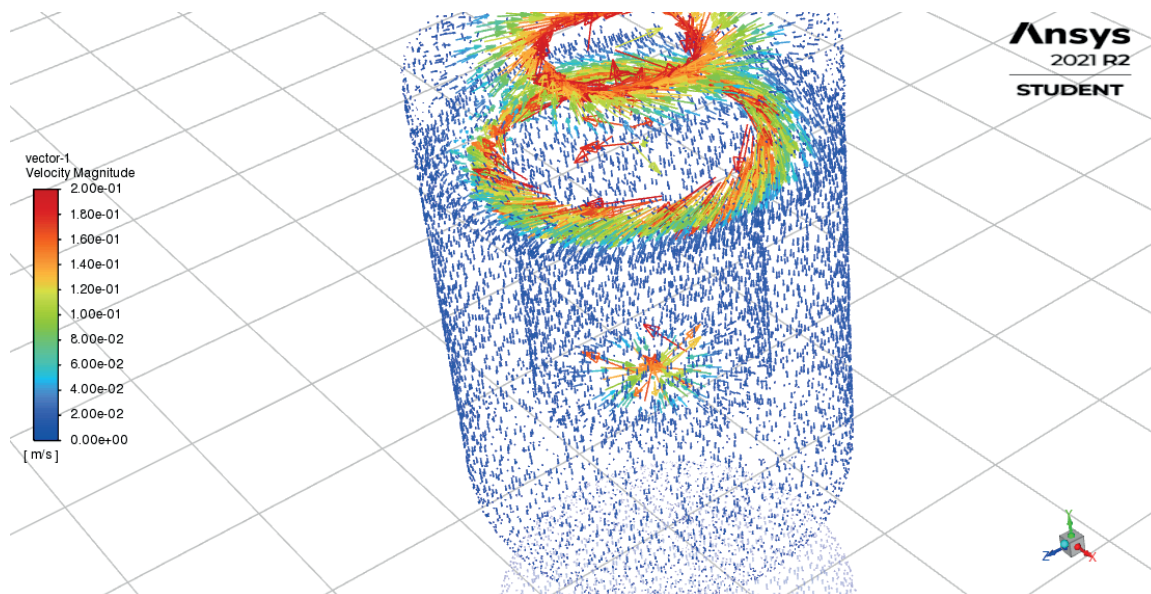


Figure 37. Velocity vectors on exterior of preliminary model at 1000 RPM

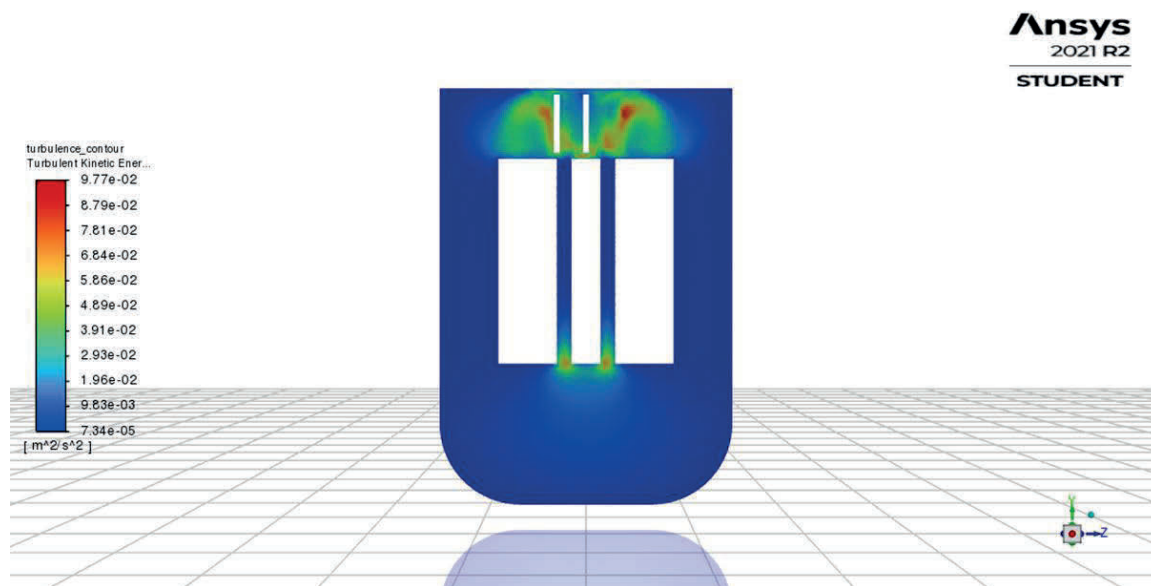


Figure 38. Turbulent kinetic energy in vertical cross section of preliminary model at 1000 RPM

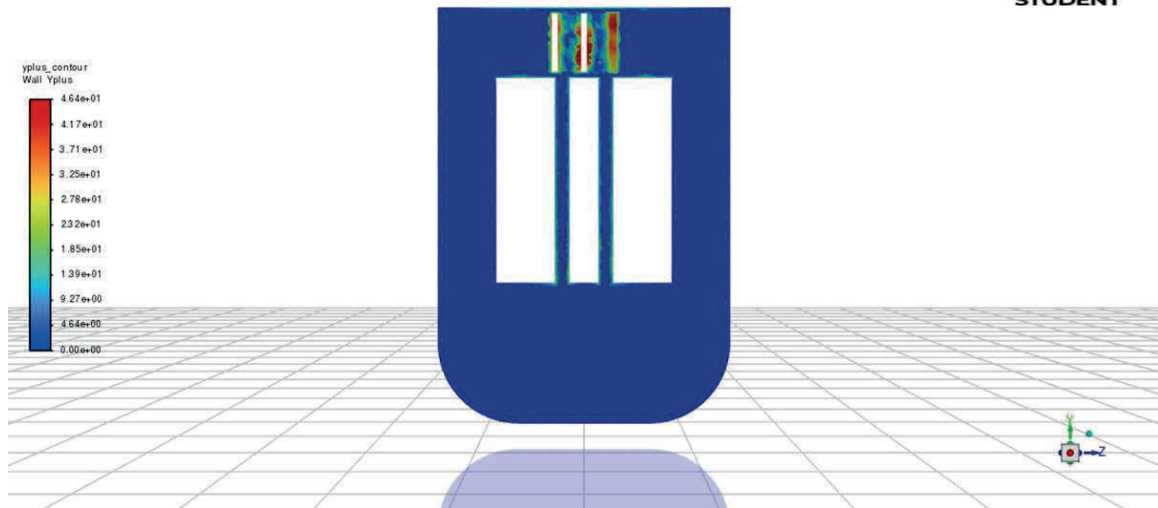


Figure 39.  $y^+$  values in vertical cross section of preliminary model at 1000 RPM

Figure 35, Figure 36, and Figure 37 show the velocity profile at 1000 RPM from different angles and vantage points. They show that the flow rate is highest at the impeller and that the flow circulates around the glass cell as expected. The velocity within the specimen holder was found to be approximately 0.55 m/s. That said, Figure 36 and Figure 37 show that the swirling motion seen in the transient solution at 5000 RPM is not present at steady state and 1000 RPM. This is likely due to the fact that the rotational speed of the impeller is significantly lower. With the reduced rotational speed, there is insufficient energy present to cause bulk rotational movement of solution. There is also slight secondary motion present within Figure 35 near the top of the glass cell. This is likely caused by the outward motion of the fluid being stopped by the walls of the glass cell. After this, some fluid travels down towards the bottom of the glass cell while some travels upwards towards the top of the glass cell. Since there is so little space before

hitting the top “wall” of the glass cell, the fluid that traveled upwards ends up circulating downwards again in this observed secondary motion.

Figure 38 shows that the turbulent kinetic energy in the glass cell is at its greatest magnitude near the impeller. This is expected behavior because the impeller is a moving object that directly interferes with the fluid surrounding it. It should also be noted that there is a clear spike in turbulent kinetic energy near the entrance to the specimen holder. As noted earlier, this simplified geometry ignores the beveled edge at the inner diameter of the specimen holder and the bullnose edge around the outer edge of the counter electrode. Further experimentation is expected to show that these design considerations reduce the turbulence in this entrance region.

Figure 39 shows that the  $y^+$  values within the glass cell reach a maximum value of 46.4 for this simulation; this maximum is located at the impeller. This maximum is expected because of the turbulence caused by the impeller’s rotation. There are other regional spikes in  $y^+$  values near the walls of the specimen holder and counter electrode; these  $y^+$  values are around 15. Because the values of  $y^+$  near the walls of this system exist within the constraints outlined above, it can be concluded that the mesh sizing is sufficient for simulations performed at 1000 RPM.

8.1.2.2 **2000 RPM.** Results for the 2000 RPM simulation are shown in Figure 40, Figure 41, Figure 42, Figure 43, and Figure 44 below.

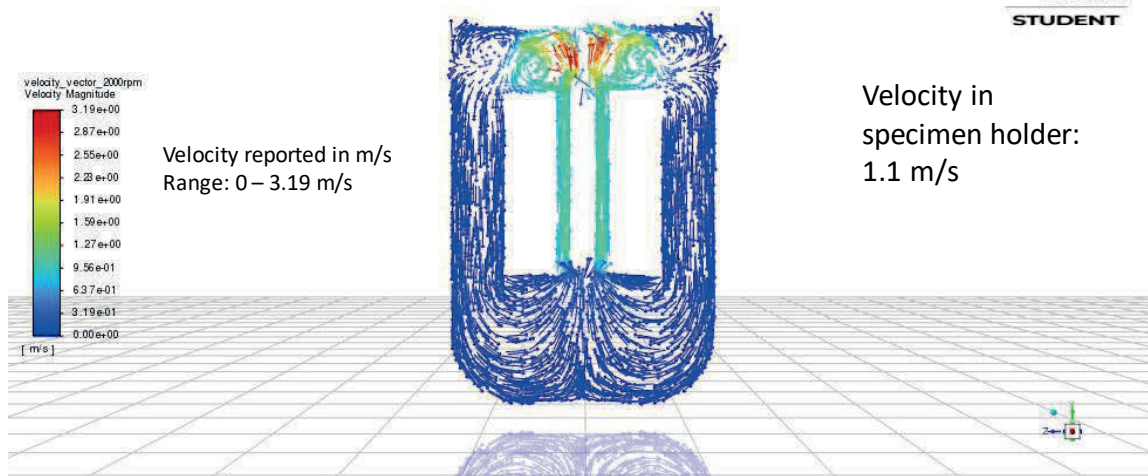


Figure 40. Velocity vectors in vertical cross section of preliminary model at 2000 RPM

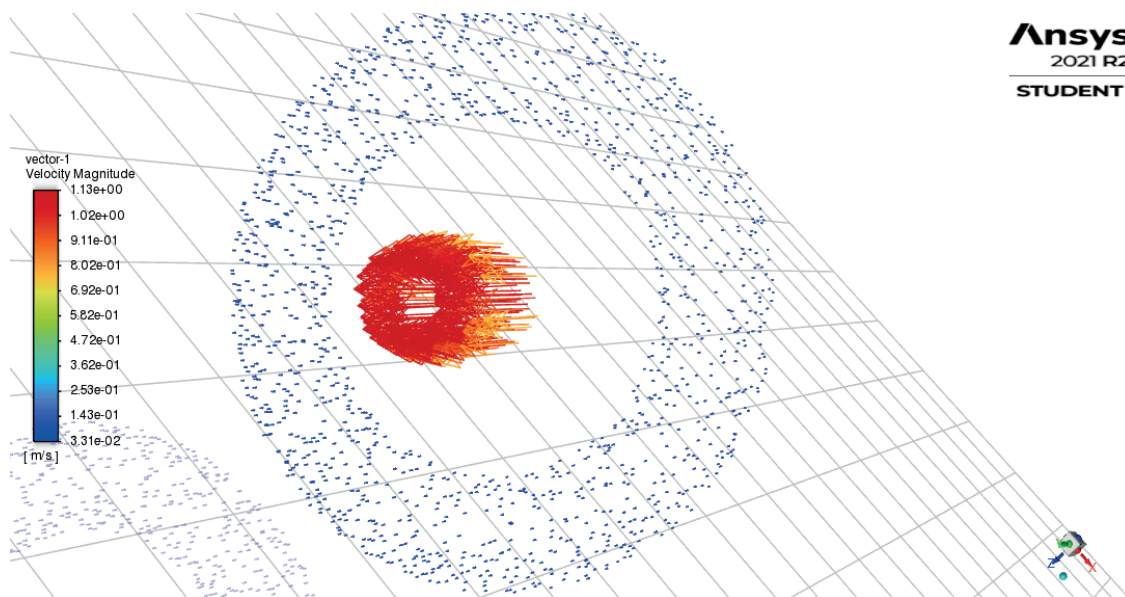


Figure 41. Velocity vectors in horizontal cross section of preliminary model at 2000 RPM

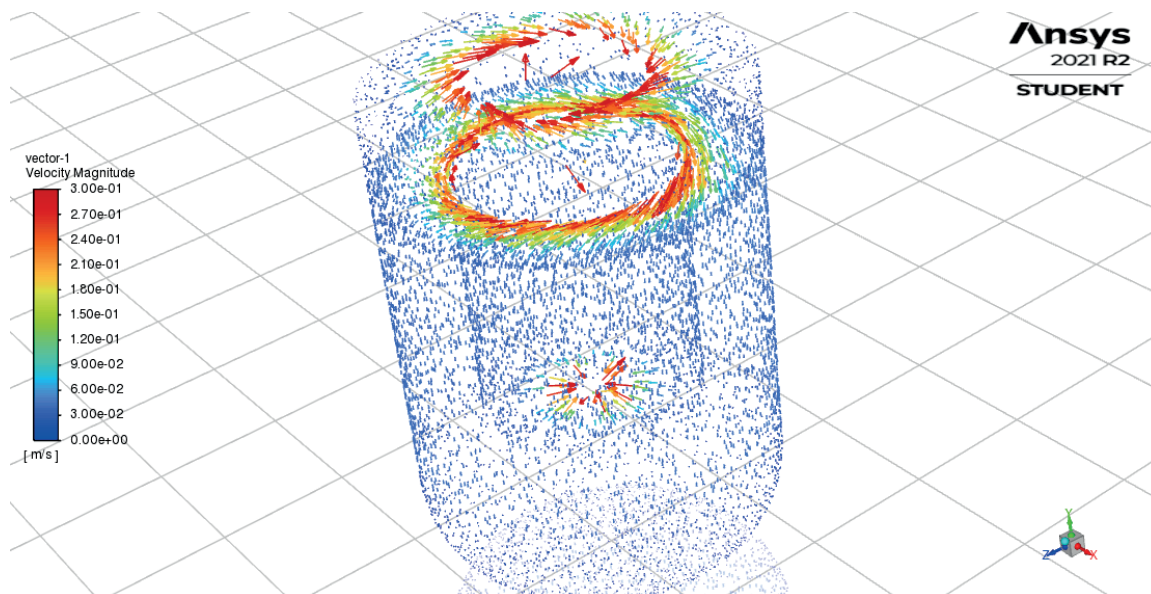


Figure 42. Velocity vectors on exterior of preliminary model at 2000 RPM

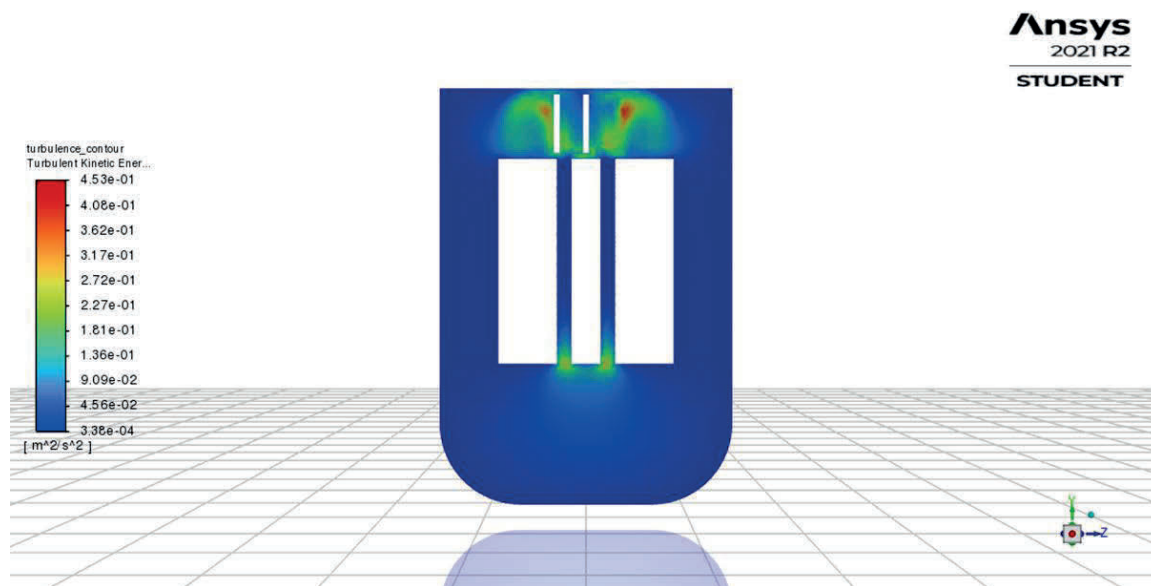


Figure 43. Turbulent kinetic energy in vertical cross section of preliminary model at 2000 RPM

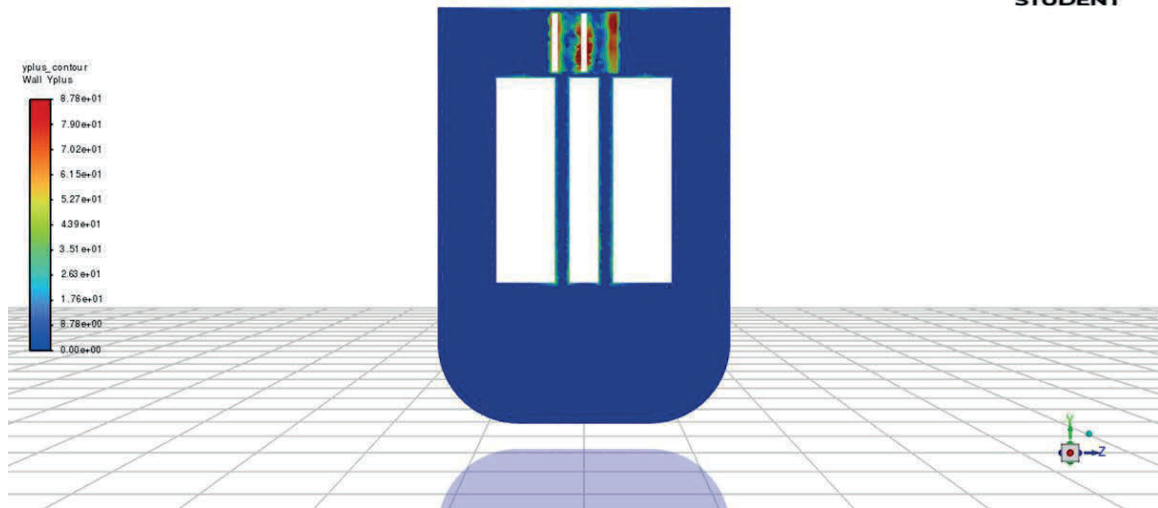


Figure 44.  $y^+$  values in vertical cross section of preliminary model at 2000 RPM

Figure 40, Figure 41, and Figure 42 show the velocity profile at 2000 RPM from different angles and vantage points. The results are very similar to the 1000 RPM simulation. As described before, the fluid motion is of the greatest magnitude at the impeller, and there is another area of increased fluid velocity within the specimen holder. The velocity within the specimen holder was found to be approximately 1.1 m/s. The fluid circulates through the glass cell without significant swirling motion at 2000 RPM, just like at 1000 RPM. The secondary motion mentioned in the 1000 RPM simulation near the top of the glass cell is more pronounced in the 2000 RPM simulation. It appears that the primary difference between 1000 RPM and 2000 RPM velocity profiles is the magnitude of velocity.

Figure 43 shows the turbulent kinetic energy in the glass cell with a rotational rate of 2000 RPM. There is an increased magnitude of turbulent kinetic energy when

compared to the 1000 RPM simulation, but there is minor difference beyond that. The same analysis applies. Turbulence is highest at the impeller and at the entrance to the specimen holder.

Figure 44 shows that the  $y^+$  values within the glass cell reach a maximum value of 87.8 for this simulation; this maximum is located at the impeller. The regional spikes on the inside of the specimen holder have  $y^+$  values around 25. Because the values of  $y^+$  near the walls of this system exist within the constraints outlined above, it can be concluded that the mesh sizing is sufficient for simulations performed at 2000 RPM.

8.1.2.3 **5000 RPM.** Results for the 5000 RPM simulation are shown in Figure 45, Figure 46, Figure 47, Figure 48, and Figure 49 below.

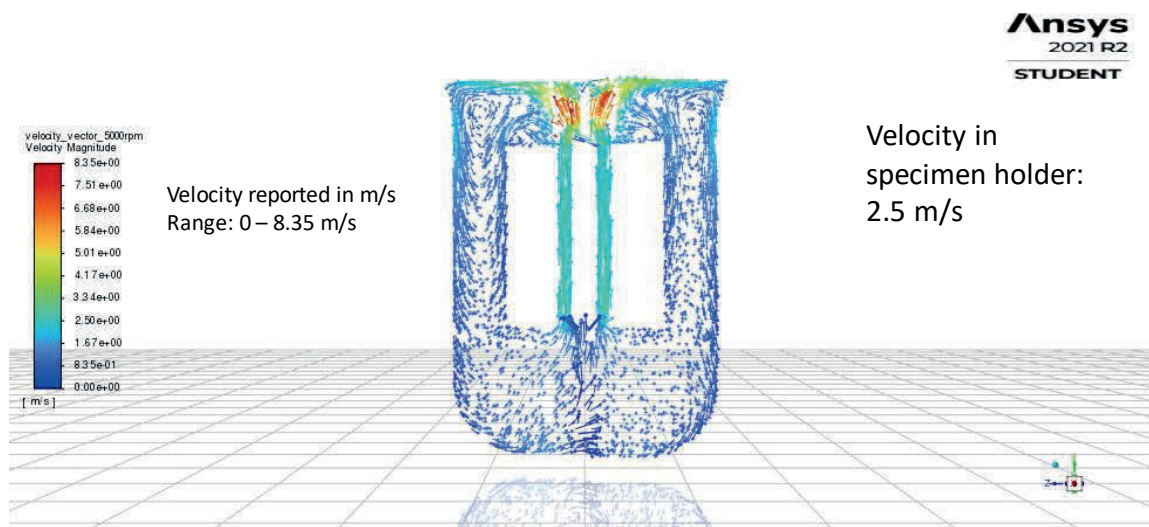


Figure 45. Velocity vectors in vertical cross section of preliminary model at 5000 RPM

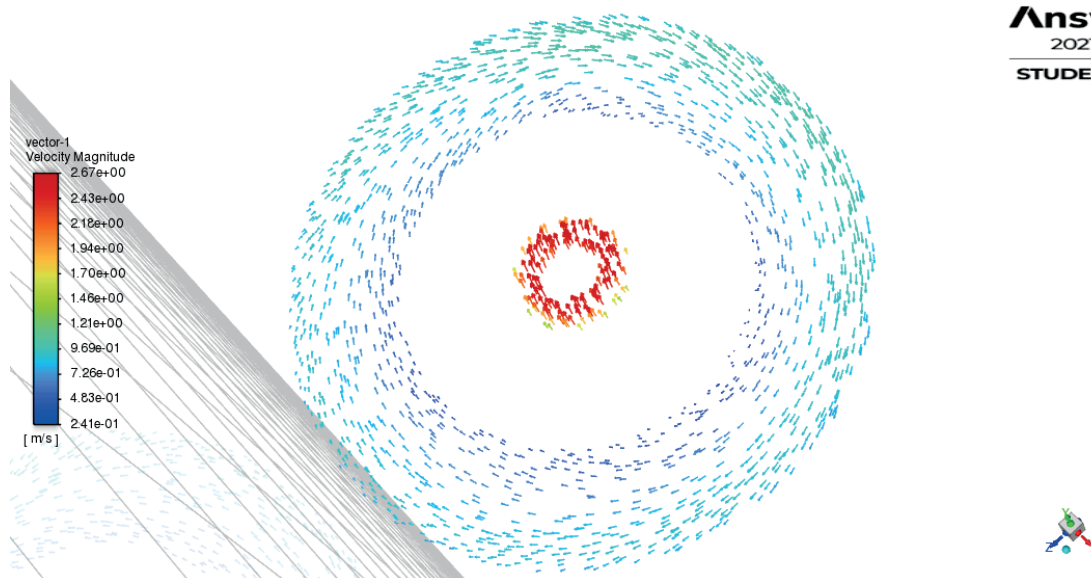


Figure 46. Velocity vectors in horizontal cross section of preliminary model at 5000 RPM

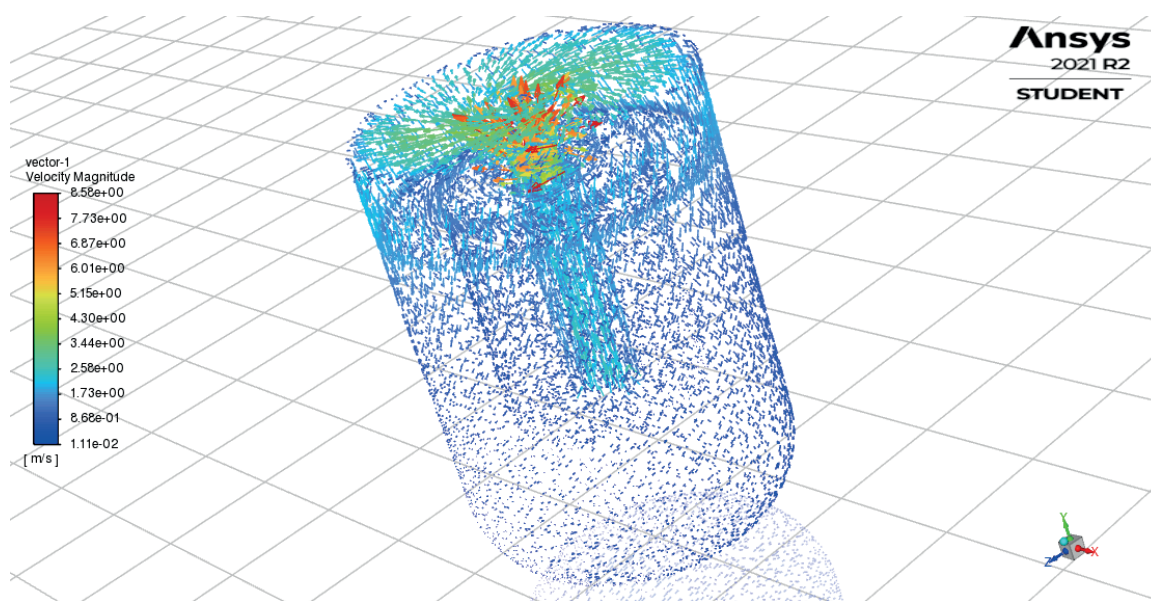


Figure 47. Velocity vectors on exterior of preliminary model at 5000 RPM

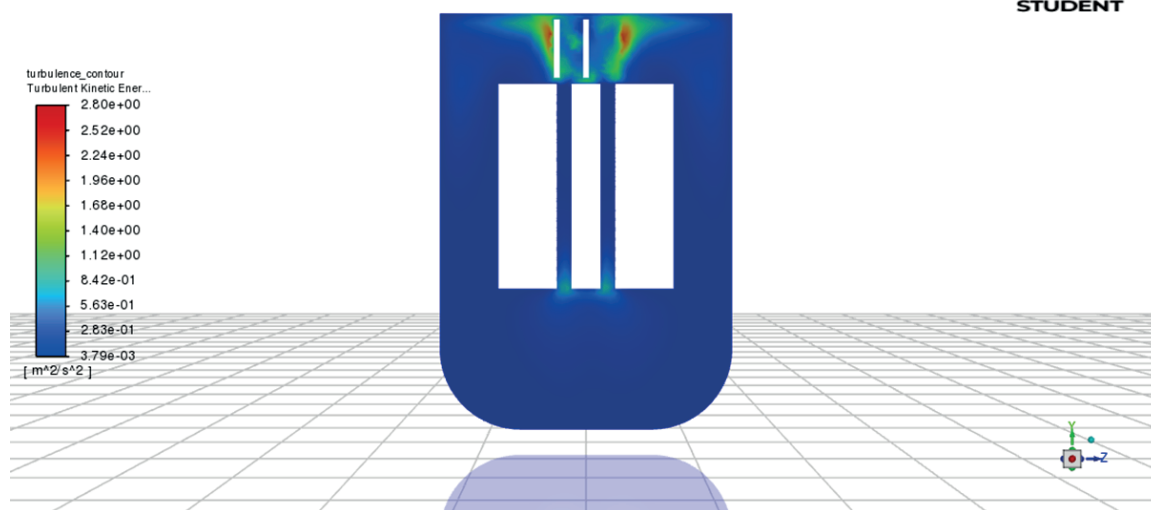


Figure 48. Turbulent kinetic energy in vertical cross section of preliminary model at 5000 RPM

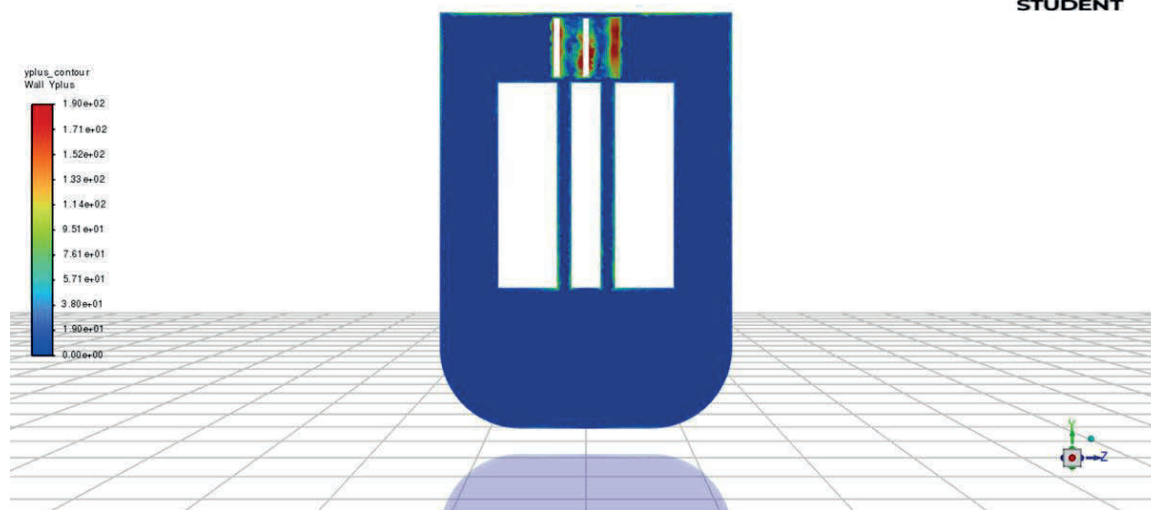


Figure 49.  $y^+$  values in vertical cross section of preliminary model at 5000 RPM

Figure 45, Figure 46, and Figure 47 show the velocity profile at 5000 RPM from different angles and vantage points. Figure 45 shows a very similar story to the previous rotational speeds; the magnitude of fluid velocity is now higher, and the secondary motion near the top of the glass cell is even more pronounced. The velocity within the specimen holder was found to be approximately 2.5 m/s. Figure 46 and Figure 47 show that there is actually a significant difference in the flow pattern. In the 5000 RPM simulation, there is a noticeably clear swirling motion present in the bulk fluid as well as slight swirling motion present in the specimen holder. It should be noted that this swirling motion is undesirable.

Figure 48 shows the turbulent kinetic energy in the glass cell with a rotational rate of 5000 RPM. There is a further increased magnitude of turbulent kinetic energy when compared to the previous simulations. At first glance, it appears that there is less turbulence at the entrance to the specimen holder as well. However, closer inspection reveals that the turbulent kinetic energy near the impeller is now so large that the scale is skewed in such a way that makes the entrance to the specimen holder appear less significant.

Figure 49 shows that the  $y^+$  values within the glass cell reach a maximum value of 190 for this simulation; this maximum is located at the impeller. The regional spikes on the inside of the specimen holder have  $y^+$  values around 82. The top of the glass cell also appeared to have a regional spike in  $y^+$  value around 120. Because the  $y^+$  values near the impeller and near the top of the glass cell exceed the threshold for acceptable  $y^+$  values, it can be concluded that the mesh is not able to accurately predict fluid motion near the

impeller or near the top of the glass cell at 5000 RPM. In order to overcome this, the mesh will have to be finer near those regions. That said, the  $y^+$  values appeared to be within an acceptable range near the walls of the specimen holder, which is the region of interest. This indicates that the fluid flow is sufficiently modeled at those points. It should be noted that for the purposes of designing the next flowtube prototype, the fluid motion within the specimen holder is the most significant.

As a summary, the rotational speed of the impeller appeared to have a linear relationship with the measured superficial fluid velocity within the specimen holder. This relationship is shown in Figure 50 below. It should be noted that the Reynolds number is shown, as it would be used to compare the superficial fluid velocity within the flowtube to the analogous fluid velocity within a pipeline. In all experimental cases, the Reynolds numbers indicated fully developed turbulent flow within the specimen holder, as the threshold for fully developed turbulent flow in an annulus is a Reynolds number value of 4000.<sup>15</sup> It was anticipated that the flow through the specimen holder would be turbulent. These results indicate that all flow through the flowtube specimen holder will be turbulent unless the rotational speed is less than 495 RPM. In order to ensure properly developed turbulent flow for repeatable results, the rotational speed should never be set lower than 500 RPM.

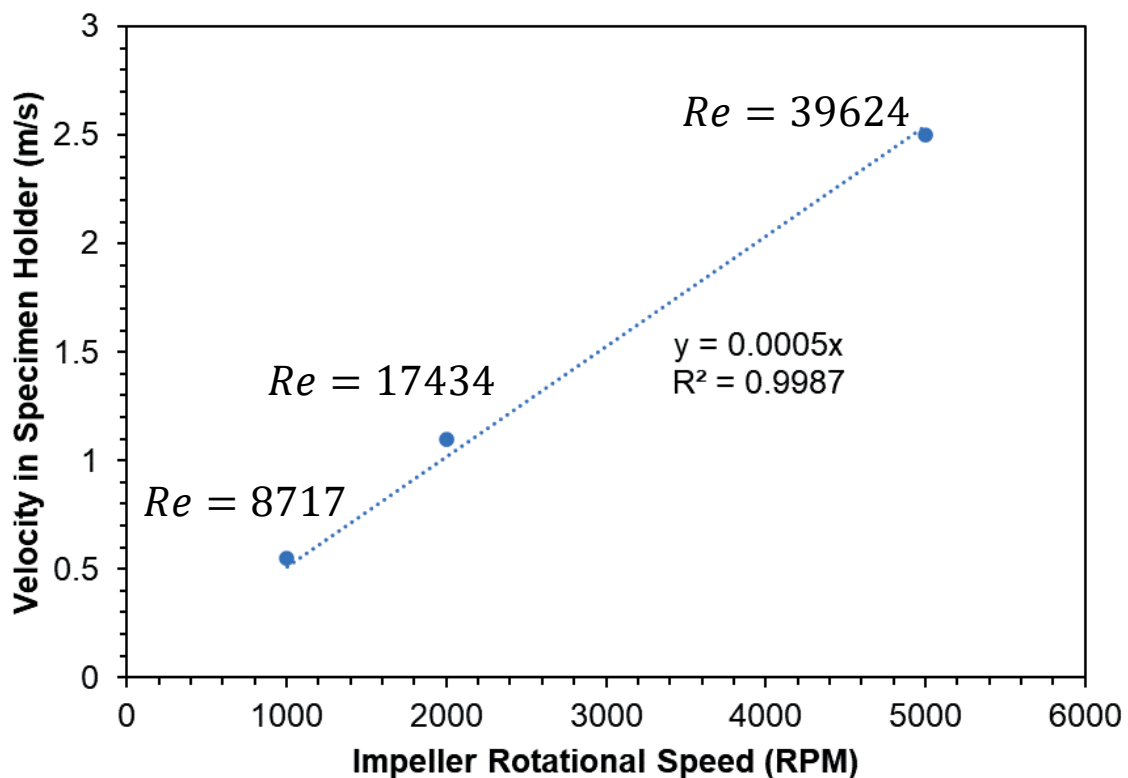


Figure 50. Effect of impeller rotational speed in preliminary model on velocity observed in specimen holder

## 8.2 Replication of Physical Prototype Model

Steady state simulations were performed for rotational rates of 1000 RPM, 2000 RPM, and 5000 RPM. This was done to showcase the difference impeller rotational rate, and therefore fluid velocity, makes on the velocity profile, turbulent kinetic energy, and  $y^+$  values in the glass cell. For most simulation results, a vertical cross section will be used to demonstrate the effect of the parameter of interest. Because the flowtube is expected to be axisymmetric, the vertical cross section will be considered an accurate representation of the system as a whole.

Simulation results showcase the velocity profiles represented by velocity vectors in a vertical cross section of the glass cell. The vertical cross-section will serve as a representation of the fluid motion within the glass cell. The turbulent kinetic energy will be shown as a vertical cross section of the glass cell. The turbulent kinetic energy is a measure of the turbulence present in the solution. The  $y^+$  value will be shown as a vertical cross section of the glass cell. These parameters are identical to those discussed for the preliminary simulation, but these simulations will introduce various factors to replicate the physical prototype, as discussed under Methodology. These features were implemented in the physical prototype and were intended to decrease or eliminate secondary motion within the specimen holder and within the bulk electrolyte solution. Additionally, the glass cell was expanded to 4 L volume in order to avoid a surface area to volume ratio limitation if three specimens were tested simultaneously. The following results are intended to demonstrate the anticipated hydrodynamics in a simulation as close as possible to the physical prototype.

### **8.2.1 1000 RPM**

Results for the 1000 RPM simulation are shown in Figure 51, Figure 52, Figure 53, and Figure 54 below.

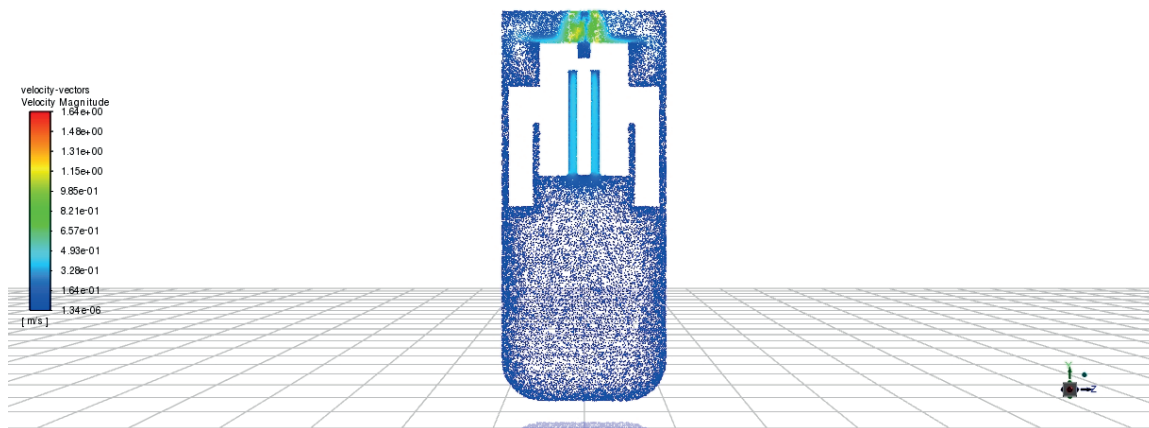


Figure 51. Velocity vectors in yz cross-section of physical prototype model at 1000 RPM impeller speed

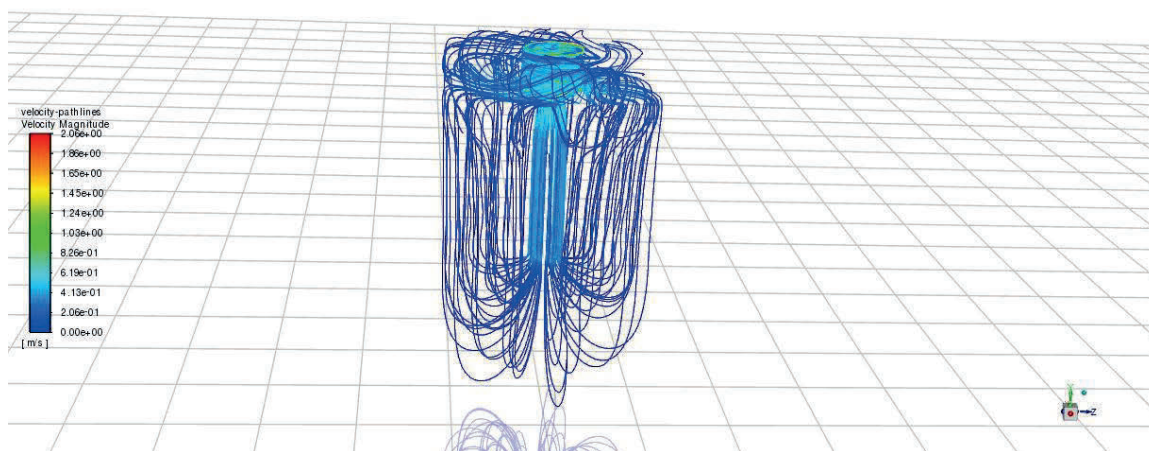


Figure 52. Velocity pathlines in yz cross-section of physical prototype model at 1000 RPM impeller speed

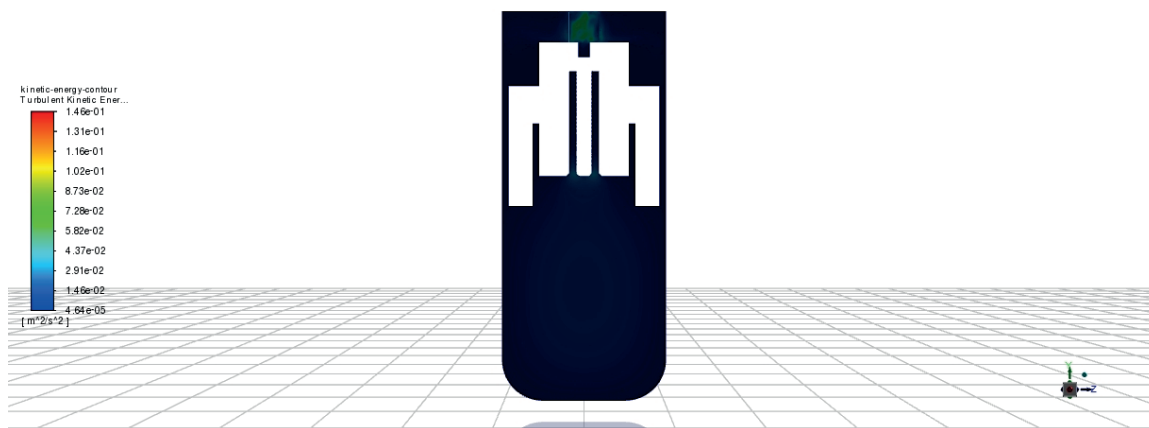


Figure 53. Turbulent kinetic energy contour in yz cross-section of physical prototype model at 1000 RPM impeller speed

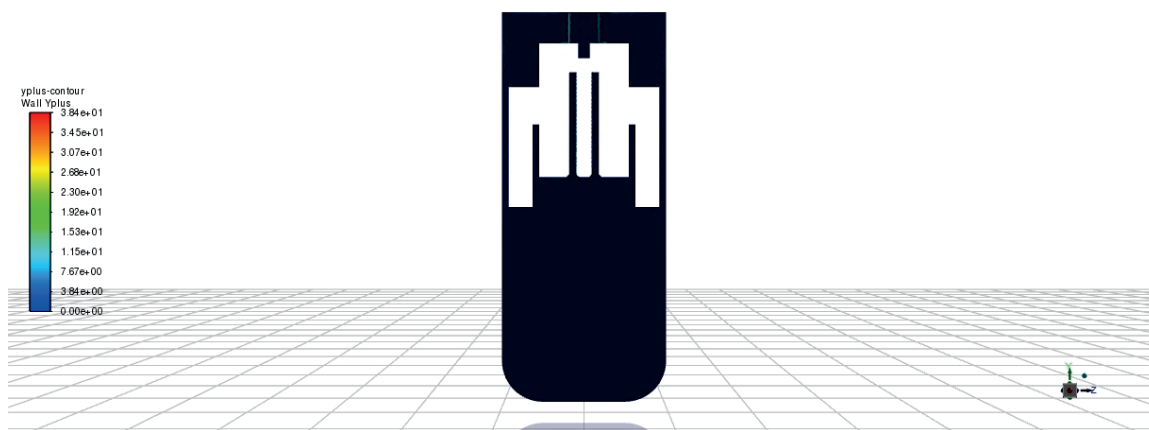


Figure 54.  $y^+$  contour in yz cross-section of physical prototype model at 1000 RPM impeller speed

Figure 51 and Figure 52 show the velocity profile at 1000 RPM in different styles. The velocity within the specimen holder was found to be approximately 0.394 m/s. Similar to the preliminary model, Figure 52 shows that the swirling motion is not present at steady state and 1000 RPM with the baffles and internal flow straightener present. This

simulation result appears to be very similar to what was observed at in the simulation without the external baffles, which implies that the external baffles do not significantly impact the flow pattern at 1000 RPM.

Figure 53 shows that the turbulent kinetic energy in the glass cell is at its greatest magnitude near the impeller. This is expected behavior because the impeller is a moving object that directly interferes with the fluid surrounding it. It should also be noted that there is a clear spike in turbulent kinetic energy near the entrance to the specimen holder. This spike is present despite the addition of the beveled edge and the bullnose edge being added to that opening. This shows that the addition of those edges did not significantly impact the turbulent kinetic energy at the entrance of the flowtube.

Figure 54 shows that the  $y^+$  values within the glass cell reach a maximum value of 38.4 for this simulation; this maximum is located at the impeller. There are other regional spikes in  $y^+$  values near the walls of the specimen holder and counter electrode similar to the preliminary model; these  $y^+$  values are also within the acceptable range of  $y^+$  values. Because the values of  $y^+$  near the walls of this system exist within the constraints outlined above, it can be concluded that the mesh sizing is sufficient for simulations performed at 1000 RPM.

### **8.2.2 2000 RPM**

Results for the 1000 RPM simulation are shown in Figure 55, Figure 56, Figure 57, and Figure 58 below.

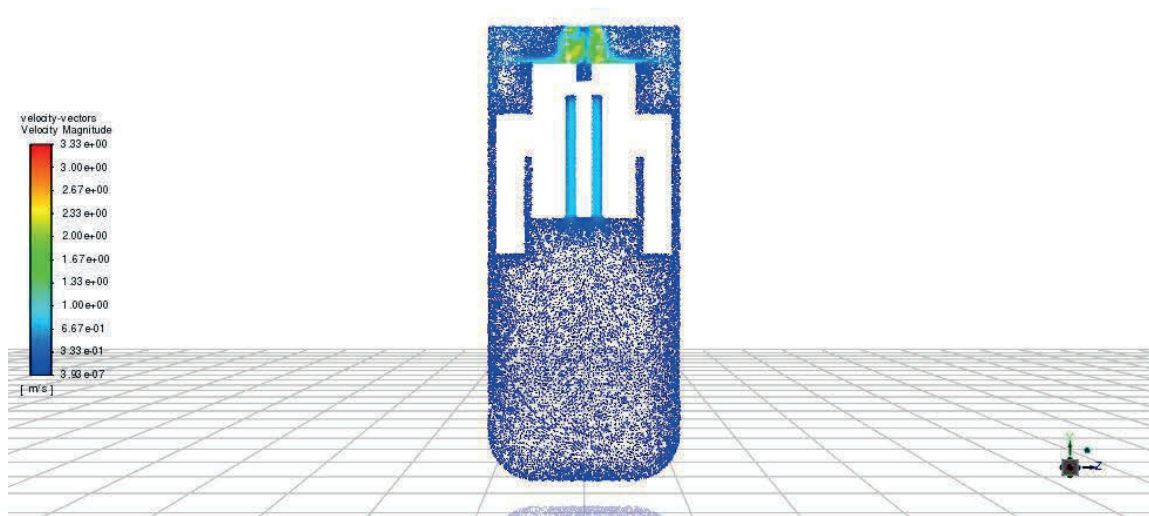


Figure 55. Velocity vectors in yz cross-section of physical prototype model at 2000 RPM  
impeller speed

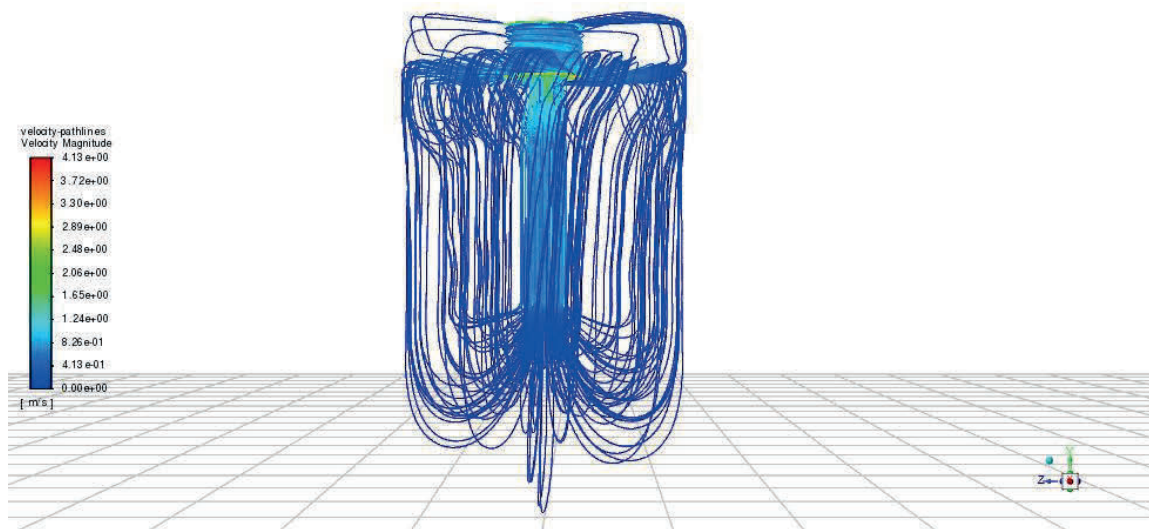


Figure 56. Velocity pathlines in yz cross-section of physical prototype model at 2000  
RPM impeller speed

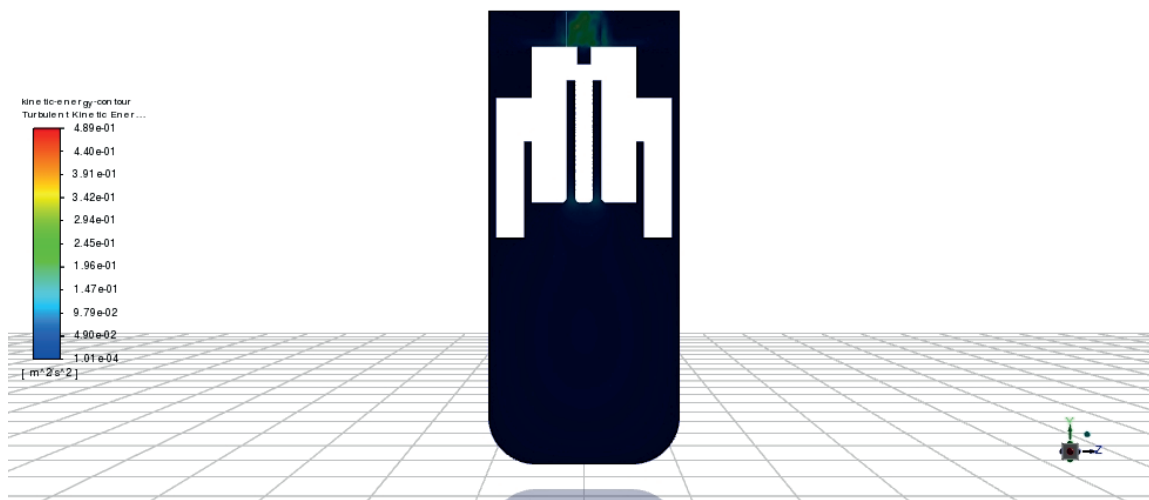


Figure 57. Turbulent kinetic energy contour in yz cross-section of physical prototype model at 2000 RPM impeller speed

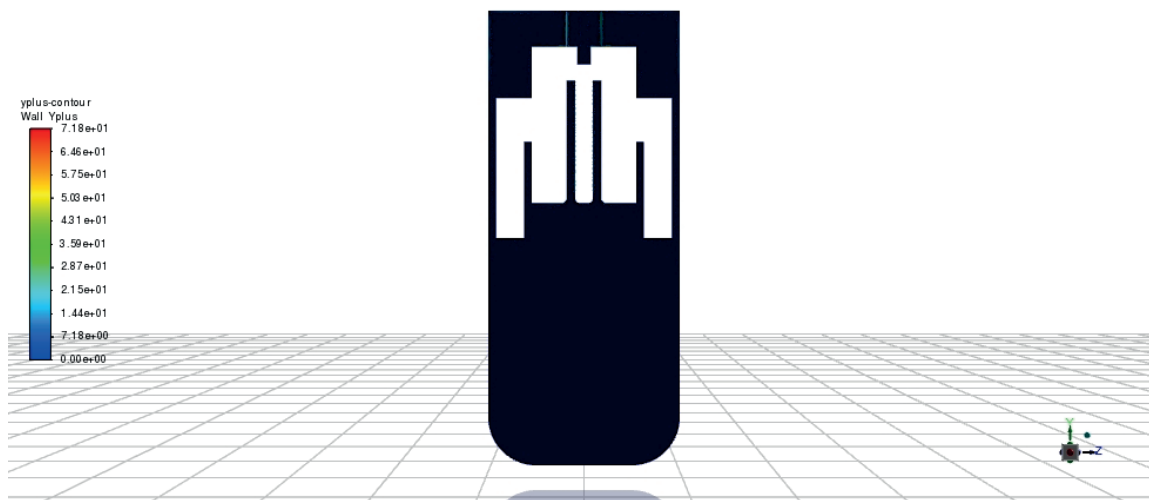


Figure 58.  $y^+$  contour in yz cross-section of physical prototype model at 2000 RPM impeller speed

Figure 55 and Figure 56 show the velocity profile at 2000 RPM in different styles. The velocity within the specimen holder was found to be approximately 0.800 m/s. This

simulation result appears to be very similar to what was observed at in the simulation without the external baffles, which implies that the external baffles do not significantly impact the flow pattern at 2000 RPM. Similar to the previous case, it appears the primary difference between the 1000 RPM and 2000 RPM trials is the superficial velocity of the fluid within the specimen holder.

Figure 57 shows that the turbulent kinetic energy in the glass cell at 2000 RPM impeller speed. There is an increased magnitude of turbulent kinetic energy when compared to the 1000 RPM simulation, but there is little difference beyond that. The same analysis applies.

Figure 58 shows that the  $y^+$  values within the glass cell reach a maximum value of 71.8 for this simulation; this maximum is located at the top of the flowtube at the boundary between the impeller fluid body and the bulk fluid. This is expected because of the turbulence caused by the impeller's rotation. The regional spikes in  $y^+$  values are also within the acceptable range of  $y^+$  values. Because the values of  $y^+$  near the walls of this system exist within the constraints outlined above, it can be concluded that the mesh sizing is sufficient for simulations performed at 2000 RPM.

### **8.2.3 5000 RPM**

Results for the 5000 RPM simulation are shown in Figure 59, Figure 60, Figure 61, and Figure 62 below.

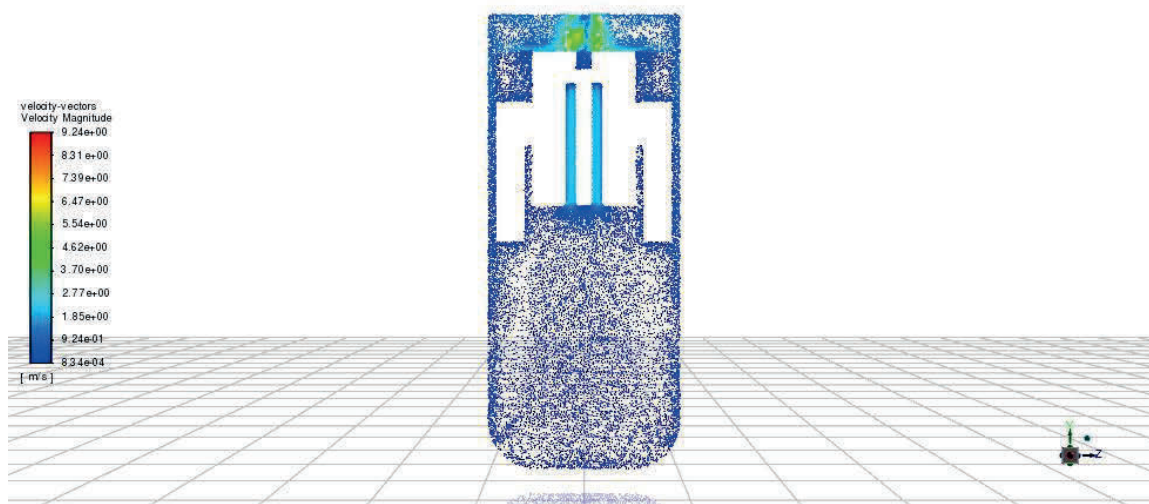


Figure 59. Velocity vectors in yz cross-section of physical prototype model at 5000 RPM  
impeller speed

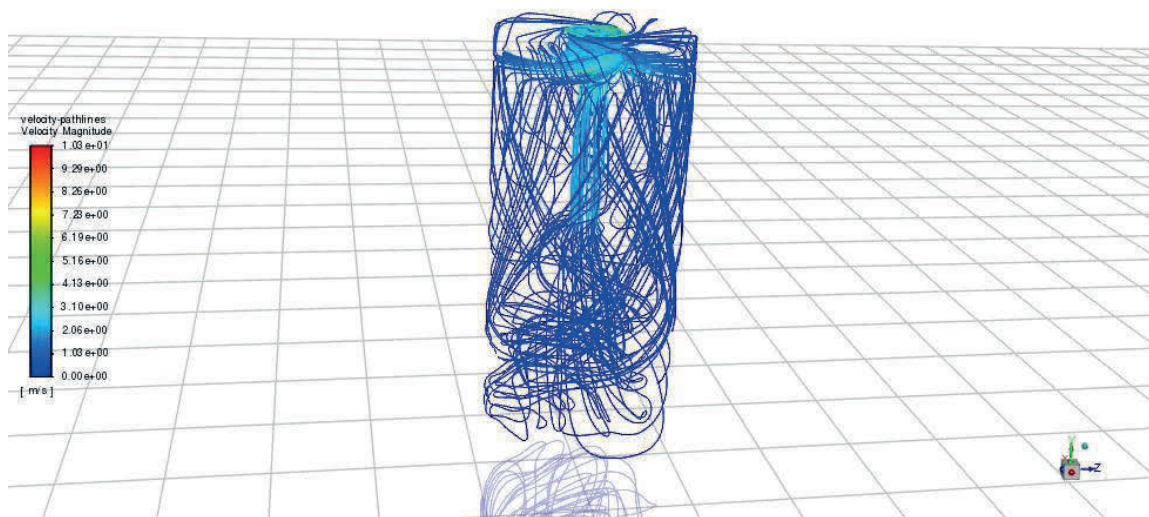


Figure 60. Velocity pathlines in yz cross-section of physical prototype model at 5000  
RPM impeller speed

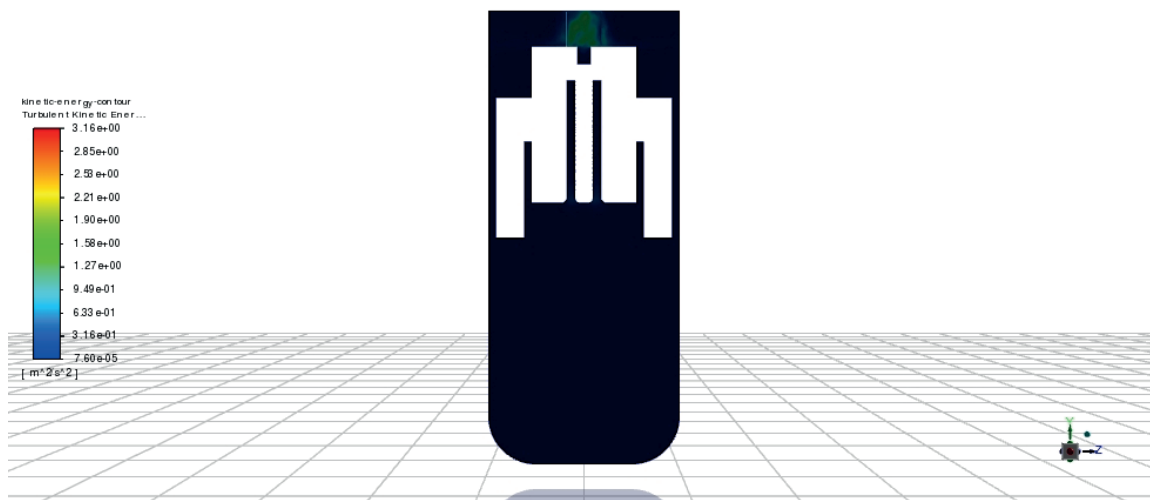


Figure 61. Turbulent kinetic energy contour in yz cross-section of physical prototype model at 5000 RPM impeller speed

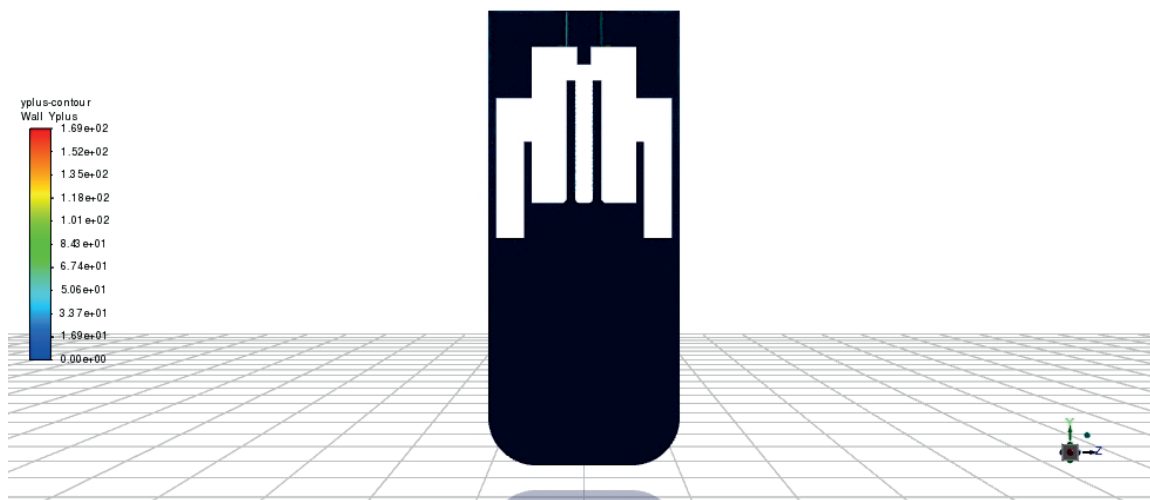


Figure 62.  $y^+$  contour in yz cross-section of physical prototype model at 5000 RPM impeller speed

Figure 59 and Figure 60 show the velocity profile at 5000 RPM from different angles and vantage points. Figure 60 shows a very similar story to the previous rotational

speeds; the magnitude of fluid velocity is now higher, and the secondary motion region near the top of the glass cell is even more pronounced. The velocity within the specimen holder was found to be approximately 2.217 m/s. Figure 59 and Figure 60 show that there is a significant difference in the flow pattern, just like the previous simulation. In the 5000 RPM simulation, there is a very clear swirling motion present in the bulk fluid. This bulk fluid motion appears to be decreased with the addition of the internal flow straightener. In spite of the secondary fluid motion within the bulk electrolyte solution, the swirling motion previously identified in the specimen holder appears to not be present. This indicates that the physical prototype design is able to sufficiently mitigate the effect of the secondary fluid motion on the specimen holder region. In physical experimentation, the baffles appeared to significantly decrease the secondary motion within the glass cell. This appears to have been verified through this CFD simulation.

Figure 61 shows the turbulent kinetic energy in the glass cell with a rotational rate of 5000 RPM. There is a further increased magnitude of turbulent kinetic energy when compared to the previous simulations. At first glance, it appears that there is less turbulence at the entrance to the specimen holder as well. However, closer inspection reveals that the turbulent kinetic energy near the impeller is now so large that the scale is skewed in such a way that makes the entrance to the specimen holder appear less significant.

Figure 62 shows that the  $y^+$  values within the glass cell reach a maximum value of 169 for this simulation; this maximum is located at the boundary between the impeller fluid body and the bulk solution at the surface where the top of the glass cell is located.

Because the  $y^+$  values near the impeller and near the top of the glass cell exceed the threshold for acceptable  $y^+$  values, it can be concluded that the mesh is not able to accurately predict fluid motion near the impeller or near the top of the glass cell at 5000 RPM. In order to overcome this, the mesh will have to be finer near those regions. That said, the  $y^+$  values appeared to be within an acceptable range near the walls of the specimen holder. This indicates that the fluid flow is sufficiently modeled at those points, which are the region of interest. In future trials, the inflation could be implemented at the boundary between the impeller enclosure fluid body and the bulk solution fluid body. This should smooth out any issues arising from a difference in mesh sizing. However, the  $y^+$  values within the specimen holder seem to indicate that this simulation is able to adequately model the hydrodynamics of the system within the region of interest.

It should also be noted that specimen placement is of concern within this design. The current prototype contains specimens starting approximately 0.125 inches above the inlet of the flowtube and ending directly below the internal flow straightener. It appears that at the bottom of the flowtube, the flow is fully developed approximately 0.2 inches above the bottom of the flowtube. This was determined by observing the superficial fluid velocity at various points along the y-axis and determining where it stabilized along that line. A similar analysis was performed at the top of the flowtube, where the flow is interrupted by the flow straightener. It was determined that the flow ceases to be fully developed approximately 0.4 inches from the top of the specimen holder. This analysis was performed for the 5000 RPM trial as the larger superficial fluid velocity will cause the entry and exit regions where the flow is not fully developed to be larger than the

regions in 1000 RPM or 2000 RPM trials. For design purposes, it is necessary to design for the most restrictive case, which would be in the 5000 RPM trial. For future design prototypes, this analysis has concluded that the specimen holder should be decreased in size and modified so that the top specimen is no less than 0.4 inches from the top of the specimen holder and the bottom specimen is no less than 0.2 inches from the inlet.

### **8.3 Removal of Internal Flow Straightener**

Steady state simulations were performed for rotational rates of 1000 RPM, 2000 RPM, and 5000 RPM. Similar to the previous simulation, the intention is to showcase the difference that rotational rate, and therefore fluid velocity, makes on the velocity profile, turbulent kinetic energy, and  $y^+$  values in the glass cell. For most simulation results, a vertical cross section will be used to demonstrate the effect of the parameter of interest. Because the flowtube is expected to be axisymmetric, the vertical cross-section will be considered an accurate representation of the system as a whole. Simulation results showcase the parameters of interest in the same manner as discussed above in the previous simulations. The following results are intended simulate how the hydrodynamics would change if the internal flow straightener was removed from the physical prototype.

#### **8.3.1 1000 RPM**

Results for the 1000 RPM simulation are shown in Figure 63, Figure 64, Figure 65, and Figure 66 below.



Figure 63. Velocity vectors in yz cross-section of model without internal flow straightener at 1000 RPM impeller speed

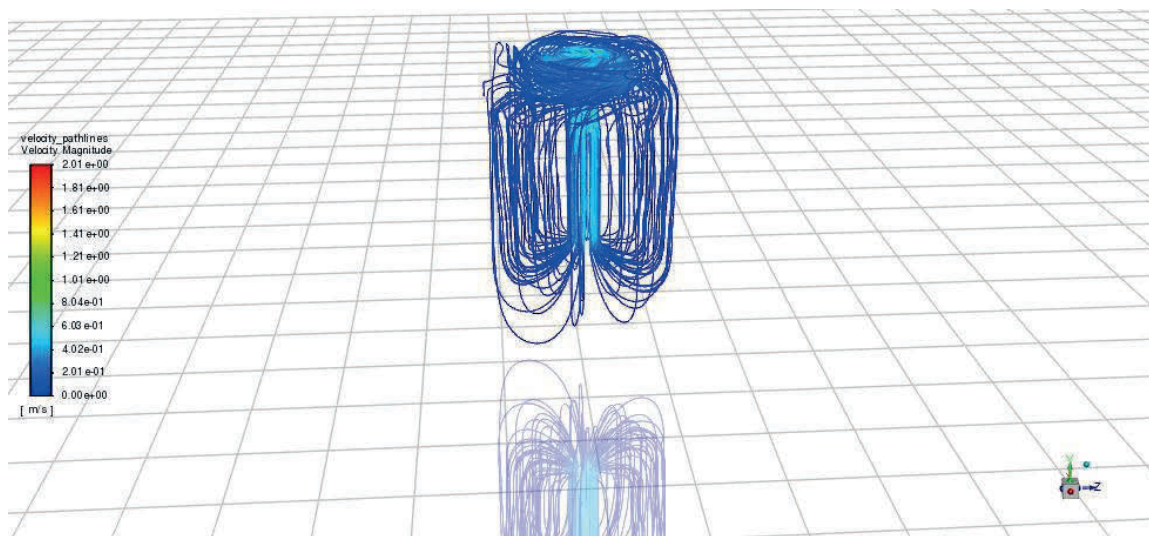


Figure 64. Velocity pathlines in yz cross-section of model without internal flow straightener at 1000 RPM impeller speed

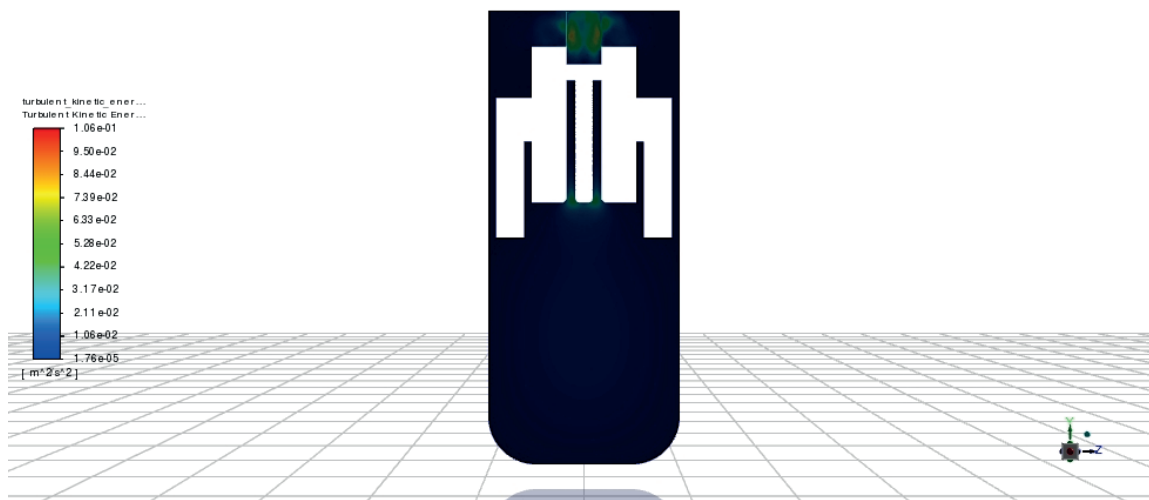


Figure 65. Turbulent kinetic energy contour in yz cross-section of model without internal flow straightener at 1000 RPM impeller speed

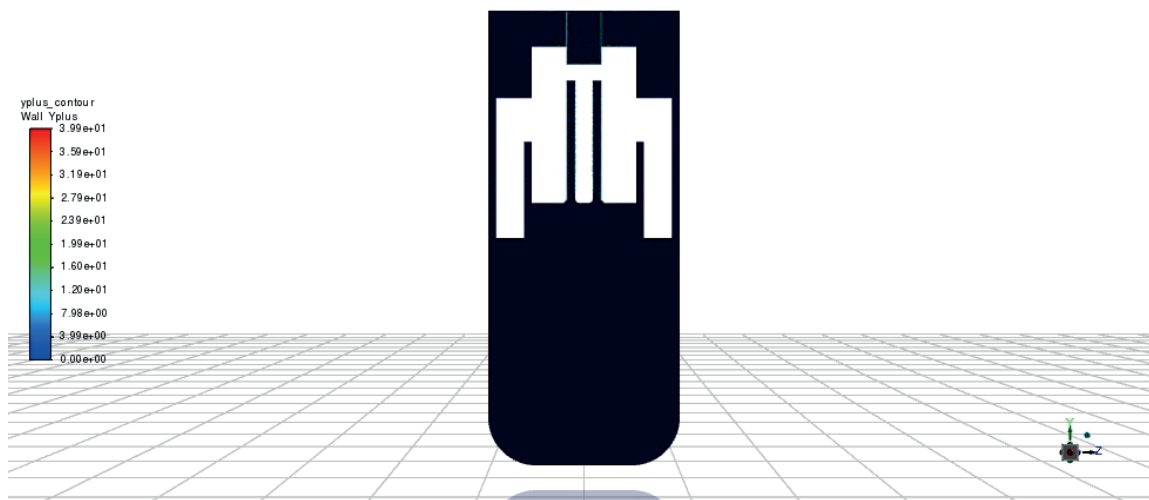


Figure 66.  $y^+$  contour in yz cross-section of model without internal flow straightener at 1000 RPM impeller speed

Figure 63 and Figure 64 show the velocity profile at 1000 RPM in different styles. The velocity within the specimen holder was found to be approximately 0.493 m/s. This

simulation result appears to be very similar to what was observed in the previous simulation, which implies that the internal flow straighteners do not significantly impact the flow pattern at 1000 RPM.

Figure 65 shows that the turbulent kinetic energy in the glass cell is at its greatest magnitude near the impeller. This is expected behavior and is discussed more thoroughly in the discussion of previous models. The internal flow straightener does not appear to cause a significant impact on the turbulent kinetic energy modeled in this system.

Figure 66 shows that the  $y^+$  values within the glass cell reach a maximum value of 39.9 for this simulation; this maximum is located at the impeller. The regional spikes in  $y^+$  values are also within the acceptable range of  $y^+$  values. Because the values of  $y^+$  near the walls of this system exist within the constraints outlined above, it can be concluded that the mesh sizing is sufficient for simulations performed at 1000 RPM.

### **8.3.2 2000 RPM**

Results for the 2000 RPM simulation are shown in Figure 67, Figure 68, Figure 69, and Figure 70 below.

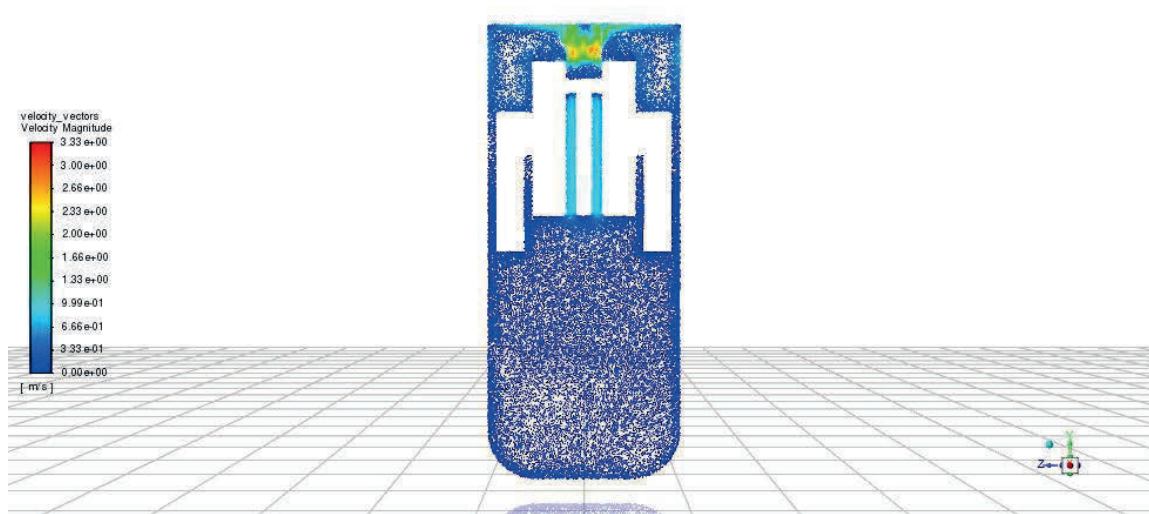


Figure 67. Velocity vectors in yz cross-section of model without internal flow straightener at 2000 RPM impeller speed

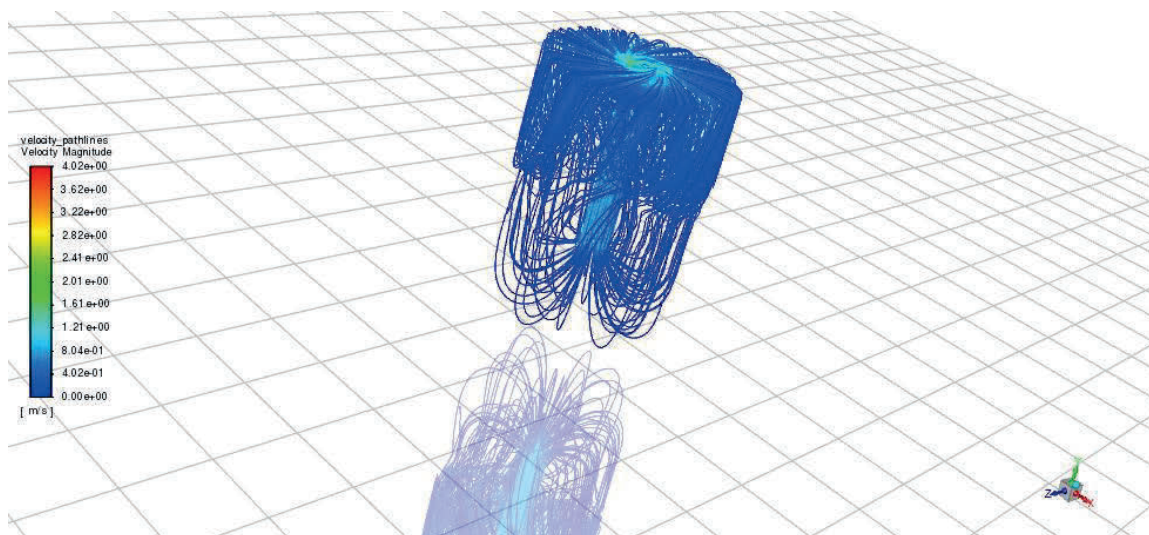


Figure 68. Velocity pathlines in yz cross-section of model without internal flow straightener at 2000 RPM impeller speed

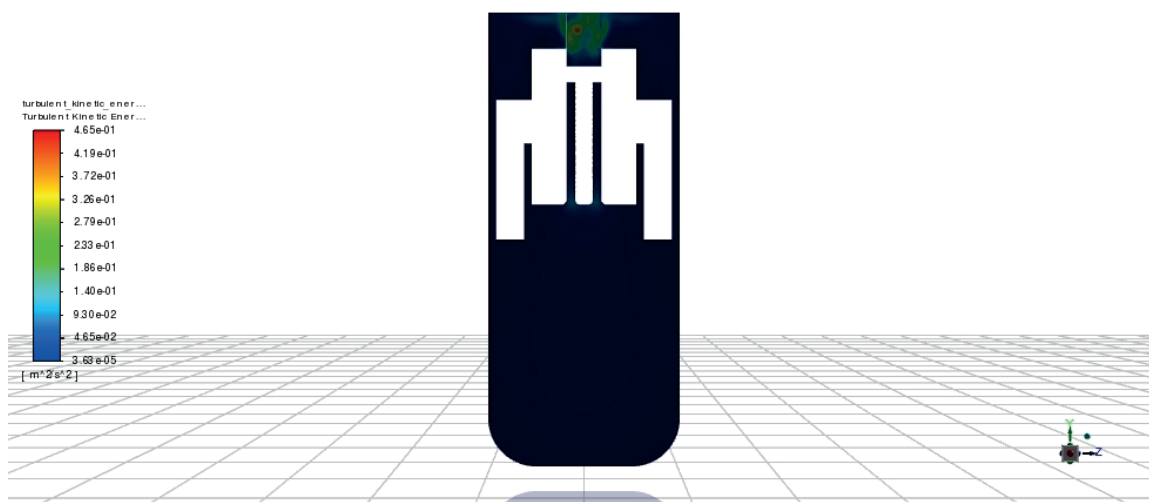


Figure 69. Turbulent kinetic energy contour in yz cross-section of model without internal flow straightener at 2000 RPM impeller speed

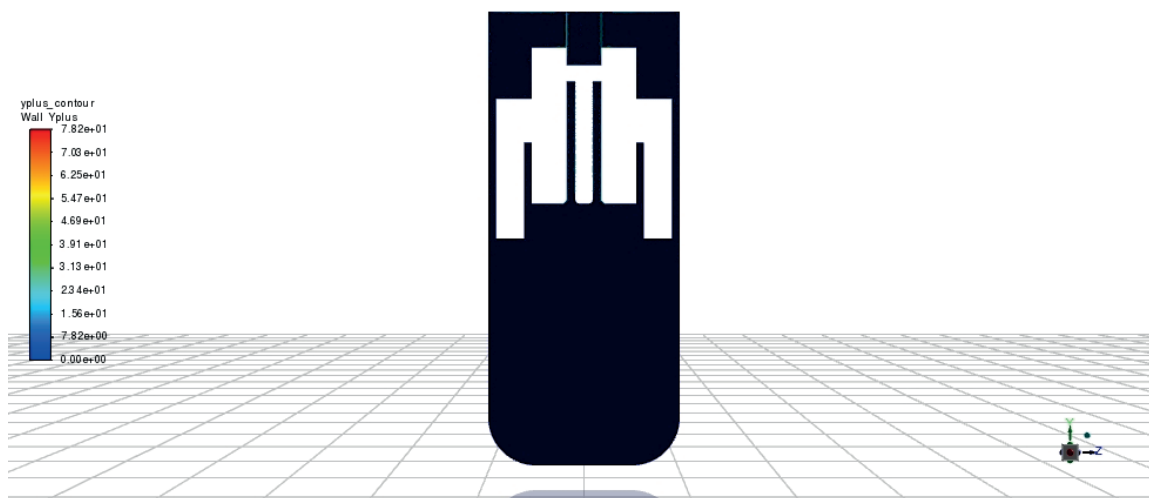


Figure 70.  $y^+$  contour in yz cross-section of model without internal flow straightener at 2000 RPM impeller speed

Figure 67 and Figure 68 show the velocity profile at 2000 RPM in different styles. The velocity within the specimen holder was found to be approximately 0.899 m/s. This simulation result appears to be very similar to what was observed at in the previous simulation, which implies that the internal flow straightener does not significantly impact the flow pattern at 2000 RPM.

Figure 69 shows the turbulent kinetic energy in the glass cell at 2000 RPM impeller speed. There is an increased magnitude of turbulent kinetic energy when compared to the 1000 RPM simulation, but there is little difference beyond that. The same analysis applies as described above. The internal flow straightener does not appear to cause a significant impact on the turbulent kinetic energy modeled in this system.

Figure 70 shows that the  $y^+$  values within the glass cell reach a maximum value of 78.2 for this simulation; this maximum is located at the top of the flowtube at the boundary between the impeller fluid body and the bulk fluid. The regional spikes in  $y^+$  values are also within the acceptable range of  $y^+$  values. Because the values of  $y^+$  of this system exist within the constraints outlined above, it can be concluded that the mesh sizing is sufficient for simulations performed at 2000 RPM.

### **8.3.3 5000 RPM**

Results for the 5000 RPM simulation are shown in Figure 71, Figure 72, Figure 73, and Figure 74 below.



Figure 71. Velocity vectors in yz cross-section of model without internal flow straightener at 5000 RPM impeller speed

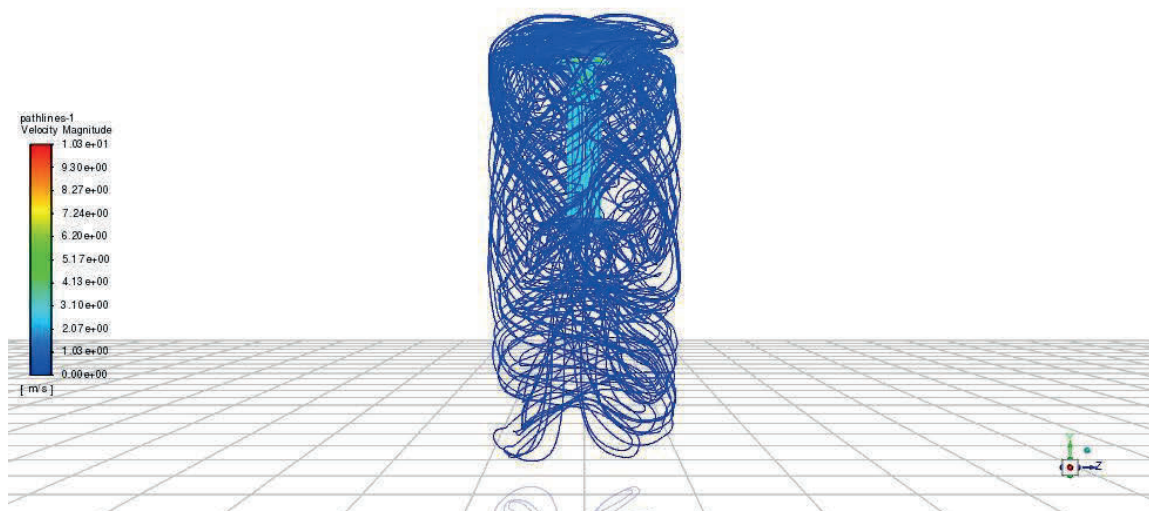


Figure 72. Velocity pathlines in yz cross-section of model without internal flow straightener at 5000 RPM impeller speed

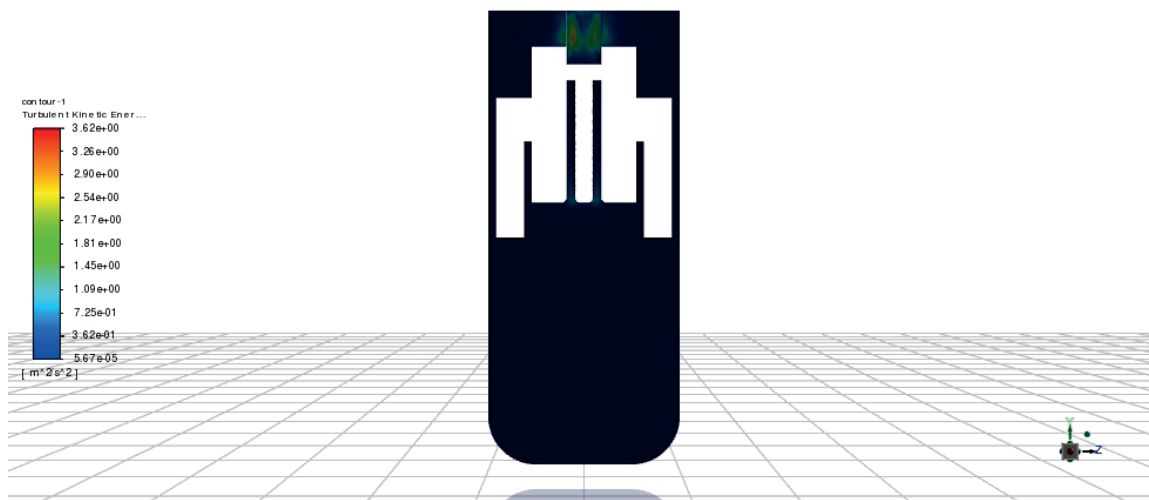


Figure 73. Turbulent kinetic energy contour in yz cross-section of model without internal flow straightener at 5000 RPM impeller speed

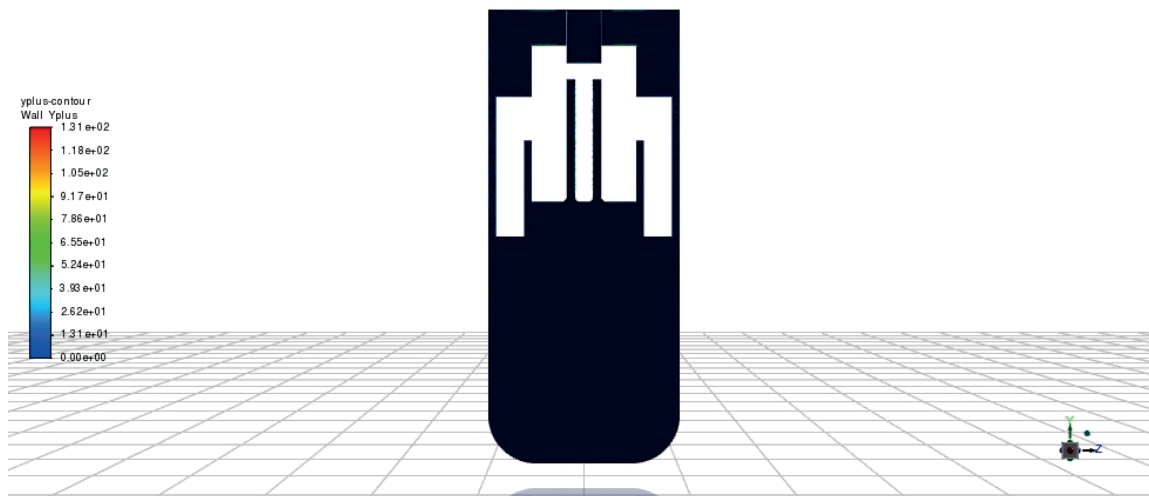


Figure 74.  $y^+$  contour in yz cross-section of model without internal flow straightener at 5000 RPM impeller speed

Figure 71 and Figure 72 show the velocity profile at 5000 RPM from different angles and vantage points. Figure 72 shows a very similar story to the previous rotational speeds; the magnitude of fluid velocity is now higher, and the secondary motion region near the top of the glass cell is even more pronounced. The velocity within the specimen holder was found to be approximately 2.36 m/s. Figure 71 and Figure 72 show that there is a significant difference in the flow pattern as shown in the model showing the replication of the physical prototype; the swirling motion previously identified in the specimen holder appears to not be present. This appears to indicate that the removal of the internal flow straighteners does not significantly impact the flow pattern within the specimen holder at any of the rotational speeds tested.

Figure 73 shows the turbulent kinetic energy in the glass cell with a rotational rate of 5000 RPM. The same analysis applies to this model as the previous model at 5000 RPM. The internal flow straightener does not appear to cause a significant impact on the turbulent kinetic energy modeled in this system.

Figure 74 shows that the  $y^+$  values within the glass cell reach a maximum value of 131 for this simulation; this maximum is located at the boundary between the impeller fluid body and the bulk solution at the surface where the top of the glass cell is located. Because the  $y^+$  values near the impeller and near the top of the glass cell exceed the threshold for acceptable  $y^+$  values, it can be concluded that the mesh is not able to accurately predict fluid motion near the impeller or near the top of the glass cell at 5000 RPM. In order to overcome this, the mesh will have to be finer near those regions. That said, the  $y^+$  values appeared to be within an acceptable range near the walls of the

specimen holder. This indicates that the fluid flow is sufficiently modeled at those points, which are the region of interest. In future trials, the inflation could be implemented at the boundary between the impeller enclosure fluid body and the bulk solution fluid body. This should smooth out any issues arising from a difference in mesh sizing. However, this model should still sufficiently model the hydrodynamic properties of the system within the region of interest despite this potential shortcoming.

Similar to above, an analysis was performed to determine optimal specimen location within the specimen holder for this trial. The development of the flow at the bottom of the flowtube appeared unaffected by the removal of the internal flow straightener. As in the simulation for the replication of the physical prototype, the flow appeared to be fully developed approximately 0.2 inches from the bottom of the flowtube. It was also determined that the removal of the internal flow straightener did not significantly impact the flow at the top of the specimen holder either. The flow appeared to be fully developed approximately 0.4 inches from the top of the specimen holder. Therefore, it can be concluded that the removal of the internal flow straightener does not impact the design considerations for the optimal specimen location within the flowtube.

#### **8.4 Reduced Counter Electrode Diameter**

Similar to previous simulations, steady state simulations were performed for rotational rates of 1000 RPM, 2000 RPM, and 5000 RPM. This was done to showcase the difference impeller rotational rate, and therefore fluid velocity, makes on the velocity profile, turbulent kinetic energy, and  $y^+$  values in the glass cell. Similar to the previous simulations, the intention is to showcase the difference that rotational rate, and therefore

fluid velocity, makes on the velocity profile, turbulent kinetic energy, and  $y^+$  values in the glass cell. As above, a vertical cross section will be used to demonstrate the effect of the parameter of interest due to the axisymmetric nature of the flowtube system. Simulation results showcase the parameters of interest in the same manner as discussed above in the previous simulations. The following results are intended to demonstrate the anticipated hydrodynamics in a simulation taking into account a design case where the diameter of the central counter electrode is reduced by half.

#### 8.4.1 1000 RPM

Results for the 1000 RPM simulation are shown in Figure 75, Figure 76, Figure 77, and Figure 78 below.

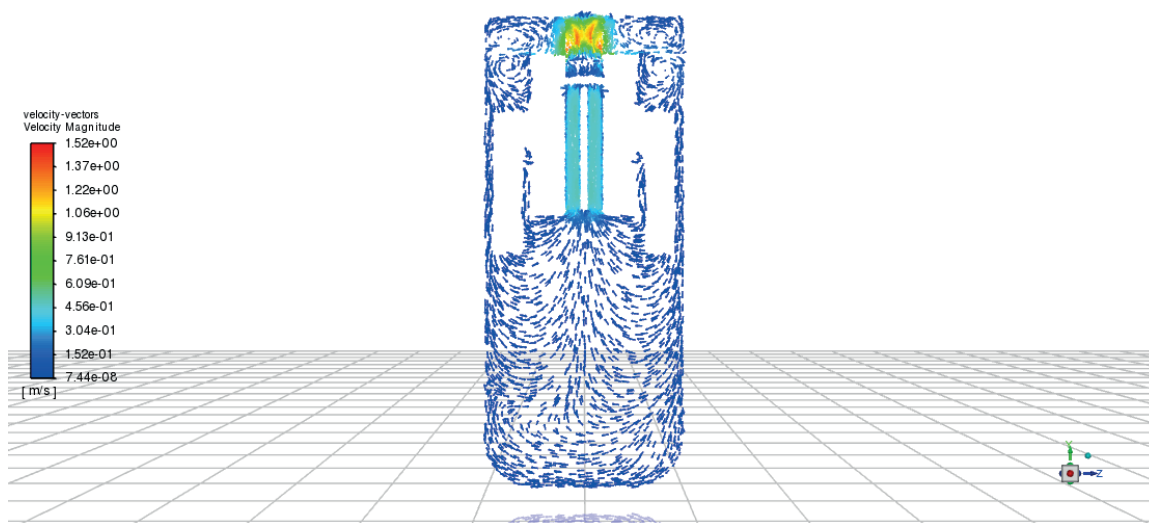


Figure 75. Velocity vectors in yz cross-section of smaller counter electrode model at 1000 RPM impeller speed

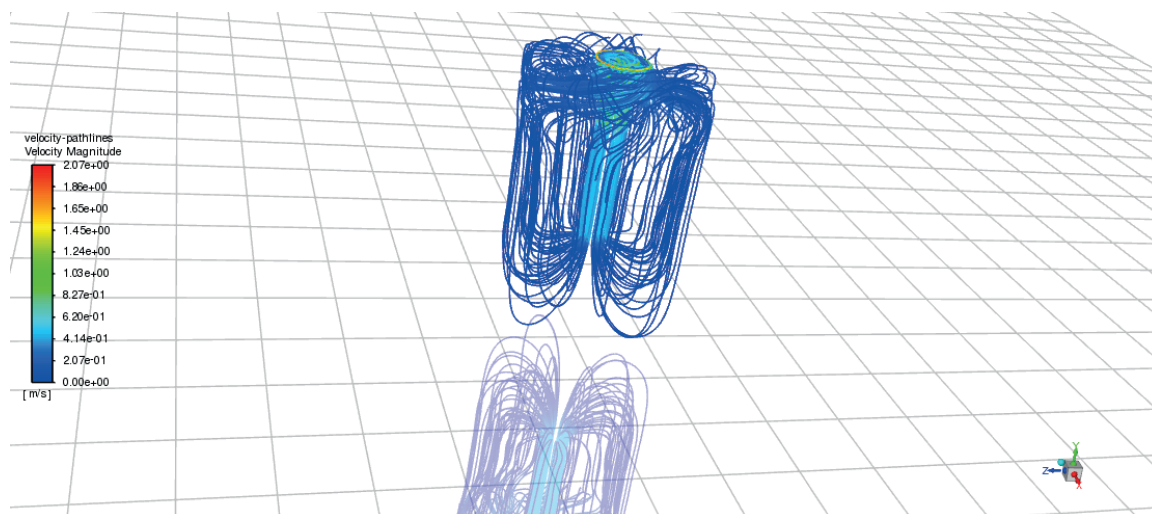


Figure 76. Velocity pathlines in yz cross-section of smaller counter electrode model at 1000 RPM impeller speed

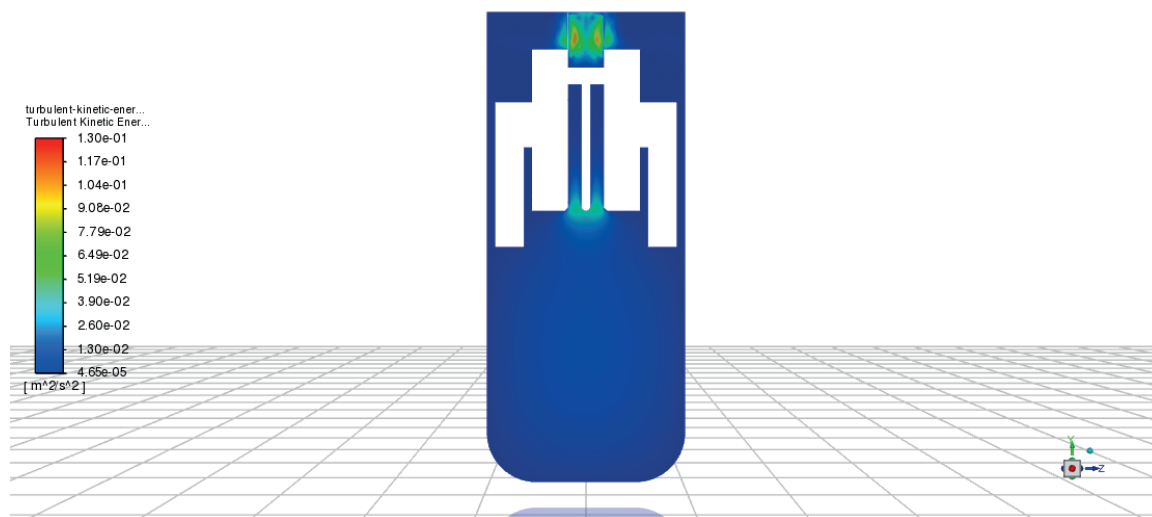


Figure 77. Turbulent kinetic energy contour in yz cross-section of smaller counter electrode model at 1000 RPM impeller speed

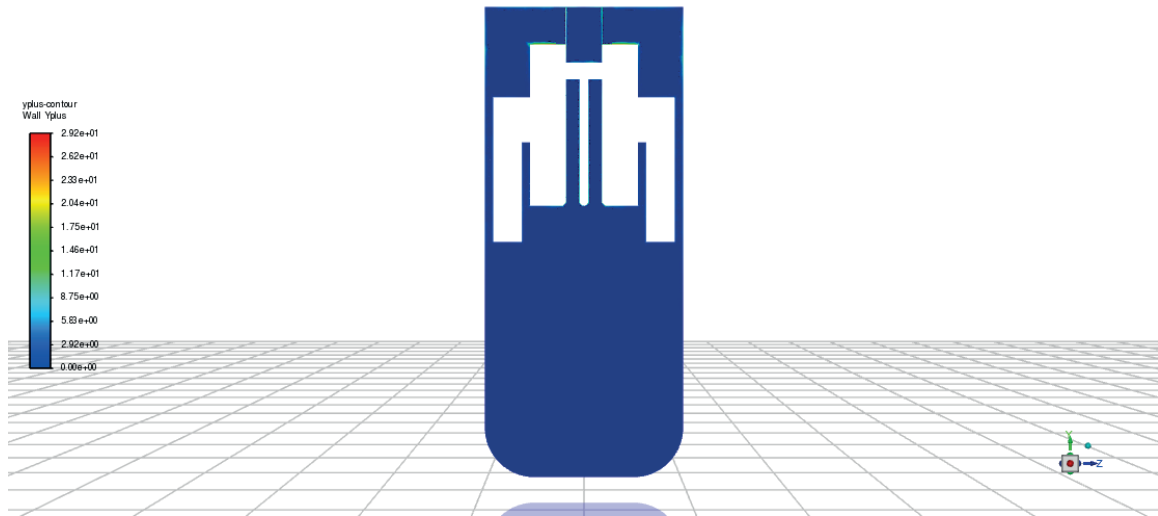


Figure 78.  $y^+$  contour in yz cross-section of smaller counter electrode model at 1000 RPM impeller speed

Figures show the velocity profile at 1000 RPM in different styles. The velocity within the specimen holder was found to be approximately 0.487 m/s.

Figure shows that the turbulent kinetic energy in the glass cell is at its greatest magnitude near the impeller. This is expected behavior because the impeller is a moving object that directly interferes with the fluid surrounding it. It should also be noted that there is a clear spike in turbulent kinetic energy near the entrance to the specimen holder. This spike is present despite the addition of the beveled edge and the bullnose edge being added to that opening. This shows that the addition of those edges did not significantly impact the turbulent kinetic energy at the entrance of the flowtube.

Figure shows that the  $y^+$  values within the glass cell reach a maximum value of 29.1 for this simulation; this maximum is located at the impeller. This is expected because of the turbulence caused by the impeller's rotation. There are other regional

spikes in  $y^+$  values near the walls of the specimen holder and counter electrode; these  $y^+$  values are also within the acceptable range of  $y^+$  values. Because the values of  $y^+$  near the walls of this system exist within the constraints outlined above, it can be concluded that the mesh sizing is sufficient for simulations performed at 1000 RPM.

#### 8.4.2 2000 RPM

Results for the 2000 RPM simulation are shown in Figure 79, Figure 80, Figure 81, and Figure 82 below.

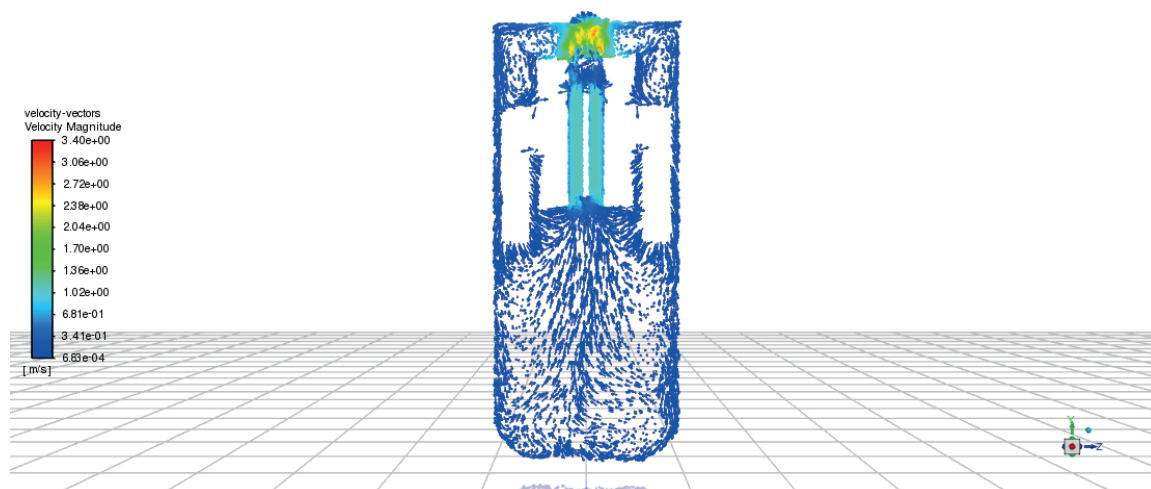


Figure 79. Velocity vectors in yz cross-section of smaller counter electrode model at 2000 RPM impeller speed

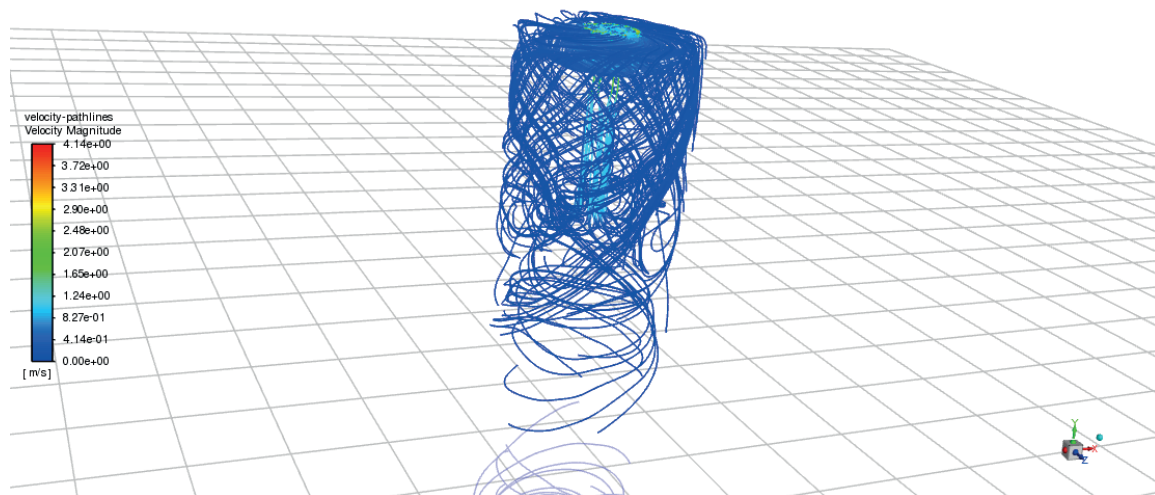


Figure 80. Velocity pathlines in yz cross-section of smaller counter electrode model at 2000 RPM impeller speed

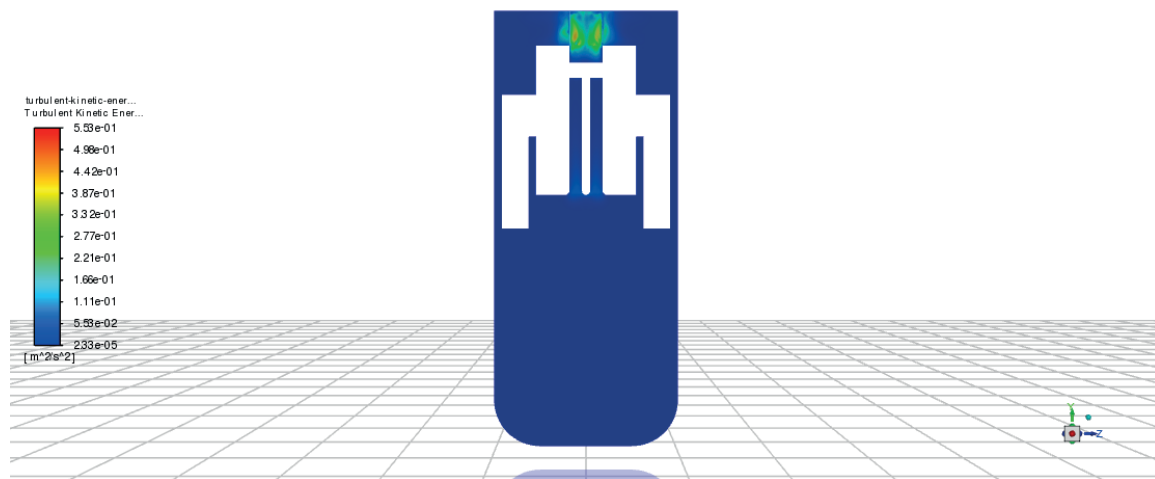


Figure 81. Turbulent kinetic energy contour in yz cross-section of smaller counter electrode model at 2000 RPM impeller speed

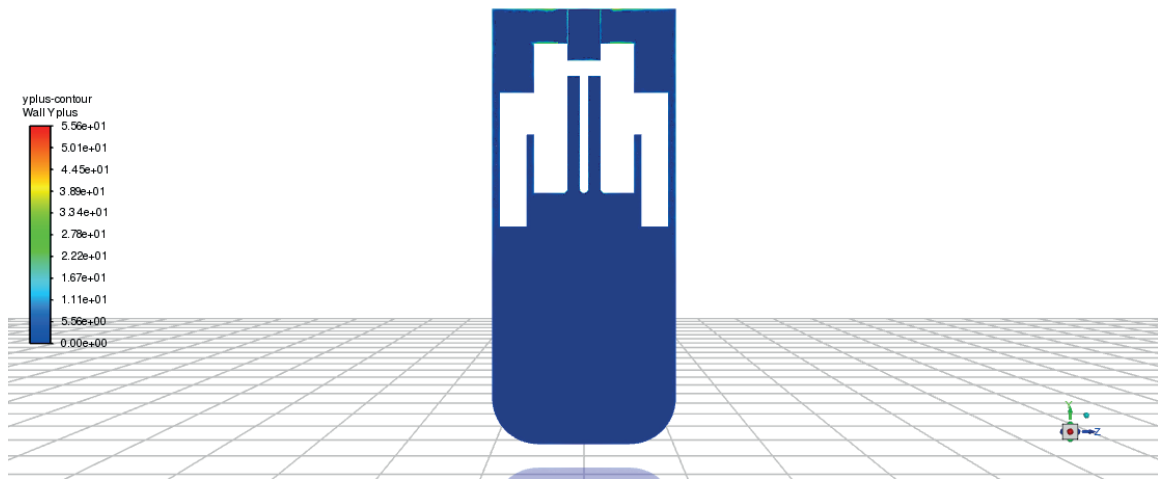


Figure 82.  $y^+$  contour in yz cross-section of smaller counter electrode model at 2000 RPM impeller speed

Figures show the velocity profile at 2000 RPM in different styles. The velocity within the specimen holder was found to be approximately 1.089 m/s.

Figure shows that the turbulent kinetic energy in the glass cell is at its greatest magnitude near the impeller. This is expected behavior because the impeller is a moving object that directly interferes with the fluid surrounding it. It should also be noted that there is a clear spike in turbulent kinetic energy near the entrance to the specimen holder. This spike is present despite the addition of the beveled edge and the bullnose edge being added to that opening. This shows that the addition of those edges did not significantly impact the turbulent kinetic energy at the entrance of the flowtube.

Figure shows that the  $y^+$  values within the glass cell reach a maximum value of 55.3 for this simulation; this maximum is located at the impeller. This is expected because of the turbulence caused by the impeller's rotation. There are other regional

spikes in  $y^+$  values near the walls of the specimen holder and counter electrode; these  $y^+$  values are also within the acceptable range of  $y^+$  values. Because the values of  $y^+$  near the walls of this system exist within the constraints outlined above, it can be concluded that the mesh sizing is sufficient for simulations performed at 2000 RPM.

#### 8.4.3 5000 RPM

Results for the 5000 RPM simulation are shown in Figure 83, Figure 84, Figure 85, and Figure 86 below.

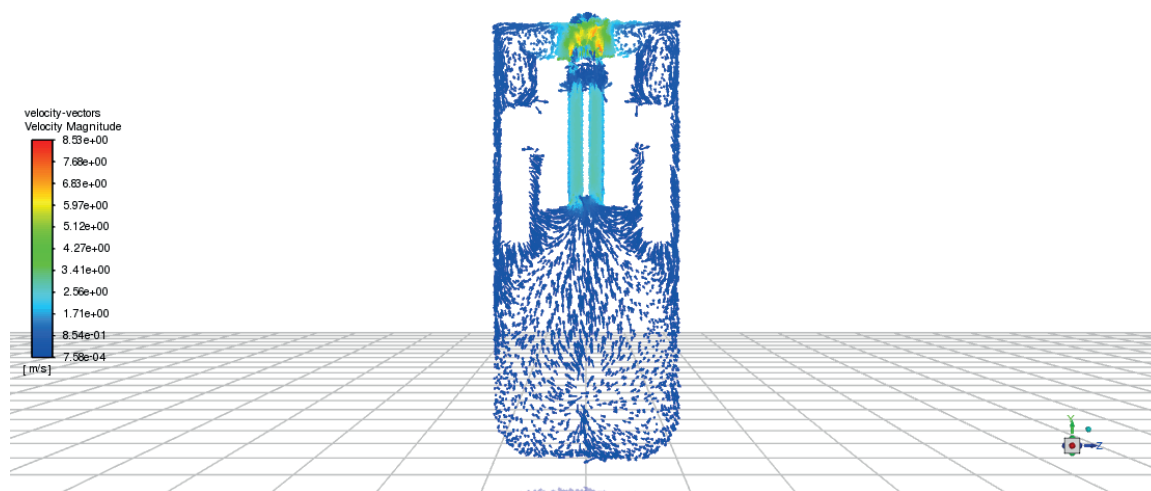


Figure 83. Velocity vectors in yz cross-section of smaller counter electrode model at 5000 RPM impeller speed

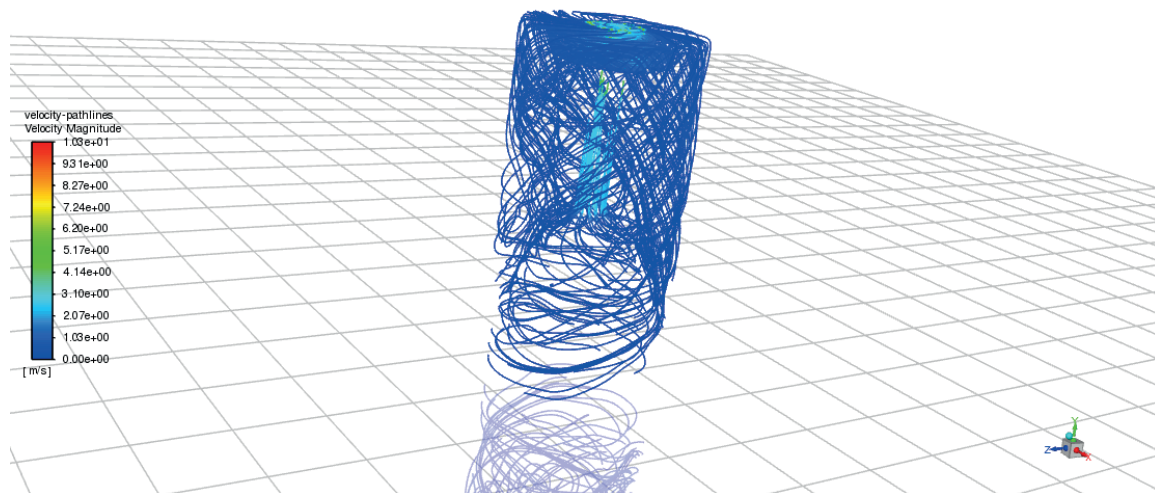


Figure 84. Velocity pathlines in yz cross-section of smaller counter electrode model at 5000 RPM impeller speed

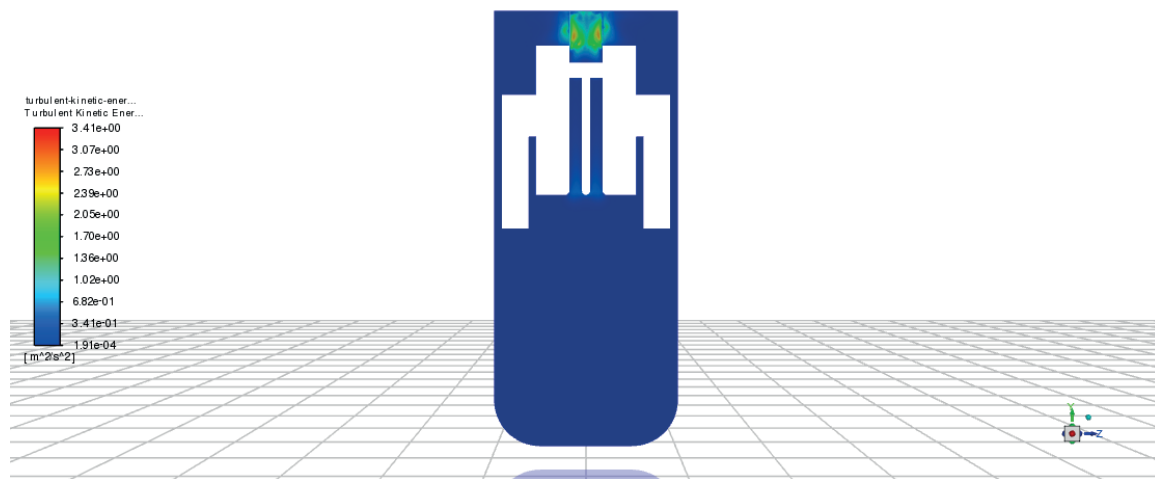


Figure 85. Turbulent kinetic energy contour in yz cross-section of smaller counter electrode model at 5000 RPM impeller speed

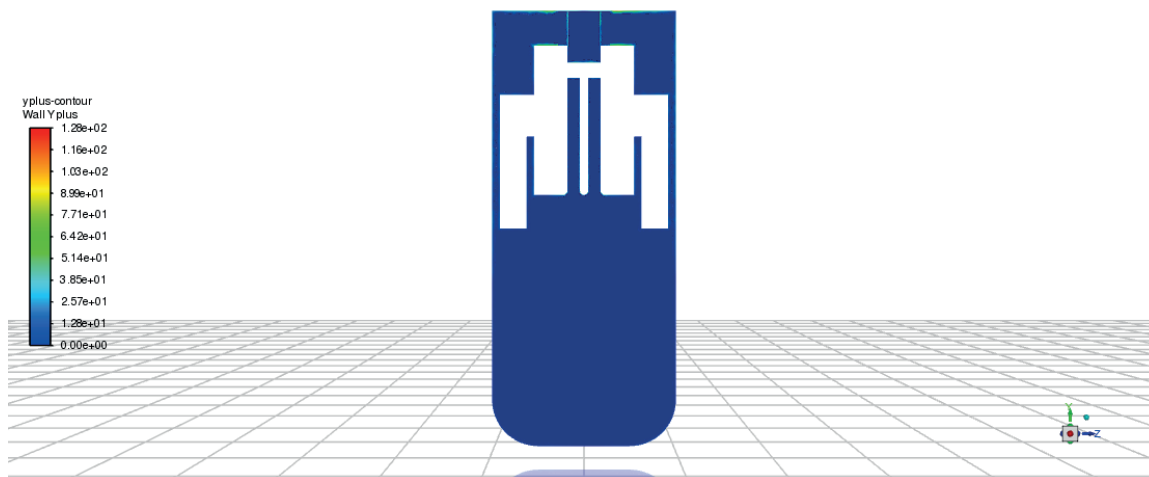


Figure 86.  $y^+$  contour in yz cross-section of smaller counter electrode model at 5000 RPM impeller speed

Figure 83 and Figure 84 show the velocity profile at 5000 RPM in different styles. The velocity within the specimen holder was found to be approximately 2.816 m/s.

Figure 85 shows that the turbulent kinetic energy in the glass cell is at its greatest magnitude near the impeller. This is expected behavior because the impeller is a moving object that directly interferes with the fluid surrounding it. It should also be noted that there is a clear spike in turbulent kinetic energy near the entrance to the specimen holder. This spike is present despite the addition of the beveled edge and the bullnose edge being added to that opening. This shows that the addition of those edges did not significantly impact the turbulent kinetic energy at the entrance of the flowtube.

Figure 86 shows that the  $y^+$  values within the glass cell reach a maximum value of 116.6 for this simulation; this maximum is located at the impeller. This is expected because of the turbulence caused by the impeller's rotation. Because the  $y^+$  values near

the impeller and near the top of the glass cell exceed the threshold for acceptable  $y^+$  values, it can be concluded that the mesh is not able to accurately predict fluid motion near the impeller or near the top of the glass cell at 5000 RPM. Similar to other 5000 RPM simulations, the  $y^+$  values within the specimen holder are within the acceptable range. The same analysis applies as in previous 5000 RPM simulations.

Similar to above, an analysis was performed to determine optimal specimen location within the specimen holder for this trial. The development of the flow at the bottom of the flowtube was impacted by the reduction in size of the central counter electrode. In this simulation, the flow appeared to be fully developed approximately 0.125 inches from the bottom of the flowtube, directly after the beveled edge ends at the entrance to the flowtube. It was also determined that the reduction in size of the central counter electrode did not significantly impact the flow at the top of the specimen holder either. The flow appeared to be fully developed approximately 0.4 inches from the top of the specimen holder. Therefore, it can be concluded that the removal of the reduction in the size of the central counter electrode may impact the design considerations for the optimal specimen location within the flowtube. By reducing the size of the central counter electrode, the specimens could be located closer to the entrance to the specimen holder.

After all simulations are completed for the flowtube, the superficial fluid velocity within the specimen holder can be compared between simulated conditions. This comparison allows for a clearer view of the differences in hydrodynamics within the region of interest as the design conditions are altered. Specifically, this shows that the

superficial fluid velocity increases with simpler design conditions while maintaining a constant impeller rotational speed, as anticipated. It is important to understand this observation when creating a new physical prototype as the superficial fluid velocity within the specimen holder is the variable of interest within the system. These results are summarized in Table 17 below. The superficial fluid velocity results were used in order to determine the Reynolds number for the flow through the flowtube sample holder at each specified rotational speed and design consideration using Equation (28). This analysis confirmed that the flow through the flowtube specimen holder was fully developed turbulent flow for all simulated parameters, as the Reynolds number for all cases was above 4000. It should be noted that the change in design parameters did impact the minimum velocity for fully developed turbulent flow. These minimum rotational speeds are tabulated in Table 17 below. It appears that reducing the counter electrode size has the largest impact on the minimum rotational speed allowable while maintaining fully developed turbulent flow. For any considered design considerations, this analysis should be performed to ensure that the rotational rate of the impeller does not cause a flow through the specimen holder that is not fully developed turbulent flow.

Table 17. Comparison of superficial velocity between various flowtube design considerations

	Preliminary Model	Replication of Physical Prototype	No Internal Flow Straighteners	Smaller Counter Electrode
Glass Cell Size	2 L	4 L	4 L	4 L
External Baffles	No	Yes	Yes	Yes
Internal Flow Straighteners	No	Yes	No	No
Counter Electrode Size	0.50 inch	0.50 inch	0.50 inch	0.25 inch
1000 RPM	0.550 m/s	0.394 m/s	0.493 m/s	0.487 m/s
2000 RPM	1.100 m/s	0.800 m/s	0.899 m/s	1.089 m/s
5000 RPM	2.500 m/s	2.217 m/s	2.360 m/s	2.816 m/s
Minimum Rotational Speed for Turbulent Flow	495 RPM	578 RPM	536 RPM	301 RPM

## Chapter 9: Results and Discussion for CFD Model of RDE

### 9.1 Mass Transfer CFD Model for RDE Simulation

Simulations for the mass transfer of H<sup>+</sup> ions to the surface of the RDE were performed for RDE rotational speeds of 250, 500, 1000, 2000, 4000, and 8000 RPM. This was done in order to replicate experimental conditions and achieve a representative model of the simulated mass transfer boundary layer thickness. The flow fields for the RDE simulation are shown in Figure 87 below. The flow fields indicate that, as expected, the RDE shaft is rotating and causing bulk fluid motion within the glass cell. This bulk fluid motion causes mixing to occur, which brings aqueous species to the RDE surface, where the mass transfer takes place.

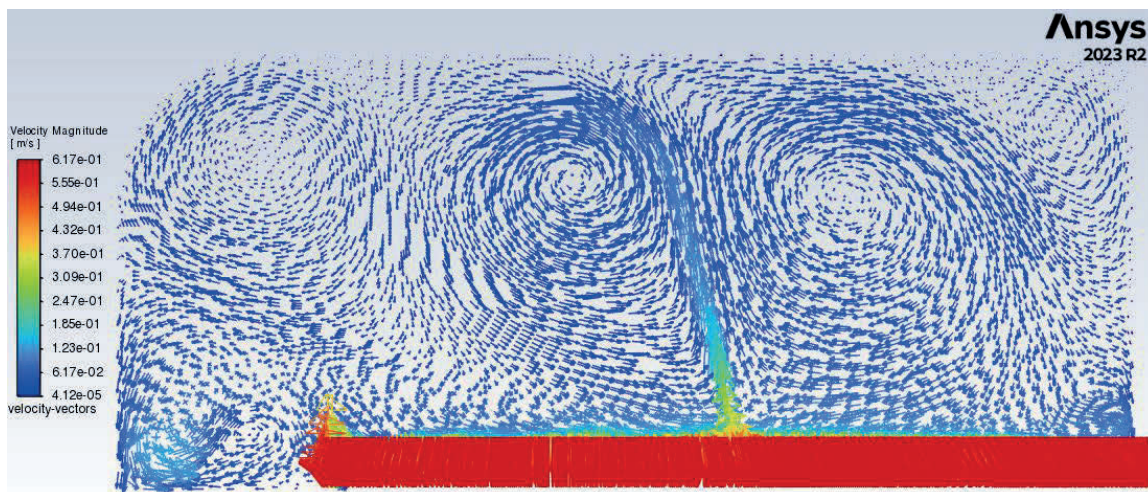


Figure 87. Velocity Vectors in RDE Simulation at 1000 RPM

For this analysis, the concentration profile was analyzed 1 mm above the centerline as shown in Figure 88 below. This analysis was performed for each rotational speed in

order to determine the mass transfer boundary layer thickness. The bulk fluid  $H^+$  concentration is 0.0001 M, as the pH of the solution was set to 4. In order to determine the mass transfer boundary layer thickness, a straight line was extrapolated from the linear region of the concentration profile nearest the RDE surface. The point at which the line intersects with the bulk solution concentration indicates the mass transfer boundary layer thickness. In Figure 88, this is noted as a red dotted line.

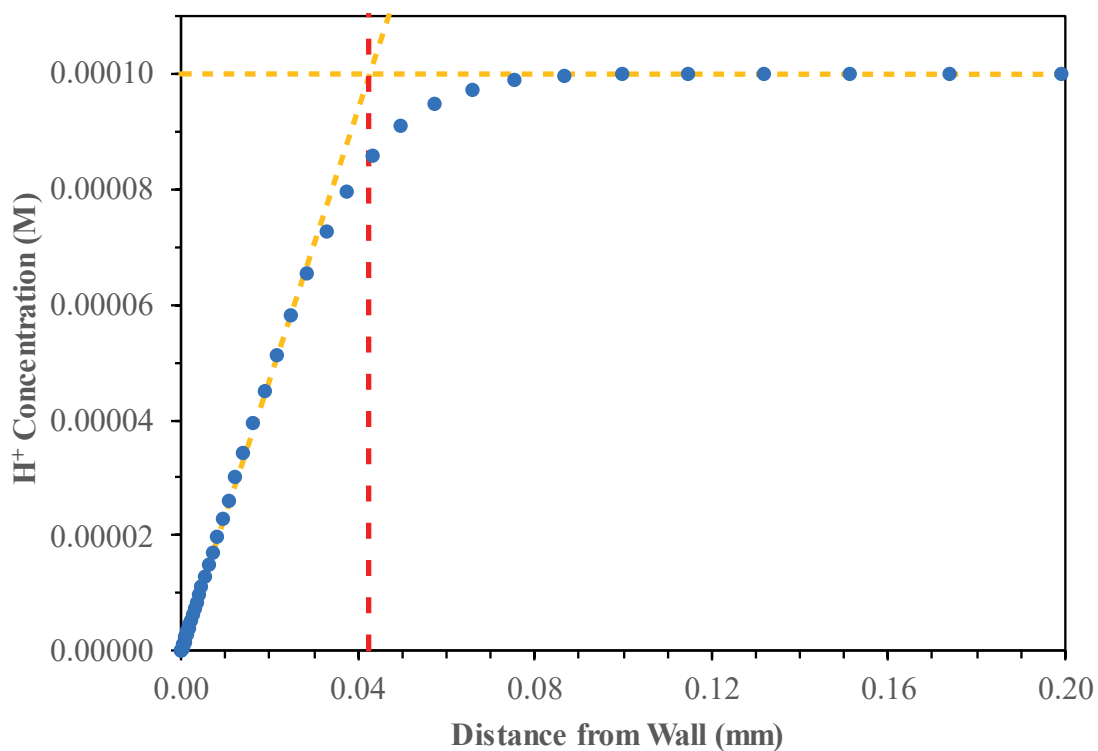


Figure 88.  $H^+$  Concentration profile 1 mm above centerline starting at RDE surface for 1000 RPM trial

The mass transfer boundary layer thickness results are shown in Figure 89 below. This figure shows that the simulated results follow the same trend as expected from the theoretical correlation from Equation (18). For nearly all analyzed rotational speeds, the simulated mass transfer boundary layer thickness is within 20% of the theoretical mass transfer boundary layer thickness. Due to this similarity, it can be concluded that the CFD simulated results sufficiently model the mass transfer of an RDE. This indicates that if more complex simulations are performed, such as a corrosion simulation, then the mass transfer portion of the simulation should not introduce significant error into the corrosion simulation.

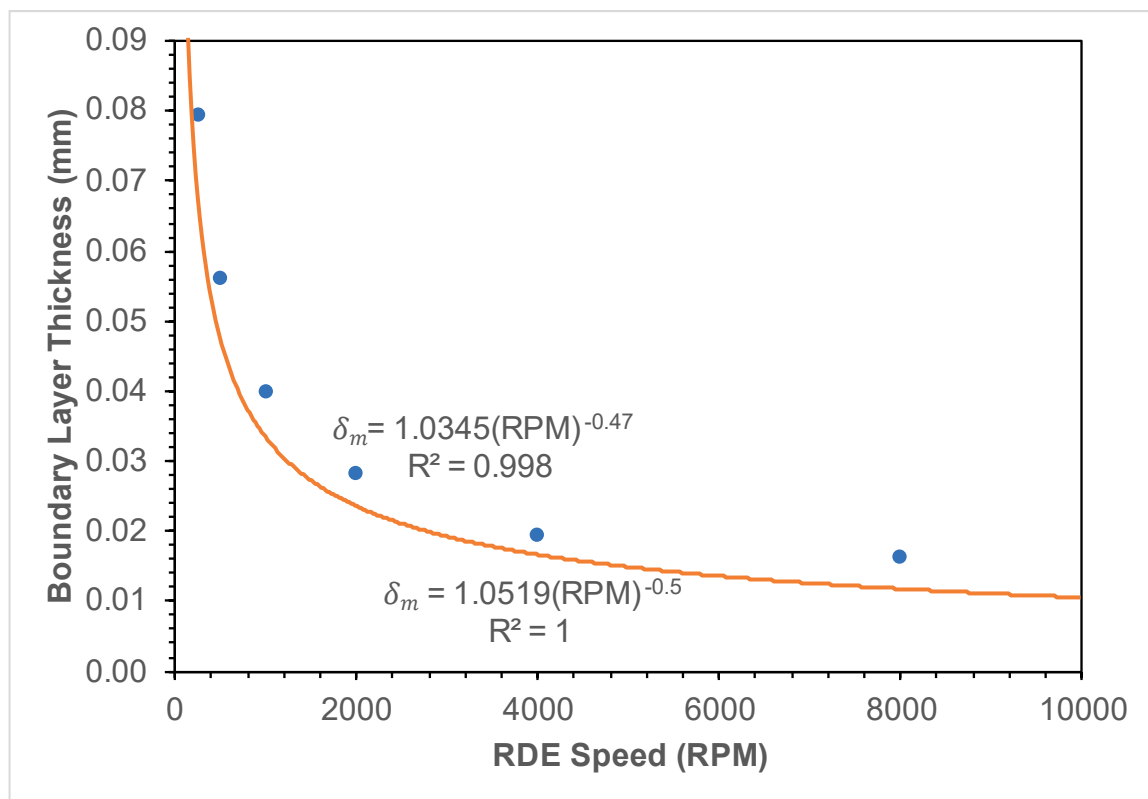


Figure 89. Comparison of simulated mass transfer boundary layer thickness to theoretical correlation

## Chapter 10: Conclusions and Future Work

The focus of this research has been to investigate the design considerations pertaining to the development of the flowtube apparatus for corrosion experimentation within a glass cell or autoclave. Over the course of the research, the following tasks were accomplished:

- Verified mass transfer correlation for ferricyanide/ferrocyanide solution proposed by Silverman using RCE equipment
- Conducted baseline corrosion experiments using 1018 mild steel RCE specimens and validated results using FREECORP™
- Conducted baseline corrosion experiments using an X65 mild steel RDE specimen and validated results using FREECORP™
- Conducted CFD simulations of flowtube apparatus using Ansys Fluent to explore design considerations for future prototype versions
- Conducted CFD simulations of rotating disk electrodes in order to form comparison of mass transfer to the literature correlation

The results of these experiments and simulations have been discussed above in order to determine their validity. Many of the baseline experiments offered valuable experience in learning how to perform electrochemical analyses for corrosion experimentation. The CFD simulations allowed for fine analysis of the effects of various design considerations without the need to develop a physical prototype in order to do so. For example, the simulations performed appear to indicate that the internal flow straightener does not

significantly impact the flow within the specimen holder of the flowtube, as long as the external baffles are present.

In future work, further design considerations for the flowtube should be considered. The simulations described above were restricted in scope to the previously developed prototype. However, future simulations will be able to incorporate further design considerations being implemented in the next prototype version. Based on the simulations performed, it has been concluded that the next prototype should include external baffles to mitigate secondary fluid motion within the glass cell and specifically inside the specimen holder. It was also concluded that the optimal location for electrochemical specimens is between 0.4 inches from the top of the specimen holder and 0.2 inches from the bottom of the specimen holder. Furthermore, experimentation will need to be performed on the physical prototype to verify the superficial fluid velocity within the specimen holder. The simulations indicated that differences in the design of the flowtube caused changes in the velocity of fluid within the specimen holder. This finding is significant because the previously used flow rate calibration rig detailed in Appendix A: did not incorporate the external baffles. Additionally, flowtube design considerations, such as reducing the size of the central counter electrode, could impact the optimal location for specimens within the specimen holder. It would be worthwhile to investigate how close the measured flowrate is within the calibration rig when compared to a glass cell or autoclave. Designing the flowtube with the capability to measure flow rate directly within the glass cell would be advantageous. It was also found that the internal flow straightener does not seem to significantly impact the flow within the specimen holder.

Previous design suggestions discussed placing internal flow straighteners at both the top and the bottom of the flowtube in order to mitigate secondary fluid motion in that region. However, it has now been determined that the external baffles should be sufficient in reducing the secondary motion. As such, future designs should incorporate the external baffles, possibly as a permanent structure rather than the current design, which is removable. In addition, future models may be able to incorporate the gas cap within the CFD simulations. Multiphase flow is a notable problem observed within the prototype flowtube design while it was in use. It would be desirable to determine if design considerations, such as moving the flowtube further down into the electrolyte solution, may aid in mitigating multiphase flow within the testing apparatus.

In addition to flowtube design considerations based on hydrodynamics, future work should incorporate corrosion simulations in order to verify the effect of design considerations on the measured corrosion. In order to make these simulations, the ability for Ansys Fluent to accurately predict corrosion in similar environments must be validated. In order to build confidence in the models, RDE corrosion simulations should be performed and validated. As discussed in Chapter 9:, the lack of ability to perform these simulations appears to be rooted in underlying problems with the way in which Ansys Fluent calculates the hydrodynamics within the RDE system. Once these issues are identified and rectified, the corrosion simulations in an RDE system can be performed and validated.

## Chapter 11: References

1. Nikitina, V. Charge transfer processes in the course of metal-ion electrochemical intercalation. *Current Opinion in Electrochemistry*, **2020**, 19, 71-77.  
<https://doi.org/10.1016/j.coelec.2019.10.006>
2. E. McCafferty. Introduction To Corrosion Science, Springer Science. New York, (2010).
3. de Waard, C.; Milliams, D.E. Carbonic Acid Corrosion of Steel. *Corrosion*, **1975** 31 (5), 177–181. <https://doi.org/10.5006/0010-9312-31.5.177>
4. de Waard, C., Milliams, D.E. Prediction of Carbonic Acid Corrosion in Natural Gas Pipelines, *First International Conference on the Internal and External Protection of Pipes*, University of Durham, 1975.
5. Kittel, J.; Remita, E.; Ropital, F.; Sutter, E.; Tribollet, B.; Vivier, V. Hydrogen evolution in aqueous solutions containing dissolved CO<sub>2</sub>: Quantitative contribution of the buffering effect. *Corrosion Science*. **2008**, 50 (5), 1433-1440. <https://doi.org/10.1016/j.corsci.2007.12.007>
6. NACE Impact – Economic Impact <http://impact.nace.org/economic-impact.aspx>
7. Cost of Corrosion Estimate in the United States <https://www.g2mtlabs.com/cost-of-corrosion/>

8. U.S. Department of Transportation Pipeline and Hazardous Materials Safety Administration Office of Pipeline Safety, *Pipeline Corrosion – Final Report*. U.S. Department of Transportation Pipeline and Hazardous Materials Safety Administration, November 2008.  
<https://www.phmsa.dot.gov/sites/phmsa.dot.gov/files/docs/technical-resources/pipeline/gas-transmission-integrity-management/65341/finalreportpipelinecorrosion.pdf>
9. AMPP – *Cost of corrosion study* <https://www.ampp.org/resources/what-is-corrosion/corrosion-reference-library/cost-of-corrosion-study>
10. Silverman, D.C. The Rotating Cylinder Electrode for Examining Velocity-Sensitive Corrosion—A Review. *Corrosion* **2004**, 60 (11), 1003-1023.  
<https://doi.org/10.5006/1.3299215>
11. Revie, R.W., Uhlig's Corrosion Handbook, 3<sup>rd</sup> Ed. John Wiley & Sons, Inc., 2011. DOI:10.1002/9780470872864
12. Ruzic, V., Veidt, M., & Nescic, S. Protective iron carbonate films - Part 1: Mechanical removal in single-phase aqueous flow. *Corrosion* **2006**, 62 (5), 419-432. <https://doi.org/10.5006/1.3278279>
13. Li, W., Potts, B.F.M., Brown, B., Kee, K.E., Nescic, S. A direct measurement of wall shear stress in multiphase flow—Is it an important parameter in CO<sub>2</sub> corrosion of carbon steel pipelines?. *Corrosion Science* **2016**, 110, 35-45.  
<https://doi.org/10.1016/j.corsci.2016.04.008>

14. Akeer, E.; Brown, B.; Nestic, S. The Influence of Mild Steel Metallurgy on the Initiation of Localized CO<sub>2</sub> Corrosion in Flowing Conditions, *NACE International Corrosion Conference & Expo*, Orlando, Florida, March 2013; No. 2383.
15. Ramsey, M. Practical Wellbore Hydraulics and Hole Cleaning, Elsevier Science, 2019. <https://doi.org/10.1016/C2018-0-01191-3>
16. Nestic, S. CHE 7500 Advanced ChE Momentum Transport, Department of Chemical and Biomolecular Engineering, Ohio University, Athens, OH. Personal Communication. January 2022-May 2022.
17. ANSYS FLUENT 12.0 Theory Guide - 7. Species Transport and Finite-Rate Chemistry.  
<https://www.afs.enea.it/project/neptunius/docs/fluent/html/th/node126.htm>
18. ANSYS FLUENT 12.0 Theory Guide - 18. Solver Theory.  
<https://www.afs.enea.it/project/neptunius/docs/fluent/html/th/node359.htm>
19. Eisenberg, M., Tobias, C.W., and Wilke, C.R. Ionic Mass Transfer and Concentration Polarization at Rotating Electrodes, *Electrochemical Society*, **1954**, 101 (6), 306-320. <https://doi.org/10.1149/1.2781252>
20. Standard Practice for Laboratory Immersion Corrosion Testing of Metals, ASTM Standard G 31, 1999. <https://www.astm.org/Standards/G31>
21. FREECORP™ 2.0: Institute for Corrosion and Multiphase Technology, Ohio University: Athens, OH, 2018.  
<https://secure.icmt.ohio.edu/web/software/public/freecorp2/>

22. Ansys Fluent Release 24.1 ANSYS, Inc, 2024.  
<https://www.ansys.com/products/fluids/ansys-fluent>
23. ANSYS FLUENT 12.0 User's Guide - 9.3 Swirling and Rotating Flows.  
<https://www.afs.enea.it/project/neptunius/docs/fluent/html/ug/node349.htm>
24. Liu, G., Tree, D.A., and High, M.S. Relationships Between Rotating Disk Corrosion Measurements and Corrosion in Pipe Flow, *Corrosion*, **1994**, 50 (8), 584-593. <https://doi.org/10.5006/1.3293529>
25. V. Levich, *Physicochemical Hydrodynamics*, Prentice Hall, 1962
26. Bard, Allen J., and Larry R. Faulkner. *Electrochemical Methods: Fundamentals and Applications*, John Wiley & Sons, 2002.
27. *Electrochemical Techniques for Corrosion Measurement*, Gamry Instruments.  
<https://www.gamry.com/assets/Uploads/Echem-Corrosion-Measurement.pdf>
28. Ahmad, Zaki. *Principles of Corrosion Engineering and Corrosion Control*, Elsevier Ltd., 2006.

## **Appendix A: Additional Experimental Methodology**

### **Flowmeter Calibration**

#### ***Equipment***

- PVC flowmeter calibration rig
- Spring scale
- 5-gallon bucket
- Stopwatch

#### ***Experimental Apparatus***

Flowmeter calibration was performed using a PVC pipe connected to a garden hose on one end and to the flowmeter on the other. Water was collected in a bucket and weighed with a spring scale.

#### ***Procedure***

In order to determine the conversion between output voltage from the flowmeter and a flow rate, a calibration had to be performed. To perform this calibration, a PVC rig was created to adapt a garden hose to the flowmeter. Inlet and outlet PVC pipes were attached to the flowmeter using PVC unions tightened by hand. This apparatus was then attached to a garden hose. The flowmeter was attached to its 19 V DC power supply and plugged in. A voltmeter was also attached to the flowmeter. The PVC rig was placed flat on a cart and flow was established by turning on the garden hose. The flow rate was increased until the voltage readout from the flowmeter read a relatively constant value; if the flow rate was below the minimum for the flowmeter, the voltage readout was unstable. After a constant voltage readout was established, a 5-gallon bucket was used to

collect the water coming out of the flowmeter. Prior to water entering the bucket, the bucket was placed on a spring scale and the spring scale was zeroed out so that future uses of the spring scale would only account for the mass of water in the bucket. A stopwatch was used to record the amount of time during which water was being collected in the bucket.

The stopwatch was started as soon as the 5-gallon bucket was placed under the water stream. When the bucket began to get heavy in the hands of the person running the experiment, it was removed from the water stream and the stopwatch was stopped. The bucket of water was then weighed on the spring scale. The mass of water collected, the time under which it was collected, and the voltage output from the flowmeter were all recorded. After each experiment, water from the 5-gallon bucket was discarded and the bucket was weighed on the spring scale again. The zero point of the spring scale was adjusted, if necessary, at this point prior to the next experiment. Once the data was collected, the bucket was emptied, the scale was zeroed with the mass of the bucket, and the stopwatch was reset, the water flow rate could be changed for the next data point. The water flow rate was increased until the voltage output increased by approximately 0.1 V. This procedure was then repeated for each flow rate evaluated. Data was collected for voltage outputs up to approximately 0.4 V since experiments with the flowtube resulted in voltage outputs up to 0.48 V. Four independent sets of data were collected.

Once experimentation was complete, the shutdown procedure was as follows: The water line going into the garden hose was completely turned off. The power cable for the flowmeter was disconnected and the voltmeter was turned off. Any water remaining

in the bucket was discarded. The garden hose was disconnected from the PVC experimental rig. Any water remaining in the garden hose was emptied and discarded. The PVC unions were disconnected from the flowmeter and any water within the flowmeter, or the PVC pipes was emptied out and discarded.

### ***Results***

After data was collected, the mass was converted to volume by assuming a constant water density of  $0.997 \frac{\text{g}}{\text{mL}}$ . This allowed the volume of water to be divided by the time during which it was collected in order to calculate a volumetric flow rate. The volumetric flow rate was plotted against the voltage output from the flowmeter and is shown in Figure 90 below. A trendline was added in order to determine the conversion factor between the voltage output and the volumetric flow rate it represents. The  $R^2$  value of 0.978 indicates a linear relationship between the voltage output from the flowmeter and the volumetric flow rate.

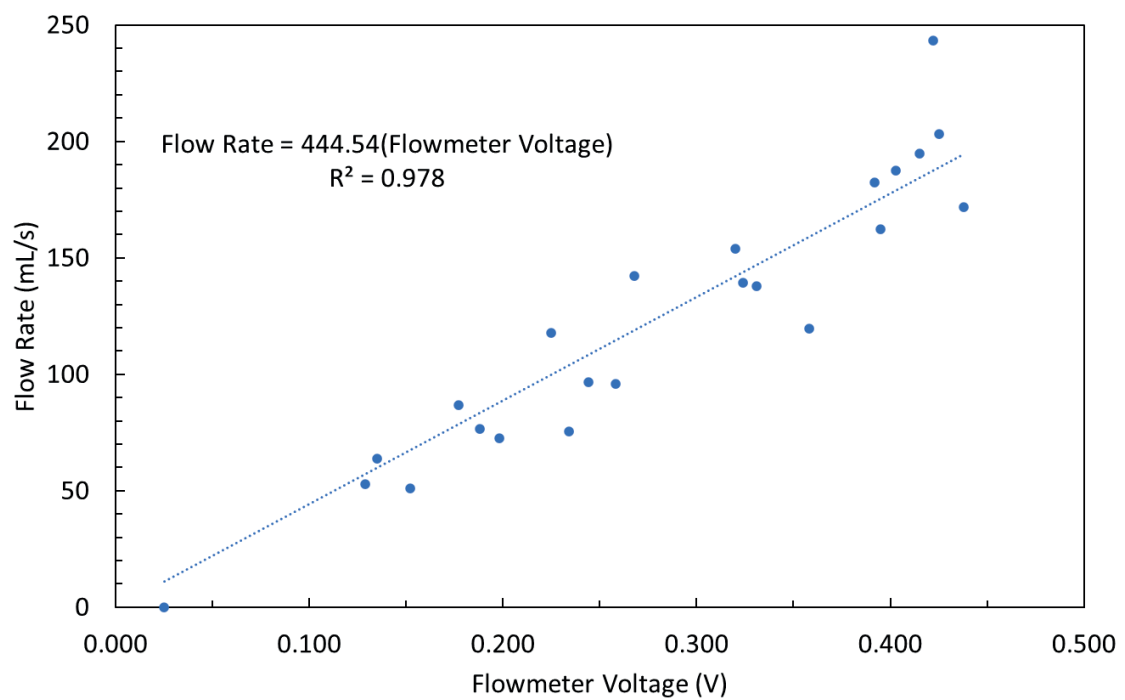


Figure 90. Flowmeter Calibration Curve

## Flowtube Flow Rate Calibration

### *Equipment*

- Flowtube apparatus
- Flowmeter
- Voltmeter
- PVC flowtube flow experimental rig

### *Experimental Apparatus*

Flowtube flow rate calibration experimentation was performed using a flowtube flow experimental rig developed by Albert Schubert. A schematic of this experimental rig is shown in Figure 91 below.

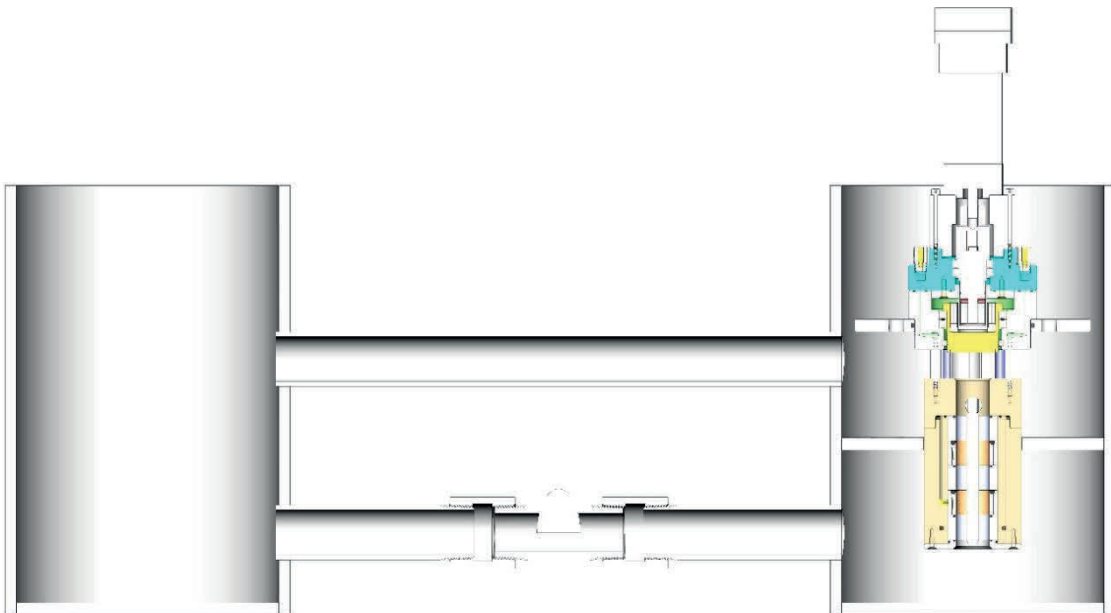


Figure 91. Flowtube calibration rig used in voltage response calibration (Albert Schubert)

### *Procedure*

Before any flow experimentation could take place, the flowtube had to be prepared for experimentation. In order to do so, three specimens (one nickel specimen and two steel specimens) and two reference electrodes were inserted into the flowtube's specimen holder. Prior to being inserted into the flowtube, the specimens were each polished by hand with 600 grit abrasive paper. It should be noted that no electrochemical experimentation was being performed, so old prototypes of reference electrodes were used because they were available. To insert the specimens and reference electrodes into the specimen holder, the bottom plate of the flowtube was removed. The specimens and reference electrodes were inserted in the following order: nickel specimen, reference electrode, steel specimen, reference electrode, steel specimen. Once the specimens and reference electrodes were inserted, the bottom plate was reattached to the flowtube. After this, a counter electrode was inserted in the middle of the specimen holder and secured by tightening a set screw located on the outside of the specimen holder.

A PVC flow experimental rig created by Albert Schubert was used for the flowtube flow rate calibration experiments. In this apparatus, two halves were connected with the included PVC union in the top PVC tube, which was tightened by hand. A flowmeter was installed using two more PVC unions tightened by hand, connecting the bottom PVC tube. Once assembled, the flowtube was installed in the side that contained the separator plate. It should be noted that the side which contained the separator plate and flow tube was determined by observing the orientation of the flowmeter and ensuring that flow was supposed to go along the bottom PVC tube toward the bottom of the

flowtube. The separator plate was maneuvered within the rig to ensure that the flowtube could rest on it while remaining perpendicular to the bottom of the rig and not in contact with the bottom of the rig.

Once the rig was assembled and the flowtube was inserted, the rig was filled with tap water. To do this, a 5-gallon bucket was filled with tap water, which was then dumped into the side of the PVC rig that did not contain the flowtube. Water was added until the water line exceeded the top of the top PVC tube connecting the two halves of the rig.

After water was added to the system, the flowmeter was attached to the 19 V power supply and plugged in. Additionally, the flowtube controller was also plugged in and powered on. Once the equipment was connected to power, a voltmeter was connected to the flowtube controller and the flowmeter (one voltmeter per device).

The dial on the flowtube controller was then turned until the voltmeter attached to the flowtube controller read 1.150 V. It should be noted that the flowtube controller has a fuse that will blow if the voltage going into the flowtube exceeds 1.2 V. After ensuring that the flowtube was generating a flow, there were no visible air bubbles in the system, and the water level did not rise close to the electrical connections on the flowtube, the system was left to run for 1 minute to ensure the flowmeter reached equilibrium. After this point, the voltage on the flowtube controller and the voltage reported by the flowmeter were recorded. Once the data was recorded, the dial on the flowtube controller was adjusted to the next desired voltage and the procedure was followed again. This procedure was performed to record data at a series of controller voltages spanning

between 0.3 V and 1.2 V. Three independent sets of data were collected. Data were also taken when the dial was turned completely to the off position on the flowtube controller and water was not flowing.

Once experimentation was complete, the shutdown procedure was as follows:

The dial on the flowtube controller was turned entirely counterclockwise to turn it to the off position. The power switch for the flowtube controller was then turned to the off position. The power cables for both the flowtube controller and the flowmeter were unplugged from the wall outlets. The flowtube was removed from the PVC experimental rig and placed on paper towels on the test bench. The set screw for the counter electrode on the flowtube apparatus was loosened and the counter electrode was removed from the flowtube. A paper towel was used to dry the counter electrode before setting it aside. A paper towel was inserted into the specimen holder of the flowtube to dry the inner surface of the specimens and reference electrodes within the flowtube. The bottom plate of the flowtube was then removed. The specimens and reference electrodes were removed one by one and examined to determine if moisture had leaked behind any of them. Each specimen and reference electrode were dried with a paper towel prior to being set aside and after each individual one was removed from the flowtube, a paper towel was used to wipe any water that may have fallen into the interior of the flowtube, since failing to do this may give a false indication that water leaked behind a specimen or reference electrode. As each specimen was removed and dried, it was placed in a specimen bag for storage. Once all specimens and reference electrodes were removed, paper towels were used to dry any visible water still on the flowtube. The flowtube was then left laying on

its side on top of dry paper towels to dry completely before the next use. The PVC experimental rig was then taken over to the nearest sink or available drain. The PVC experimental rig was lifted by hand and all water in the system was poured out and discarded down the drain. Once the water was removed from the PVC experimental rig, all PVC unions were disconnected, and the flowmeter was placed on the testing bench to dry completely. The PVC experimental rig was then left to air dry until next use.

### ***Results***

After data was collected for both the voltage going into the flowtube controller and voltage coming out of the flowmeter, it was graphed as shown in Figure 92 below. An  $R^2$  value of 0.999 indicates a very strong linear relationship between the controller voltage and flowmeter voltage, which was expected.

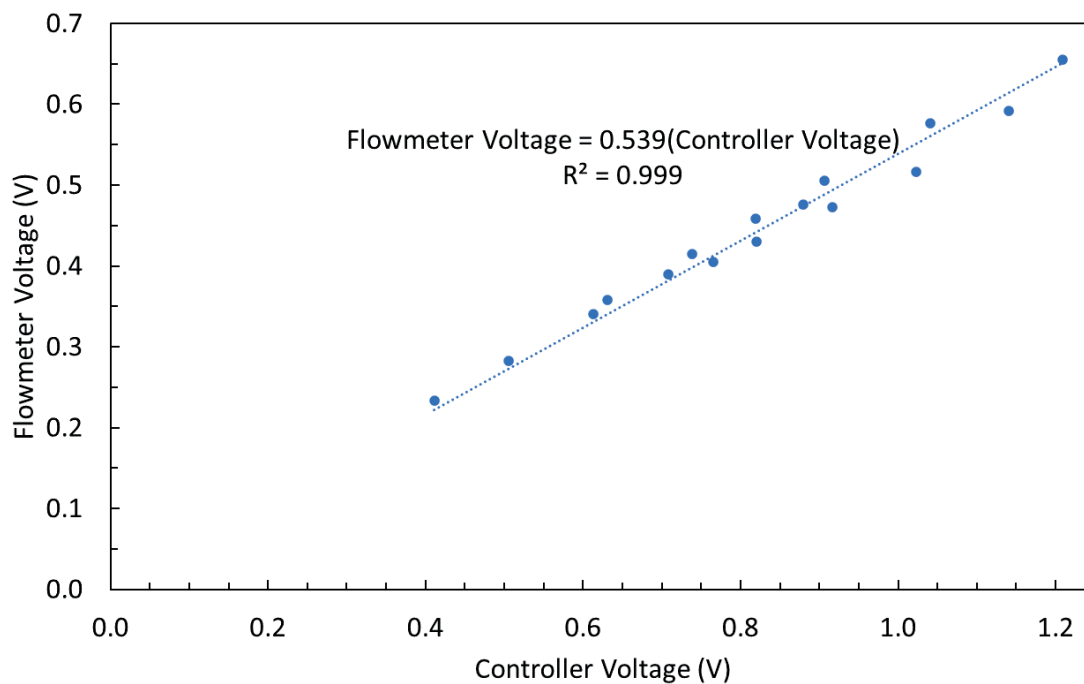


Figure 92. Flowmeter Voltage Output as a Function of Controller Voltage Input

The correlation determined in Figure 90 was used to convert the flowmeter voltage output into a volumetric flow rate. The volumetric flow rate was then divided by the cross-sectional area of the water flowing through the flowtube in order to determine the superficial velocity of the water. This can be used in future calculations for practical application of the flowtube. The calculated superficial velocities were plotted against the voltage input for the controller as shown in Figure 93 below. This allowed a correlation to be created showing superficial velocity as a function of voltage input to the flowtube controller. It should be noted that the maximum superficial velocity capable of being produced by water in the flowtube is approximately 0.6 m/s because of the 1.2 V limit for

voltage input to the flowtube controller discussed in the flowtube calibration Procedure section.

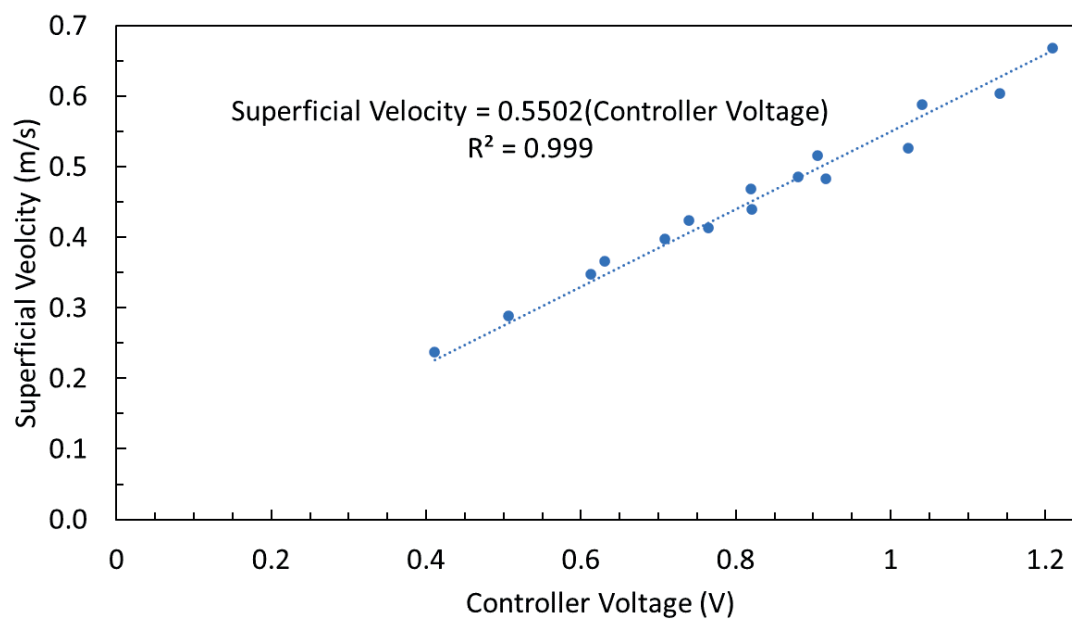


Figure 93. Superficial Velocity as a Function of Voltage Input to Flowtube Controller

## Reference Electrode OCP Calibration

### *Equipment*

- PEEK reference electrode in 3.8 M KCl, AgCl solution
- Brass ring (to be replaced with silver ring)
- PVC experimental rig with rubber stopper
- Ag|AgCl reference electrode
- 1 M KCl solution
- Gamry potentiostat

### *Experimental Apparatus*

Reference Electrode OCP calibration and experimentation was performed using a PVC experimental rig created by Albert Schubert. This experimental rig is then connected to a potentiostat in order to obtain data. This PVC experimental rig is shown in Figure 94 below.



Figure 94. PVC Experimental Apparatus for Use in OCP Calibration

***Procedure***

To begin, the procedure for assembling the reference electrode is as follows: the PEEK portion of the reference electrode is submerged in 3.8 M KCl, AgCl solution so

that the tip does not dry out. The brass ring is placed over top of the PEEK portion in the orientation where the ridge on the brass ring is upwards and the larger end of the PEEK portion is downwards in the solution. The brass ring is pressed into place so the O rings on the PEEK portion seal the 3.8 M KCl, AgCl solution inside the reservoir area of the PEEK portion.

Once the reference electrode is assembled, the exterior is dried off with a paper towel. The reference electrode is then placed inside the PVC experimental rig with the O ring on the outside of the reference electrode facing downwards. This will prevent solution from getting between the brass ring and the walls of the PVC experimental rig. The set screw of the experimental rig is then tightened to make contact with the brass ring.

The Ag|AgCl reference electrode is placed in the middle of the flowtube reference electrode. The cavity is then filled with 1 M KCl solution. Once the solution is in the experimental rig, the electrical connections are made with the Gamry potentiostat. The working and working sense alligator clips are connected to the set screw on the experimental rig. The reference connection is connected to the Ag|AgCl reference electrode.

Using the Gamry Framework software, the open circuit potential is run for 10 minutes. This should be enough time to see if the open circuit potential will remain stable. The experiment can be run for a longer duration of time if desired.

### ***Results***

Data was collected for open circuit potential using the brass ring in four trial runs, as shown in Figure 95 below. As shown in Figure 95, there was no consistency with the OCP. Since the Ag|AgCl reference electrode and the flowtube reference electrode were connected through an electrolyte solution and no other factors were known to be influencing either electrode, it would be expected that the OCP would be a constant value with very little change over time. However, this was not the case; for the first three runs, it appeared almost as if each consecutive experiment run started where the previous one left off. There was no apparent pattern or trend for stability. The fourth run was allowed to proceed for 2 hours; after approximately an hour and a half, the OCP appeared to stabilize around -285 mV. It is unclear if this result is reproducible, however it would still indicate that a brass ring is incompatible with the flowtube reference electrode even if that result were reproducible; it is impractical to have to wait for an hour and a half for a stable OCP while using the flowtube apparatus in corrosion experimentation. Due to these results and previous failed attempts to create a reproducible procedure to create the flowtube reference electrode using a brass ring, a new ring will be manufactured out of silver. This silver ring will replace the brass ring once it has been created. Once the silver ring is inserted, the OCP will be expected to be stable at 0 mV vs the Ag|AgCl reference electrode. In the future, the flowtube reference electrode can be tested against the saturated calomel electrode to convert any potential readings to potential vs standard hydrogen electrode.

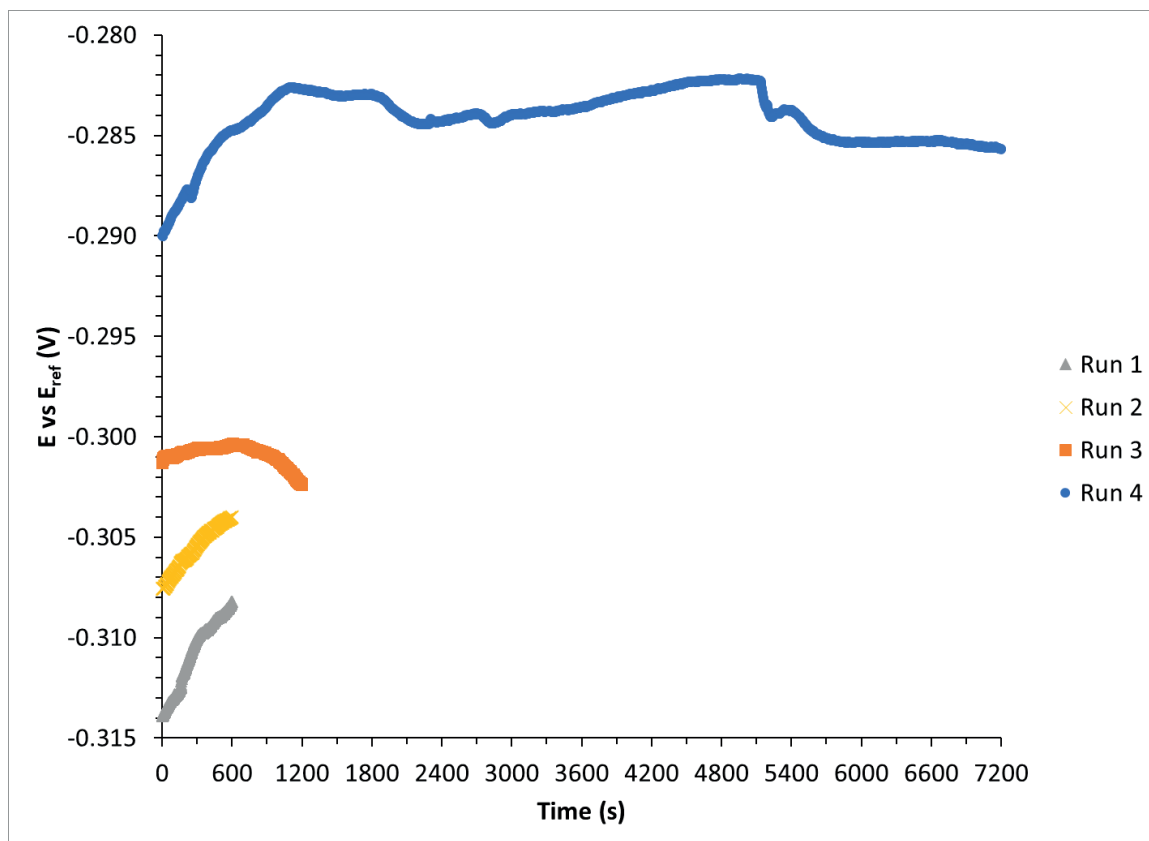


Figure 95. Open Circuit Potential Using Brass Ring on Flowtube Reference Electrode

## **Proposed Flowtube Baseline Corrosion experimentation**

### ***Equipment***

- Flowtube apparatus
- Two assembled reference electrodes
- Three electrochemical specimens (nickel or 1018 mild steel depending on the experiment)
- Central counter electrode
- 4 L glass cell

### ***Experimental Apparatus***

Mass transfer and corrosion experimentation will be performed in a 4 L glass cell on a hot plate/stirrer. 3.6 liters of experimental solution will be present in the 4 L glass cell; this volume accounts for displacement due to the size of the flowtube. The glass cell will be sparged with nitrogen gas before experimentation is performed for mass transfer experiments. For corrosion experimentation, the cell will be sparged with nitrogen gas for one set of experiments and carbon dioxide gas for the second set of experiments. All experiments will be performed with the flowtube apparatus submerged in solution within the glass cell. A sample drawing of the flowtube in a 2 L glass cell was shown above in Figure 2.

### ***Materials Tested***

Mass transfer experiments will be performed using a ferricyanide/ferrocyanide solution. Corrosion experiments will be performed using a 1018 mild steel flowtube specimen.

*Test Matrix*

Table 18. Test Matrix for Flowtube Mass Transfer Experimentation

<b>Parameter</b>	<b>Conditions</b>
Material	Ni  Surface Area: 15.2 cm <sup>2</sup>
Temperature	30°C
Total Pressure (N <sub>2</sub> )	0.97 bar
Electrolyte	0.5 M of NaOH  M of K <sub>3</sub> Fe(CN) <sub>6</sub>  0.01 M of K <sub>4</sub> Fe(CN) <sub>6</sub> ·3H <sub>2</sub> O
Flowtube Controller Voltage	0.545, 0.727, 0.909, 1.091 V
Electrochemical Techniques	Potentiodynamic Sweep <ul style="list-style-type: none"> <li>• 0.4 V above E<sub>oc</sub> (Anodic)</li> <li>• 1.7 V below E<sub>oc</sub> (Cathodic)</li> <li>• Scan Speed: 5 mV/s</li> </ul>

Table 19. Test Matrix for Flowtube Corrosion Experimentation

Parameter	Conditions
Material	1018 Mild Steel Surface Area: 15.2 cm <sup>2</sup>
Temperature	35°C
Total Pressure (N <sub>2</sub> or CO <sub>2</sub> )	0.96 bar
Electrolyte	1 wt% NaCl pH adjusted with HCl or Na <sub>2</sub> CO <sub>3</sub>
pH	4.0±0.1, 5.0±0.1, 6.0±0.1
Flowtube Controller Voltage	0.545, 0.727, 0.909, 1.091 V
Electrochemical Techniques	<p>LPR</p> <ul style="list-style-type: none"> <li>• 5 mV above E<sub>oc</sub> (Anodic)</li> <li>• 5 mV below E<sub>oc</sub> (Cathodic)</li> <li>• Scan Speed of 0.125 mV/s</li> </ul> <p>Potentiodynamic Sweep</p> <ul style="list-style-type: none"> <li>• V above E<sub>oc</sub> (Anodic)</li> <li>• 0.5 V below E<sub>oc</sub> (Cathodic)</li> <li>• Scan Speed of 0.125 mV/s</li> </ul> <p>EIS</p> <ul style="list-style-type: none"> <li>• 5000 Hz to 0.1 Hz</li> </ul>

## **Polishing RDE Specimen**

### ***Equipment***

- RDE Specimen
- 1000 grit and 1200 grit abrasive paper
- Buehler EcoMet 3000 Variable Speed Grinder-Polisher
- Isopropyl alcohol
- Ultrasonic cleaner

### ***Experimental Apparatus***

Specimen polishing was performed using the Buehler EcoMet 3000 Variable Speed Grinder-Polisher located in the polishing room. The desired abrasive paper was affixed to the rotating surface of the grinder-polisher using the included mounting ring. The RDE specimen was pressed onto the abrasive surface and held in place by hand.

### ***Procedure***

The X65 mild steel RDE specimen was sequentially polished using 1000 grit and 1200 grit abrasive paper on the Buehler EcoMet 3000 Variable Speed Grinder-Polisher. Tap water is connected to the Buehler polisher, which was consistently being sprayed onto the surface of the abrasive paper. The Buehler polisher was set to a rotational speed of 250 RPM to ensure even polishing. First the 1000 grit abrasive paper was secured onto the Buehler polisher, and the RDE specimen, which was previously inserted into the PTFE RDE tip, was held on the abrasive paper surface. After clear lines were visible on the RDE specimen surface, it was rotated 90° and the RDE specimen was again held on the abrasive paper surface. If clear lines were visible in only one direction on the RDE

specimen surface after this second round of polishing, then the specimen was considered to be polished to 1000 grit. If lines were visible going in multiple directions on the RDE surface, the specimen was rotated 90° again and held to the abrasive paper surface. This process was repeated until the specimen was polished to 1000 grit. The 1000 grit abrasive paper was then removed from the Buehler polisher, and the 1200 grit abrasive paper was secured onto the Buehler polisher. The polishing procedure was repeated to polish the specimen to 1200 grit.

After polishing the specimen, it was sprayed with isopropyl alcohol. It was then cleaned with the ultrasonic cleaner; the specimen was placed in a beaker or small bottle, which was filled to just above the height of the RDE tip with isopropyl alcohol. The beaker/bottle was placed in the center of the ultrasonic cleaner. The ultrasonic cleaner was set to the 30W setting and set for 5 minutes. Once the cleaning was complete, the specimen was removed from the isopropyl alcohol by pouring the contents of the beaker/bottle onto a gloved hand. The specimen was dried using the heat gun located in the polishing room.

## Appendix B: Equations

### Mass Transfer Experimentation and RCE Equations

Mass transfer experiments were performed in a 0.01 M potassium ferricyanide and 0.01 M potassium ferrocyanide solution. As potentiodynamic sweeps were performed, ferricyanide was reduced to ferrocyanide by the reaction below:

Reduction of ferricyanide:



In order to calculate the mass transfer coefficient, the following equation was used:

$$k_m = \frac{i_{lim}}{nFC_b} \quad (1)$$

Where:  $k_m$  = mass transfer coefficient  $\left(\frac{m}{s}\right)$ ,  $i_{lim}$  = limiting current density  $\left(\frac{A}{m^2}\right)$ ,  $n$  = number of electrons transferred  $\left(\frac{mol\ e^-}{mol}\right)$ ,  $F$  = Faraday's constant  $\left(\frac{A \cdot s}{mol\ e^-}\right)$ , and  $C_b$  = concentration of active species  $\left(\frac{mol}{m^3}\right)$

Also, the rotational speed of the RCE was converted to pipe flow velocity using the following equation below developed by Silverman.<sup>10</sup>

$$u_{cyl} = 0.1185 \left( \left( \frac{\mu}{\rho} \right)^{-0.25} \left( \frac{d_{cyl}^{\frac{3}{7}}}{d_{pipe}^{\frac{28}{5}}} \right) Sc^{-0.0857} \right) u_{pipe}^{\frac{5}{4}} \quad (2)$$

Where:  $u_{cyl}$  = velocity of rotating cylinder  $\left(\frac{cm}{s}\right)$ ,  $\mu$  = dynamic viscosity of fluid  $\left(\frac{g}{cm \cdot s}\right)$ ,  $\rho$  = density of fluid  $\left(\frac{g}{cm^3}\right)$ ,  $d_{cyl}$  = diameter of rotating cylinder (cm),  $d_{pipe}$  = diameter of pipe (cm),  $Sc$  = Schmidt Number (*dimensionless*), and  $u_{pipe}$  = velocity of pipe flow  $\left(\frac{cm}{s}\right)$

The Sherwood correlation used to fit the curves shown in Figure 8 above was:

$$Sh = aRe^bSc^c \quad (3)$$

Where:  $Sh$  = Sherwood Number (*dimensionless*),  $Re$  = Reynolds Number (*dimensionless*),  $Sc$  = Schmidt Number (*dimensionless*), and  $a$ ,  $b$ , and  $c$  are all empirical constants which are specific for a given flow geometry and the flow regime.

To determine the appropriate values for  $a$ ,  $b$ , and  $c$ , the Sherwood Number was calculated by:

$$Sh = \frac{k_m d}{D} \quad (4)$$

Where:  $Sh$  = Sherwood Number (*dimensionless*),  $k_m$  = mass transfer coefficient  $\left(\frac{m}{s}\right)$ ,

$d$  = diameter of rotator ( $m$ ), and  $D$  = diffusivity of active species  $\left(\frac{m^2}{s}\right)$

The Reynolds Number for a cylinder was calculated by:

$$Re = \frac{\rho v d}{\mu} \quad (5)$$

Where:  $Re$  = Reynolds Number (*dimensionless*),  $\rho$  = density of fluid  $\left(\frac{kg}{m^3}\right)$ ,  $v$  = rotator

speed  $\left(\frac{m}{s}\right)$ ,  $d$  = diameter of rotator ( $m$ ), and  $\mu$  = dynamic viscosity of fluid  $\left(\frac{kg}{m \cdot s}\right)$

The Schmidt Number was calculated by:

$$Sc = \frac{\mu}{\rho D} \quad (6)$$

Where:  $Sc$  = Schmidt Number (*dimensionless*),  $\mu$  = dynamic viscosity of fluid  $\left(\frac{kg}{m \cdot s}\right)$ ,  $\rho$

= density of fluid  $\left(\frac{kg}{m^3}\right)$ , and  $D$  = diffusivity of active species  $\left(\frac{m^2}{s}\right)$ .

### **RDE Equations**

For RDE experiments, the rotational speed must be converted to effective pipe flow velocity in order to compare the results to other systems. In order to convert the rotational speed into effective pipe flow velocity, the Reynolds number, Schmidt number, and

Sherwood number for both RDE rotation and pipe flow can be utilized. The Reynolds number is also utilized to verify the desired RDE rotational speed yields a laminar flow.

The dimensionless numbers for an RDE can be calculated using the following equations.

$$Re_{RDE} = \frac{\omega r_{RDE}^2}{\nu} \quad (7)$$

$$Sc_{RDE} = \frac{\nu}{D} \quad (8)$$

$$Sh_{RDE} = \frac{k_{RDE} d_{RDE}}{D} \quad (9)$$

$$Sh_{RDE} = 0.62 Re_{RDE}^{0.5} Sc_{RDE}^{0.33} \quad (10)$$

Where:  $Re_{RDE}$  = Reynolds number for a rotating disk electrode (*dimensionless*),

$Sc_{RDE}$  = Schmidt number for a rotating disk electrode (*dimensionless*),

$Sh_{RDE}$  = Sherwood number for a rotating disk electrode (*dimensionless*),

$\omega$  = rotational speed of the rotating disk ( $\frac{rad}{s}$ ),  $r_{RDE}$  = radius of rotating disk (*cm*),

$\nu$  = kinematic viscosity ( $\frac{cm^2}{s}$ ),  $D$  = mass diffusivity ( $\frac{cm^2}{s}$ ),

$k_{RDE}$  = mass transfer coefficient ( $\frac{cm}{s}$ )

These equations can be solved for the mass transfer coefficient for the RDE to achieve the following equation.

$$k_{RDE} = 0.62D^{0.33}\nu^{-\frac{1}{6}}\omega^{0.5} \quad (11)$$

The dimensionless numbers for a pipe can be calculated using the following equations.

$$Re_{pipe} = \frac{V_{pipe}d_{pipe}}{\nu} \quad (12)$$

$$Sc_{pipe} = \frac{\nu}{D} \quad (13)$$

$$Sh_{pipe} = \frac{k_{pipe}d_{pipe}}{D} \quad (14)$$

$$Sh_{pipe} = 0.0165Re_{pipe}^{0.86}Sc_{pipe}^{0.33} \quad (15)$$

Where:  $Re_{pipe}$  = Reynolds number for a pipe (*dimensionless*),

$Sc_{pipe}$  = Schmidt number for a pipe (*dimensionless*),

$Sh_{pipe}$  = Sherwood number for a pipe (*dimensionless*),  $V_{pipe}$  = pipe flow velocity

$\left(\frac{cm}{s}\right)$ ,  $d_{pipe}$  = diameter of the pipe (*cm*),  $\nu$  = kinematic viscosity  $\left(\frac{cm^2}{s}\right)$ ,  $D$  = mass

diffusivity  $\left(\frac{cm^2}{s}\right)$ ,  $k_{RDE}$  = mass transfer coefficient  $\left(\frac{cm}{s}\right)$

These equations can be solved for the mass transfer coefficient for the pipe to achieve the following equation.

$$k_{pipe} = 0.0165V_{pipe}^{0.86}d_{pipe}^{-0.14}\nu^{-0.53}D^{\frac{2}{3}} \quad (16)$$

By equating the mass transfer coefficients, the following equation can be derived to illustrate the relationship between the RDE rotational speed and the effective pipe flow velocity.

$$rpm_{RDE} = \omega \frac{60}{2\pi} = 6.67 \times 10^{-3}V_{pipe}^{1.72} \quad (17)$$

In order to determine the theoretical mass transfer boundary thickness at a given rotational speed, the following equation was utilized.<sup>26</sup>

$$\delta_m = 1.61D^{1/3}\nu^{1/6}\omega^{-1/2} \quad (18)$$

When the diffusivity (D) is set to  $1.06 \times 10^{-8} \frac{m^2}{s}$ , the kinematic viscosity ( $\nu$ ) is set to  $7.99 \times 10^{-7} \frac{m^2}{s}$ , and the rotational speed ( $\omega$ ) is converted to RPM in order to replicate the experimental conditions, then Equation (18) can be simplified to the following equation as shown in Figure 89.

$$\delta_m = 1.0519(RPM)^{-1/2} \quad (19)$$

### Corrosion Rate Calculations

After the cathodic and anodic Tafel Slopes are experimentally determined, the following equations can be used to calculate the corrosion rate.<sup>27, 28</sup>

$$B = \frac{\beta_a \beta_c}{2.303(\beta_a + \beta_c)} \quad (20)$$

$$i_{corr} = 10^3 \frac{B}{R_p} \quad (21)$$

$$CR = (\text{constant}) \frac{i_{corr} E_w}{\rho} \quad (22)$$

Where:  $B$  = slope of the Tafel plot  $\left(\frac{mV}{decade}\right)$ ,  $\beta_a$  = anodic Tafel Slope  $\left(\frac{mV}{decade}\right)$ ,

$\beta_c$  = cathodic Tafel Slope  $\left(\frac{mV}{decade}\right)$ ,  $i_{corr}$  = corrosion current density  $\left(\frac{A}{m^2}\right)$ ,

$R_p$  = polarization resistance ( $\Omega$ ),  $CR$  = corrosion rate  $\left(\frac{mm}{year}\right)$ ,

$E_w$  = equivalent weight  $\left(\frac{g}{equiv}\right)$ , and  $\rho$  = density  $\left(\frac{kg}{m^3}\right)$ . Note that constant is based on the

testing environment and desired corrosion rate units will need to be utilized in the

corrosion rate equation in order to output the desired units for the corrosion rate.

### **Ansys Fluent Background**

Ansys Fluent is able to generate CFD simulations by solving the following series of equations:

Continuity equation:

$$\frac{\partial \rho}{\partial t} + \frac{\partial(\rho u_i)}{\partial x_i} = 0 \quad (23)$$

Where:  $\rho$  = density of fluid  $\left(\frac{kg}{m^3}\right)$ ,  $t$  = time ( $s$ ),  $u_i$  = velocity in direction  $i$   $\left(\frac{m}{s}\right)$ , and  $x_i$  =

distance in direction  $i$  ( $m$ )

3-dimensional Navier-Stokes equation:

$$\frac{\partial \rho u_j}{\partial t} + \frac{\partial}{\partial x_i} (\rho u_j u_i) = \rho f_j - \frac{\partial P}{\partial x_j} + \frac{\partial}{\partial x_i} \left( \mu \frac{\partial u_j}{\partial x_i} \right) + \frac{1}{3} \frac{\partial}{\partial x_j} \left( \mu \frac{\partial u_i}{\partial x_i} \right) \quad (24)$$

Where:  $\rho$  = density of fluid  $\left(\frac{kg}{m^3}\right)$ ,  $u_j$  = velocity in direction j  $\left(\frac{m}{s}\right)$ ,  $t$  = time (s),  $u_i$  = velocity in direction i  $\left(\frac{m}{s}\right)$ ,  $x_i$  = distance in direction i (m),  $f_i$  = source term in direction i  $\left(\frac{m}{s^2}\right)$ ,  $P$  = pressure  $\left(\frac{kg}{m \cdot s^2}\right)$ ,  $x_i$  = distance in direction j (m), and  $\mu$  = dynamic viscosity of fluid  $\left(\frac{kg}{m \cdot s}\right)$

Mass transfer equation:

$$\frac{\partial}{\partial t} (m^s) + \frac{\partial}{\partial x_i} (m^s u_i) = \frac{\partial}{\partial x_i} \left( D^s \frac{\partial m^s}{\partial x_i} \right) + R^s \quad (25)$$

Where:  $m^s$  = mass (kg),  $t$  = time (s),  $u_i$  = velocity in direction i  $\left(\frac{m}{s}\right)$ ,  $x_i$  = distance in direction i (m),  $D^s$  = diffusivity of active species  $\left(\frac{m^2}{s}\right)$ , and  $R^s$  = source term  $\left(\frac{kg}{s}\right)$

Butler-Volmer equation:

$$i_F = i_0 \left( \frac{c}{c^{ref}} \right)^n \left[ \exp \left( \frac{2.303 \eta}{\beta_a} \right) - \exp \left( \frac{2.303 \eta}{\beta_c} \right) \right] \quad (26)$$

Where:  $i_F$  = electrode current density  $\left(\frac{A}{m^2}\right)$ ,  $i_0$  = exchange current density  $\left(\frac{A}{m^2}\right)$ ,  $c$  = concentration  $\left(\frac{kg}{m^3}\right)$ ,  $c$  = reference concentration  $\left(\frac{kg}{m^3}\right)$ ,  $n$  = number of electrons

transferred  $\left(\frac{\text{mol } e^-}{\text{mol}}\right)$ ,  $\eta = E - E_{eq}$  = overpotential (*V vs SHE*),  $\beta_a$  = anodic Tafel slope  $\left(\frac{\text{mV}}{\text{decade}}\right)$ , and  $\beta_c$  = cathodic Tafel slope  $\left(\frac{\text{mV}}{\text{decade}}\right)$ .

#### k-ε Model of Turbulence

$$\mu_t = \rho C_\mu \frac{k^2}{\varepsilon} \quad (27)$$

Where:  $\mu_t$  = turbulent viscosity  $\left(\frac{\text{kg}}{\text{m}\cdot\text{s}}\right)$ ,  $\rho$  = density of fluid  $\left(\frac{\text{kg}}{\text{m}^3}\right)$ ,  $C_\mu$  = turbulence model constant (*dimensionless*),  $k$  = kinetic energy of turbulence  $\left(\frac{\text{kg}\cdot\text{m}^2}{\text{s}^2}\right)$ , and  $\varepsilon$  = rate of viscous dissipation  $\left(\frac{\text{kg}^2\cdot\text{m}^2}{\text{s}^3}\right)$ .

The Reynolds number is a nondimensional number used to classify the flow as laminar or turbulent. It is also used to compare different systems, such as comparing this small scale flowtube to a large-scale pipeline. For an annulus, such as the flowtube, the Reynolds number is calculated by the following equation.

$$Re = \frac{\rho u (D_{outer} - D_{inner})}{\mu} \quad (28)$$

Where:  $Re$  = Reynolds Number (*dimensionless*),  $\rho$  = density of fluid  $\left(\frac{\text{kg}}{\text{m}^3}\right)$ ,  $u$  = average superficial fluid velocity  $\left(\frac{\text{m}}{\text{s}}\right)$ ,  $D_{inner}$  = diameter of inner cylinder (*m*),  $D_{outer}$  = diameter of outer cylinder (*m*), and  $\mu$  = dynamic viscosity of fluid  $\left(\frac{\text{kg}}{\text{m}\cdot\text{s}}\right)$

In order to be classified as laminar flow, the Reynolds number must be below 2100. In order to be considered fully turbulent, the Reynolds number must be above 4000. Any Reynolds number value between 2100 and 4000 is considered to be transitioning from laminar to turbulent flow. <sup>15</sup>

## **Appendix C: Material Composition Data**

### **1018 Mild Steel #5**

The 1018 mild steel used in RCE experimentation was analyzed using direct reading atom emissions spectroscopy by Laboratory Testing Inc. The analysis concluded that the specimen was found to be in conformance to the specification UNS G10180. The results are shown below in Table 20.

Table 20. Material Analysis for 1018 Mild Steel #5

<b>Element</b>	<b>Measurement</b>
Al	0.008%
As	0.006%
C	0.18%
Co	0.003%
Cr	0.12%
Cu	0.18%
Fe	balance
Mn	0.75%
Mo	0.020%
Nb	0.002%
Ni	0.065%
P	0.011%
S	0.021%
Sb	0.009%
Si	0.16%
Sn	0.009%
Ta	0.028%
Ti	0.002%
V	0.003%
W	0.014%
Zn	0.004%
Zr	0.003%

**X65 Mild Steel #49**

The X65 mild steel used in RDE experimentation was analyzed using Direct Reading Atom Emissions Spectroscopy by Laboratory Testing Inc. The analysis concluded that the specimen was found to be in conformance to the specification API 5L, 45<sup>th</sup> Edition, PSL 1, Grade X65, Seamless Pipe; Welded Pipe. The results are shown below in Table 21.

Table 21. Material Analysis for X65 Mild Steel #49

<b>Element</b>	<b>Measurement</b>
Al	0.0234%
As	0.0076%
B	0.0000%
Bi	<0.0010%
C	0.0538%
Ca	0.0020%
Ce	<0.0010%
Co	<0.0010%
Cr	0.2347%
Cu	0.1108%
Fe	97.5173%
La	<0.0003%
Mn	1.3978%
Mo	0.0718%
N	0.0057%
Nb	0.0358%
Ni	0.2448%
P	0.0033%
Pb	0.0033%
S	0.0000%
Sb	<0.0010%
Se	0.0166%
Si	0.2169%
Sn	0.0018%
Ta	<0.0010%
Te	0.0111%
Ti	0.0111%
V	0.0348%
W	<0.0001%
Zn	<0.0010%
Zr	<0.0010%

Hardness analysis was also performed by Laboratory Testing Inc. on the X65 mild steel specimen using Rockwell Hardness & Rockwell Superficial Hardness testing procedure. This experiment determined that the hardness of the X65 mild steel specimen was  $86.5 \pm 0.5$  using the HRBW scale.

The microstructure of the X65 mild steel was determined by Laboratory Testing Inc. using Microexamination of Metals. The specimen was etched using 2% Nital (ethanolic nitric acid), and 100X – 500X magnification was used. It was determined that the microstructure of the X65 mild steel was uniform with fine structure of pearlite in a ferrite matrix.



**OHIO**  
UNIVERSITY

Thesis and Dissertation Services